QUANTITATIVE OBSERVATIONS OF A DEEP-SEA HYDROTHERMAL PLUME USING AN ACOUSTIC IMAGING SONAR

By

GUANGYU XU

A dissertation submitted to the

Graduate School—New Brunswick

Rutgers, The State University of New Jersey

in partial fulfillment of the requirements

for the degree of

Doctor of Philosophy

Graduate Program in Oceanography

written under the direction of

Karen G. Bemis

and approved by

_____

_____

_____

_____

_____

New Brunswick, New Jersey

October, 2015

ABSTRACT OF THE DISSERTATION

Quantitative Observations of a deep-sea hydrothermal plume using an acoustic imaging sonar

By GUANGYU XU

Dissertation Director:

Karen G. Bemis

The Cabled Observatory Vent Imaging Sonar (COVIS) is used to quantitatively monitor the hydrothermal discharge from the Grotto mound, a venting sulfide structure on the Endeavour Segment of the Juan de Fuca Ridge. Since its deployment in September 2010, COVIS has recorded a multi-year long, near-continuous acoustic backscatter dataset. Further analysis of this dataset sheds light on the backscattering mechanisms within the buoyant plumes above Grotto and yields quantitative information on the influences of oceanic, atmospheric, and geological processes on the dynamics and heat source of the plumes.

An investigation of the acoustic scattering mechanisms within the buoyant plumes issuing from Grotto suggests the dominant scattering mechanism within the plumes is the temperature fluctuations caused by the turbulent mixing of the buoyant plumes with the ambient seawater. In comparison, the backscatter from plume particles is negligible at lower levels of the plume but can potentially be significant at higher levels. Furthermore, this finding demonstrates the potential of inverting the acoustic backsatter to estimate the temperature fluctuations within the plumes.

Processing the backscatter dataset recorded by COVIS yields time-series measurements of the vertical flow rate, volume transport, expansion rate of the largest buoyant plume

above Grotto. Further analysis of those time-series measurements suggests the rate at which the ambient seawater is entrained into the plume increases with the magnitude of the ambient ocean currents—the current-driven entrainment. Furthermore, the oscillations in the ambient ocean currents that are driven by tidal and atmospheric forcing are introduced into the flow field within the plume through the current-driven entrainment.

An inverse method has been developed to estimate the source heat transport driving the largest plume above Grotto from its volume transport estimates. The result suggests the heat transport driving the plume was steady over the 41-month period between October 2011 and February 2015. Comparing the current and historical heat transport measurements with contemporaneous seismic data suggests the evolution of the heat transport since 1988 correlates with the rate of local seismicity with a short episode of increased heat transport following pronounced seismic events and reduced steady heat transport during time periods of quiescent seismicity.

Acknowledgments

First of all, I want to express my deepest gratitude to my advisors Peter Rona, Karen Bemis, and Daniela Di Iorio. I have learned a lot from each one of them and am deeply impressed by their methodical attitudes towards scientific research and mentorship. I want to say I am extremely lucky to have the opportunity of knowing and working with each one of them. It has always been their unreserved support and encouragement that motivated me to carry on and reach this far. I am sincerely hoping one day I can reach their high standards for being a scientist and mentor.

I would also like to extend my sincere gratitude to my committee member Darrell Jackson for being a great mentor in underwater acoustics. I am also very grateful to my other committee members Robert Chant and Diane Adams for their tremendous help in revising this dissertation.

I am very grateful to our colleagues at the Applied physics Laboratory of University of Washington and in particular Russ Light, Mike Kenny, and Vern Miller for their monumental contributions to the engineering aspect of this research. In particular, I want to thank them for designing the Cabled Observatory Vent Imaging Sonar (COVIS)—the primary source of the data used in this dissertation. The marvelous fact that COVIS managed to record data in the harsh environment of a hydrothermal vent site more than a mile below the sea surface for 4 plus years is a true testament to their superb engineering skills.

I remain indebted to the many people at Ocean Networks Canada and in particular Maia Hoeberechts, Reyna Jenkyns, Steve Mihaly, Ian Kulin, Martin Heesemann and Martin Scherwath for their tremendous help and company on the research cruises and during my stay in Victoria, Canada.

I need to thank the entire ROPOS team and in particular Ian Murdock, Keith Shepherd, and Keith Tamburri for the successful deployment of COVIS and the subsequent in-situ

data and sample collection. It has always been a rare treat to me watching them gracefully navigate the ROV through the abyssal valley and magically control the robotic arms with enough dexterity for needlework.

I am very grateful to Armaghan Attar for filtering the particle samples on board for me. I need to thank Kim Juniper and his lab for their help with the post-cruise sample processing. I also need to thank Chip Breier at Woods Hole Oceanographic Institution for instructions on preserving plume particle samples.

I need to thank William Wilcock of University of Washington and his former graduate student Robert Weekly for providing the code for processing the seismometer data and the instrumental instructions.

I want to say a hearty thank you to all the professors and fellow graduate students at the Department of Marine and Coastal Sciences at Rutgers University. I thank them for making the past four plus years a memorable experience to me. In particular, I want to thank Filipa Carvalho for being a tremendous dive buddy and dear friend. Also, a big thanks to Chris Free for helping me brew my first batch of beer.

A huge thank you to my therapist Christina Ortiz for working very hard over the past two years to keep my sanity in check and help me find my own courage.

A sincere thanks to my personal trainer Nipa Patel and the US masters swimming at Rutgers for making me stronger and faster.

Last and most important, I need to thank my mother, father, grandparents and whole family for being my faithful supporters and loyal cheerleaders. I want to say it is your love and care that I cherish the most, and I would be nothing without them.

Dedication

To Peter A. Rona—a great explorer, scientist, and mentor, in memoriam.

Table of Contents

List of Tables

List of Figures

Chapter 1

Introduction

1.1 Hydrothermal Circulation

Seafloor hydrothermal circulation forms a conduit connecting the Earth's interior with the overlying ocean. This circulation begins with seawater percolating downward through the cracked oceanic crust. During its descent, the seawater gradually gets heated and reacts with the bounding rock. Through this water-rock reaction, the seawater gains chemicals such as Fe and Mn and loses chemicals such as Mg and SO_4. In the meantime, the temperature of the seawater continues to increase, and can reach a maximum exceeding 400 °C. Driven by their buoyancy, these ultra-heated fluids start ascending and ultimately exit the seafloor from hydrothermal vents. Since being discovered in the late 1970s on the Galapagos Rift (Corliss et al., 1979; Edmond et al., 1979), seafloor hydrothermal circulation has been a frontier of oceanographic studies attracting researchers from a broad range of disciplines. Over the past several decades, extensive multidisciplinary studies have greatly expanded our knowledge of the role of hydrothermal circulation in connecting Earth's geosphere, biosphere, and hydrosphere (Fornari et al., 2012; Kelley et al., 2012; German and Seyfried, 2014).

Seafloor hydrothermal circulation plays a key role in the energy and chemical budgets of the global ocean. It is estimated that the total fluid transport of hydrothermal circulation is on the order of 10^{19} to 10^{20} g/year, which is comparable to or even greater than the global riverine water transport (Nielsen et al., 2006). At this rate, seawater in the global ocean, which amounts to $\sim 10^{24}$ g, can cycle through hydrothermal circulation in 10^4 to 10^5 years. The total hydrothermal heat output (~ 9 TW), estimated as the differential between conductive heat-flow measured at mid-ocean ridges and that predicted by conductive cooling models, accounts for approximately a quarter of the heat lost from the Earth's

surface and a third of the heat lost from the seafloor (Stein and Stein, 1992, 1994). In addition, the geochemically altered fluids issuing from hydrothermal vents have profound influences on the geochemistry of the global ocean. It is estimated that the transports of chemicals such as Fe and Mn released from hydrothermal discharge can rival the riverine transports of those species (Bickle and Elderfield, 2004). Furthermore, the reduced gases (e.g., H_2S) released from hydrothermal discharge support chemosynthetic microbes that form the base of the food web of lush benthic ecosystems around vent fields, whose abundance can sometimes match that of a tropical rain forest (Govenar, 2012; Luther et al., 2012). This transfer of chemicals from mantle to microbes intrigues the imagination with its intimate interconnections amongst geological, oceanic, and biological processes.

Seafloor hydrothermal discharge loosely falls into two categories: 1) discrete high-temperature venting typically in the form of vigorous hot fluids (up to 400 °C) issuing from chimney-like structures (i.e. hydrothermal vents), and 2) diffuse low-temperature venting typically in the form of warm fluids ($< 100\,^{\circ}C$) percolating through fractured permeable seafloor, which is commonly referred to as diffuse flow. Discrete high-temperature venting, mostly occurring on active plate boundaries (e.g., mid-ocean ridges), is the most spectacular seafloor expression of hydrothermal circulation. Many of the dissolved chemicals in high-temperature hydrothermal fluids precipitate upon mixing with cold ambient seawater, forming large quantities of dark-hued particles (e.g., Fe sulfide and oxide) that make the discharge resemble the black smoke wafting out of a chimney. For this reason, a high-temperature hydrothermal vent is often called a 'black smoker'. The discharge from a 'black smoker', or a hydrothermal plume, cools down and gets diluted rapidly through its mixing with the ambient seawater. Driven by its buoyancy, the plume can rise to several hundred meters above the seafloor, where the plume becomes neutrally buoyant and starts to spread laterally. Hydrothermal plumes are an important vector for transporting the chemicals released from a vent site to the abyssal ocean (Lavelle and Wetzler, 1999; Jackson et al., 2010). Hydrothermal plumes are also a vector for dispersing larvae of vent fauna, which is key to the survival and genetic connectivity of vent organisms whose habitats are temporary with lifetimes as short as decades and are often separated by tens to hundreds of kilometers (Mullineaux and France, 1995; Mullineaux et al., 2005; Jackson et al., 2010).

In addition, some studies suggest hydrothermal plumes can even drive mid-depth ocean circulation (Stommel, 1982; Helfrich and Speer, 1995).

Although 'black smokers' are probably the most memorable feature of hydrothermal circulation, recent studies suggest they only account for a small part of the total heat and mass transports of hydrothermal circulation, with most of the transport attributed to diffuse low-temperature venting (Mottl, 2003). It is estimated that high-temperature venting only accounts for 20% of the magmatic heat available along mid-ocean ridge axes and the rest of the heat is likely transported through diffuse flows (Nielsen et al., 2006). Unlike high-temperature venting, which mostly occurs on zero-age ocean crusts (e.g., the crest of a mid-ocean ridge), there is evidence suggesting diffuse low-temperature venting continues from zero to 60 million year old crust (Stein and Stein, 1994). Moreover, it is estimated that the heat transported by low-temperature venting on 1 to 60 million year old crust likely accounts for more than 70% of the global hydrothermal heat transport (i.e. the rate at which heat is injected from the Earth interior into the ocean through hydrothermal discharges) (Mottl, 2003). The partitioning of heat transport between high and low temperature venting in different mid-ocean ridge settings has been a topic of active debate in recent decades. In addition to being the dominant contributor to global hydrothermal heat transport, diffuse low-temperature venting supports the majority of vent organisms. Therefore, dense biological coverage is often used as an indicator to locate diffuse flows in a vent field (Bemis et al., 2012; Luther et al., 2012).

The majority of seafloor hydrothermal vent sites discovered to date are along mid-ocean ridge axes (German and Seyfried, 2014). A ridge-axis hydrothermal system is a focal point of intimate interconnections among hydrothermal, geological, oceanic, and biological processes. Studying these interconnections is important for understanding the role of hydrothermal activities in the Earth-ocean system. Recent decades have seen mounting evidence of the significant impacts of tidal forcing, ocean currents, geological events, and atmospheric forcing on a ridge-axis hydrothermal system. Tidal oscillations have been observed in time-series observations of temperature, chemical composition, and flow rate of hydrothermal effluents in many cases (e.g., Schultz et al., 1992, 1996; Larson et al., 2007; Crone et al., 2010; Tivey et al., 2002; Rona et al., 2006; Barreyre et al., 2014). Significant

perturbations of hydrothermal discharge by geological events such as submarine volcanic eruptions, non-eruptive dike intrusions, and earthquakes of magmatic or tectonic origin have been reported in many studies (e.g., Sohn et al., 1998; Johnson et al., 2000; Lilley et al., 2003; Larson et al., 2009; Baker et al., 2012). More recently, some studies reported significant influences of wind-driven inertial oscillations and surface mesoscale eddies on the dynamics of a hydrothermal plume and bottom currents around a vent site (e.g., Adams et al., 2011; Xu et al., 2013). All these studies are based on time-series observations of seafloor hydrothermal discharge, which are key to studying the evolution of a hydrothermal system on a range of time scales beyond the capacity of ship-based discrete field visits.

Despite their importance, conducting long-term, time-series measurements of the geochemical properties (e.g., temperature, chemical composition, flow rate, heat transport) of seafloor hydrothermal discharge has been a daunting task faced by vent researchers. The difficulty is largely due to the remoteness of most seafloor hydrothermal vent fields (hundreds of kilometers from shore, thousands of meters deep), which makes them technically challenging and logistically expensive to access. Furthermore, designing a self-contained instrument that can record data continuously for a prolonged time period in the harsh environment of a typical hydrothermal vent site (e.g., great pressure, closeness to high temperature, caustic hydrothermal effluents) is engineeringly challenging. Most recently, the advent of cabled seafloor observatories at ridge-axis hydrothermal systems has provided important platforms for scientists to monitor a seafloor hydrothermal system using interdisciplinary real-time time-series observations—a luxury beyond the scope of traditional oceanographic methods (Kelley et al., 2014). In this dissertation, we use the data recorded by the instruments connected to a cabled seafloor observatory to investigate the interconnections between a ridge-axis hydrothermal system with the processes spanning from the Earth interior to the sea surface. The corresponding results and findings are a testament to the robustness and effectiveness of a seafloor observatory as a platform for interdisciplinary, long-term, continuous data collection.

1.2 Study Area

1.2.1 Endeavour Segment

The hydrothermal system studied in this dissertation work is located on the Endeavour Segment of the Juan de Fuca Ridge—an intermediate spreading center between the Pacific plate and the Juan de Fuca plate (Figure 1.1). Endeavour is a 90 km long segment located on the northern half of the ridge between the Cobb Segment to the south and Middle/West Valley to the north (Karsten et al., 1986; VanArk et al., 2007; Kelley et al., 2012). The Endeavour Segment is flanked by chains of abyssal hills expanding up to 15 km away from the axis at an average interval of 6 km (Figure 1.2). The central part of the segment is a 25 km long volcanic high cleaved by an axial valley that is 75-200 m deep and 0.5 to 1 km wide. The central 15 km long portion of the axial valley hosts 5 major hydrothermal vent fields and numerous small fields. From south to north, those 5 major vent fields are Mothra, Main Endeavour Field (MEF), High Rise, Salty Dawg, and Sasquatch (Figure 1.2). Some more recently discovered small fields include but are not limited to Raven and Stockwork along with several distal, diffuse-flow fields such as Cirque, Dune, Clam Bed, and Quebec. The valley is narrowest immediately south of the MEF and broadens towards north and south. The floor of the valley slants upward from the southern end ($\sim$ 2300 m depth) till a sill 12 km to the north ($\sim$ 2150 m) before it plunges toward the northern end ($\sim$ 2190 m). The intense hydrothermal venting, lush vent ecosystems, and elevated level of seismicity at Endeavour attract researchers from a broad range of disciplines, making it one of the best-studied ridge systems in the world (Kelley et al., 2012). Endeavour was a major study site of the Ridge Interdisciplinary Global Experiments (RIDGE) of the National Science Foundation (NSF), the Ridge 2000 Program funded by NSF and the W. M. Keck Foundation, and the Vents Program of the National Oceanic and Atmospheric Administration (NOAA). Most recently, Endeavour was chosen as the major volcanic study site of the NEPTUNE (North East Pacific Time-series Underwater Networked Experiments) observatory installed via Ocean Networks Canada. NEPTUNE combined with the Cabled Array at Axial Seamount installed via NSF's Ocean Observatory Initiative (OOI) form the world's first plate-scale cabled observatory (Figure 1.3) (Kelley et al., 2014).

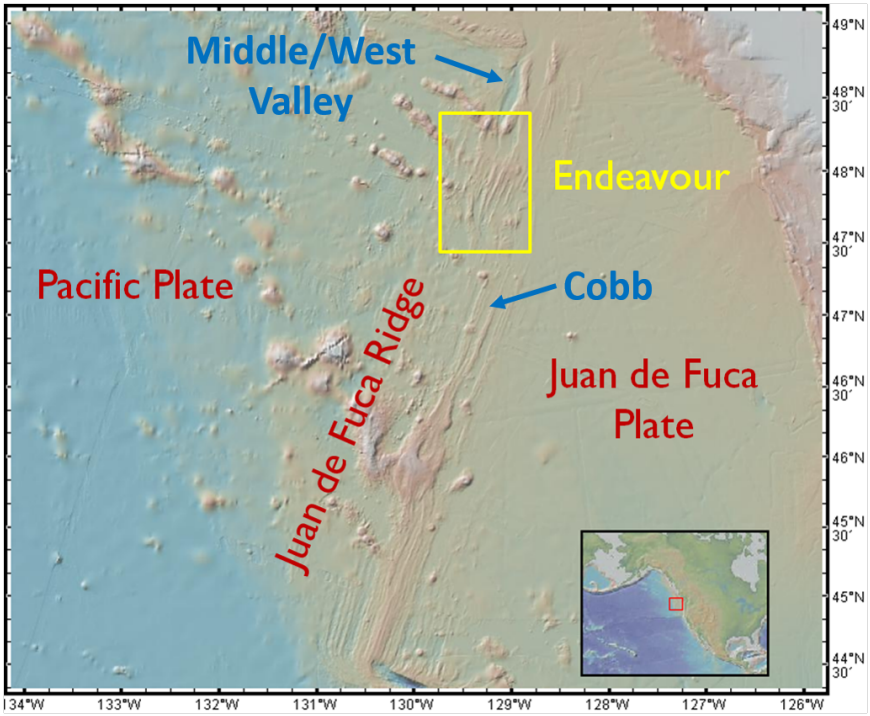

Figure 1.1: The Juan de Fuca Ridge and the Endeavour Segment (yellow block). The locations of the Middle/West Valley and Cobb Segments are also marked. Figure produced using GeoMapApp (http://www.geomapapp.org) (Ryan et al., 2009).

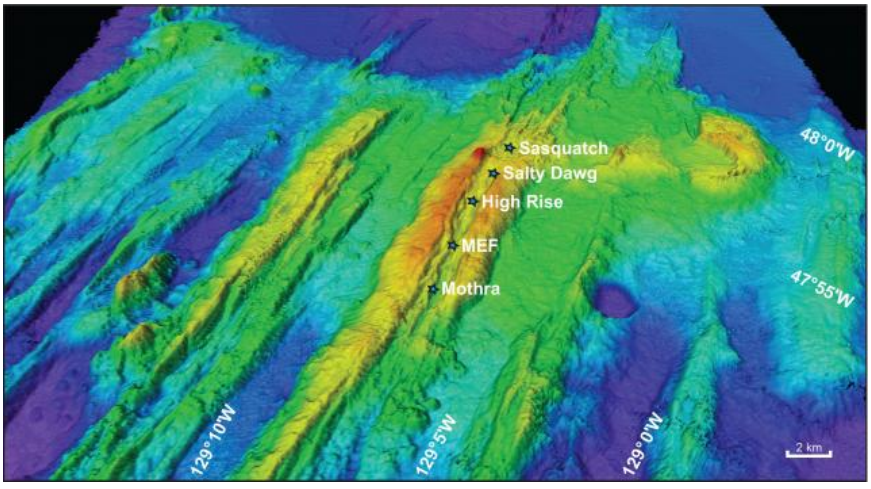

Figure 1.2: Bathymetry of the Endeavour Segment. The locations of the five major vent fields within the central axial valley are marked. Figure reproduced from Figure 1(b) in Glickson et al. (2007).

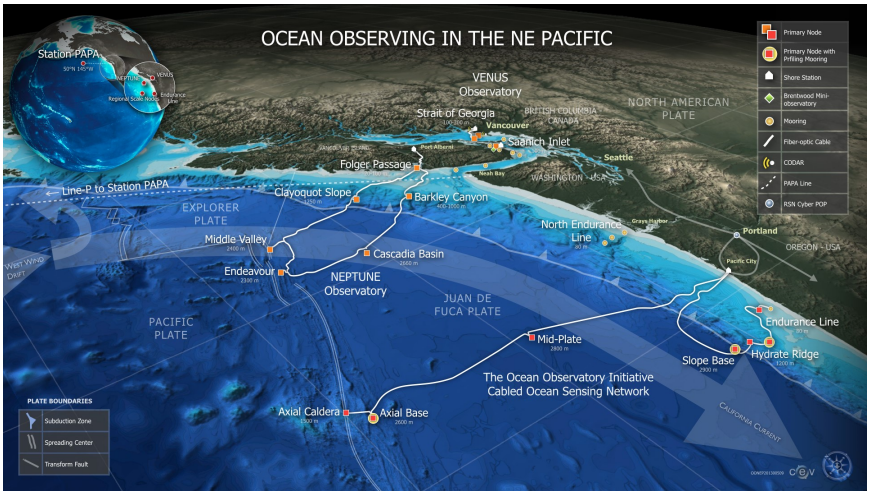

Figure 1.3: Map showing the two cabled observatories: NEPTUNE and the Cabled Array that are currently operating in the Northeast Pacific (courtesy of Ocean Observatories Initiative).

The seismic activity at the Endeavour Segment has been closely monitored since 1991 when the data recorded by the US Navy's Sound Surveillance System (SOSUS) became accessible to civilian research groups. The SOSUS record discontinued in 2008 after several key elements of the system went offline. The 20-year time series of seismic and volcanic events recorded by SOSUS suggests Endeavour has elevated background seismicity relative to the rest of the Juan de Fuca Ridge which is largely aseismic (Dziak et al., 2011). The increased rate of seismicity at Endeavour is likely a result of the reorganization of plate boundaries driven by the presence of an unstable triple junction at the northern end of the Juan de Fuca Ridge (Dziak et al., 2011). In addition to the SOSUS system, a local ocean bottom seismometer (OBS) system named Keck was deployed along the central Endeavour Segment from 2003 to 2006 to monitor local microearthquakes with high spatial resolution (Wilcock et al., 2009). The seismic data recorded by the Keck network revealed a remarkable correlation between the rate of local seismicity and hydrothermal heat output (Wilcock et al., 2009). Most of the detected microearthquakes lie in a cluster beneath High Rise and the MEF, the two most vigorous Endeavour vent fields that historically have the highest hydrothermal heat transports (Kellogg, 2011). This finding points to the intimate linkage between seismicity and hydrothermal venting at Endeavour.

1.2.2 Main Endeavour Field

Among the five major vent fields at Endeavour, the Main Endeavour Field (MEF) has been a focus of extensive studies since its discovery in 1982 (Tivey and Delaney, 1986). The MEF was the bull's-eye of the Endeavour Integrated Study Site (ISS) of the Ridge 2000 program and is a primary node of the NEPTUNE observatory at Endeavour (Figure 1.4). Located near the western boundary wall of the axial valley at depths between 2000 and 2200 m, the MEF hosts a total of 21 venting sulfide edifices with the highest venting temperature between 370 and 390 °C (e.g., Clague et al., 2008, 2014; Delaney et al., 1992). The geographical distributions of those sulfide edifices form two clusters in the north and south. Besides the active sulfide structures, the vent field is flanked to the east by a 500 m long band of extinct sulfide deposit (Figure 1.5). By dating the sulfide samples collected from the MEF using $^{226}Ra/Ba$ ratio, (Jamieson et al., 2013) suggests hydrothermal venting at the MEF has continued for at least 2400 years. The venting temperature, salinity, and chemistry at the MEF had remained relatively stable since its discovery in 1982 until the 1999-2000 earthquake swarms (Butterfield et al., 1994; Bohnenstiehl et al., 2004; Lilley et al., 2003). The data collected before the event show significant inner-field salinity and temperature gradients. The vent fluids in the south had higher temperature and much lower salinity compared to the vent fluids in the north (Butterfield et al., 1994). The 1999-2000 event significantly reduced such inner-field salinity and temperature gradients and changed the chemical concentrations of vent fluids across the vent field (Lilley et al., 2003; Seyfried et al., 2003).

Hydrothermal heat transport from the MEF was measured in several previous studies. The measurements made before the 1999-2000 earthquake swarms were $70 - 239$ MW by Bemis et al. (1993) and 364 ± 73 MW by Ginster et al. (1994), both of which were made on the same cruise in 1988. The difference between the two measurements is likely due to the different techniques applied and the uncertainty caused by extrapolating the measurements made at a limited number of vents to the entire vent field. After the earthquake swarms, in 2000, a hydrographic survey using an autonomous underwater vehicle (AUV) named the Autonomous Benthic Explorer (ABE) estimated the total heat transport from the MEF to

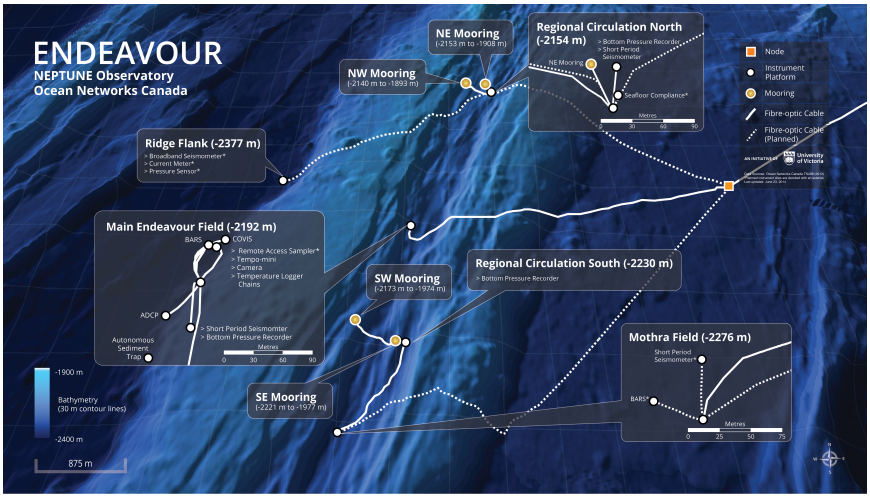

Figure 1.4: Map showing the NEPTUNE observatory at the Endeavour Segment (courtesy of Ocean Networks Canada).

be 629 ± 68 MW. In 2004, another hydrographic survey using ABE found the total heat transport decreased by $> 50\%$ compared with the 2000 measurement to 297 ± 29 MW (Thompson et al., 2005; Kellogg, 2011). Both the 2000 and 2004 surveys suggested the sulfide edifice cluster in the north accounts for $> 80\%$ of the total heat transport from the MEF (Kellogg, 2011). The partitioning of heat transport between high-temperature focused vents and low-temperature diffuse flows at the MEF was initially estimated by Schultz et al. (1992) to be $1 : 5$ with diffuse discharge being the dominant form of convective heat output in 1988. In contrast, the 2000 survey using ABE suggested the heat was partitioned approximately equally between focused and diffuse sources (Veirs et al., 2006). Later on, Pruis (2004) extrapolated the near-bottom temperature and vertical flow rate data recorded at the MEF in the Thermal Grid Project from 2000-2003 (Johnson et al., 2002) for an estimated diffuse flow heat transport of 6 to 58 MW. This estimate accounts for 2 to 20% of the total hydrothermal heat transport from the MEF measured in 2004 (Thompson et al., 2005; Kellogg, 2011). Those previous estimates suggest the contribution of diffuse flows to the hydrothermal heat transport from the MEF decreased dramatically between 1988 and 2004. Although such a decrease could be an artifact due to the large uncertainties of those estimates, it is consistent with the observation of the waning of diffuse flow sites in the southern cluster of MEF (Kelley et al., 2012).

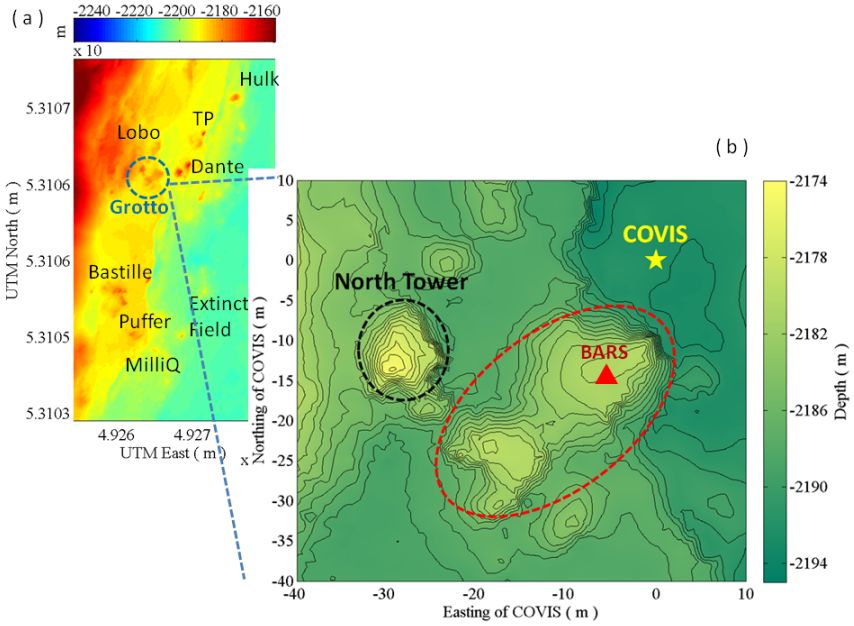

Figure 1.5: (a) High-resolution ($\sim$ 1 m) bathymetric map of the Main Endeavour Field. The blue dashed circle delimits the area of the Grotto mound. (b) Bathymetric map of the Grotto mound. The contour line interval is 1 m. The yellow star marks the location of COVIS. Black and red dashed lines delimit the area of the North Tower and the elliptical edifice respectively. The red triangle marks the location of the Benthic and Resistivity Sensors (BARS). The bathymetric data used to produce the maps in (a) and (b) was collected during an AUV survey in 2008 with $\sim$ 1 m lateral resolution and $\sim$ 0.1 m vertical resolution (Clague et al., 2008, 2014). This figure is reproduced from Figure 2 in (Xu et al., 2014).

1.2.3 The Grotto Mound

The primary study site of this research is the Grotto mound in the MEF. Grotto is a large venting sulfide structure (area $\sim 450\,m^2$) within the northern cluster of MEF, close to the western wall of the axial valley (Figure 1.5). Grotto consists of an elliptical edifice with NE-SW major axis in the east and a 10 m tall cylindrical edifice named the North Tower near the western rift valley wall. The two edifices are connected by a saddle which is approximately 5 m wide and 5 m tall. The eastern end of the elliptical edifice stands close to the edge of a fault with $\sim$ 4 m throw (Figure 1.5) (Rona et al., 2015). Grotto is one of the most hydrothermally active structures in the MEF. Of the two edifices of Grotto, the North Tower hosts the most vigorous venting, with five to six 'black smokers' on the summit and diffuse flows percolating through the base of, on the sides of, and around the summit of the edifice (Figure 1.6). The elliptical edifice hosts several 'black smokers' discharging relatively small plumes at the eastern end. Diffuse flows percolate through areas around those smokers and on the saddle connecting the two edifices (Rona et al., 2015).

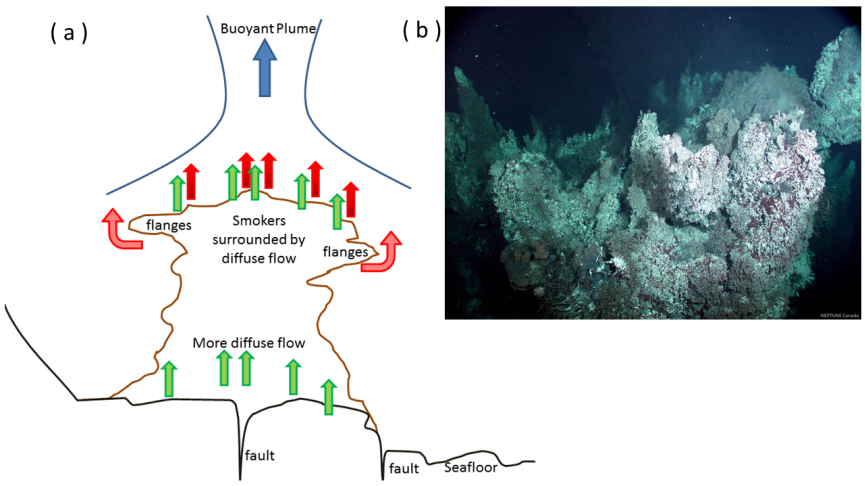

Figure 1.6: (a) Structure diagram of the North Tower of Grotto illustrating the interplay of the different modes of venting. Diffuse flow is ubiquitous, most of the flanges are on the upper edges of the steep sides, and most of the smokers are on the summit of the sulfide edifice. Faults are indicated below the edifice as that is the inferred sub-surface fluid pathway (reproduced from Figure 4 in Rona et al. (2015)). (b) Photo of the summit of the North Tower of Grotto (photo courtesy of Ocean Networks Canada).

1.3 The NEPTUNE Observatory at Endeavour

The Grotto mound is a major study site of the MEF node of the NEPTUNE observatory. The observatory connects multi-disciplinary instruments located on or near Grotto (Figure 1.4). These instruments include but are not limited to the Cabled Observatory Vent Imaging Sonar (COVIS), the Benthic and Resistivity Sensors (BARS), the Remote Access Water Sampler (RAS), Tempo Mini, an acoustic Doppler current profiler (ADCP), and an ocean bottom seismometer (OBS). The following is a summary of the locations and functions of those instruments.

COVIS is an acoustic imaging sonar deployed 30 m to the northeast of the North Tower of Grotto. COVIS quantitatively monitors the black-smoker and diffuse-flow discharges from Grotto using acoustic signals (see Section 1.4 for more details) (Figure 1.7).

BARS is a temperature and chemical sensor deployed at a 'black smoker' on the elliptical edifice of Grotto. The probe of BARS is located within the throat of the orifice, which measures the temperature, resistivity (a proxy for chloride concentration), and oxidation/reduction potential of hydrothermal fluids inside the vent.

RAS is a water sampler deployed at a diffuse flow site on Grotto that is close to the vent instrumented by BARS. RAS takes samples following a pre-programmed schedule or instantaneous user commands. The sampled fluid is pumped from the outlet of a bell-shaped dome that covers a patch of diffuse flow discharge into the bottles suspended above the edifice. The bell-shaped dome minimizes the mixing of the ambient seawater with the sampled fluid, whose temperature is measured by a thermistor inside the dome.

Tempo Mini is a video camera designed by Ifremer in France, which is located on the elliptical edifice of Grotto near the diffuse flow site instrumented by RAS. This innovative system also has an oxygen sensor, a colorimetric sensor to measure iron concentrations in fluids, and a 10-m long, 10-sensor temperature array to measure the chemical signature and temperature in the macro-fauna colony monitored by the camera.

ADCP is located approximately 50 m to the south of Grotto. It measures the amplitude and direction of the currents within 50 m above the seafloor.

OBS named KEMF is inserted into a drill hole on a piece of basalt outcrop close to the ADCP, which monitors the background seismic activity.

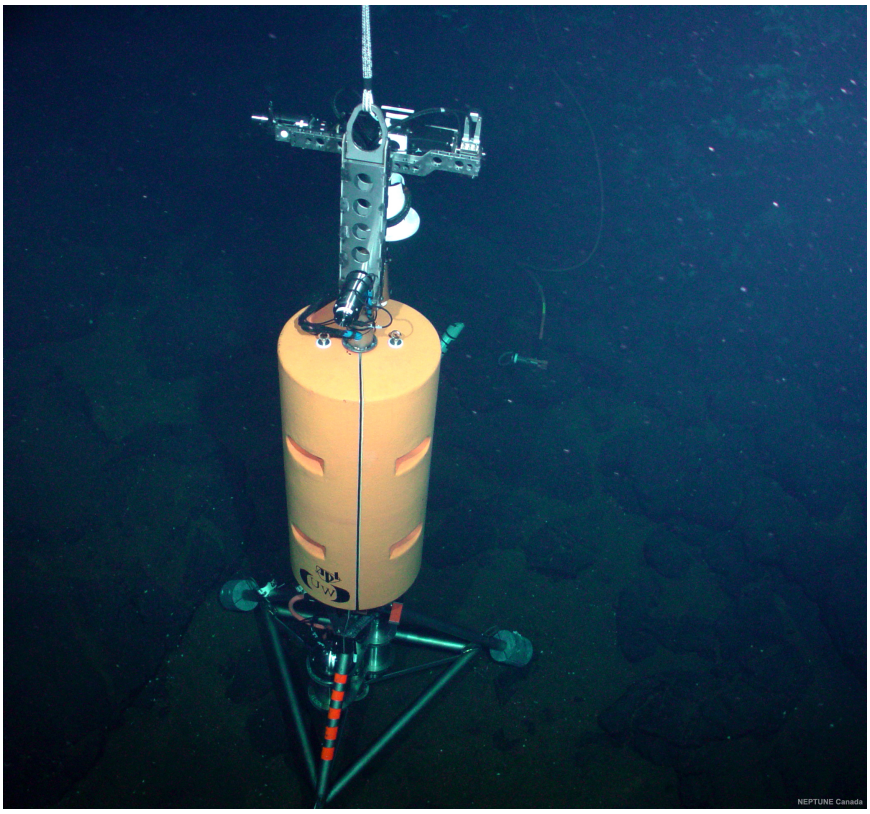

Figure 1.7: Photo of COVIS on the seafloor (photo courtesy of Ocean Networks Canada).

The high-power (up to 10 kW) high-bandwidth (10 Gbs) fiber-optic cables of the NEPTUNE observatory provide continuous, real-time, two-way data communication to the aforementioned and other observatory instruments. The Ocean Networks Canada's Data Management and Archiving System (DMAS) stores the data received from those instruments and publishes them in real time in an on-line database for scientists and the general public to access and download. The data recorded by COVIS and other NEPTUNE instruments presented in this dissertation are courtesy of Ocean Networks Canada.

1.4 Cabled Observatory Vent Imaging Sonar

In September of 2010, the Cabled Observatory Vent Imaging Sonar (COVIS) was installed in the MEF node of the NEPTUNE observatory at Endeavour to quantitatively monitor the hydrothermal plumes from both focused and diffuse sources at the Grotto mound (Rona and Light, 2011; Bemis et al., 2015). COVIS was deployed at 47°57′ N, 129°6′W, approximately 30 m to the northeast of the North Tower of Grotto, and 2197 m depth looking in the southwest direction (Figure 1.5). COVIS scans the hydrothermal discharges from Grotto every three hours in three different modes semi-simultaneously for 3-D plume imaging (Imaging mode), volume transport and flow rate quantification (Doppler mode), and 2-D diffuse-flow mapping (Diffuse Flow mode). The primary component of COVIS is a state-of-the-art imaging sonar, a variant of the Seabat 7125 developed by Reson, Inc.. The sonar has two transmitting/receiving pairs: a 400 kHz pair used in Imaging and Doppler modes, and a 200 kHz pair used in Diffuse-Flow mode. The following is a synopsis of the data acquisition in each mode (Bemis et al., 2015).

Imaging

During each scanning cycle, the 400 kHz transmitter-receiver pair on COVIS first rotates upward from $\theta = 19°$ to 59° above the horizontal plane in 1° increments and then downward in 1° increments to the initial position. The combination of the upward and downward rotation processes is called a sweep, which covers a 40 m thick water column immediately above Grotto. At each 1° step in the upward and downward halves of a total sweep, the transmitter-receiver pair stops to transmit 6 pulses of 396 kHz acoustic signals with 0.5 ms pulse-width at a rate of 2 pulses per second. Applying a conventional beam-forming technique, the receiver array records the backscatter of each pulse through a 'fan' composed by 256 beams with 0.5° (azimuthal) $\times$1° (orthogonal) beam-width that extend to 75 m away from the sonar (see Figure 1.8 for geometry). Multiple transmissions (to be averaged), data acquisition and storage, and mechanical rotation of the sonar (with instantaneous rotation speed $\sim 1°/s$) result in a combined upward and downward rotation (a total sweep) time of 8 min.

Doppler

Similar to Imaging Mode, a Doppler-mode scanning cycle comprises an up-and-down sweep of the sonar from $\theta = 20^\circ$ to 57° in 1° increments. At each 1° step, the 400 kHz transmitter-receiver pair stops to transmit 40 pulses of 396 kHz acoustic signals with 1.5 ms pulse-width at a rate of 2 pulses per second. The receiver array then records the backscatter following the beam pattern in Imaging mode (Figure 1.8). Multiple transmissions (to be averaged), data acquisition and storage, and mechanical rotation of the sonar (with instantaneous rotation speed $\sim 1^\circ$/s) result in a combined upward and downward rotation (a total sweep) time of 43 min.

Diffuse Flow

During each scanning cycle, the 200 kHz transmitter-receiver pair on COVIS transmits 10 pulses of acoustic signals with 0.3 ms pulse-width at a rate of 5 pulses per second towards the sulfide edifices of Grotto while the sonar is looking in a near horizontal direction. The receiver array then records the backscatter of each pulse through 128 beams with 1° (horizontal) $\times 28^\circ$ (vertical) beam-width (see Figure 1.9 for geometry). Each scanning cycle takes approximately 3 second to finish.

For the backscatter data recorded in Imaging and Doppler modes, the spatial resolution along the acoustic line-of-sight is $R_r = \frac{cT_p}{2} \approx 0.4$ m (Imaging) or 1 m (Doppler), where $c = 1495$ m/s is the sound speed and $T_p = 0.5$ ms (Imaging) or 1.5 ms (Doppler) is the pulse-width. As the beams diverge, the elemental scanning volume of COVIS grows larger, causing resolution to become lower as range increases. For example, at 30 m range from COVIS (where the North Tower of Grotto is located), the azimuthal distance between two adjacent beams is $R_{az} \approx 0.3$ m with an orthogonal width of $R_f \approx 0.5$ m. As a result, the elemental scanning volume is $R_V = R_f R_{az} R_r \approx 0.06\,\mathrm{m}^3$ (Imaging) or $0.15\,\mathrm{m}^3$ (Doppler), which increases to $\sim 0.4\,\mathrm{m}^3$ (Imaging) or $1\,\mathrm{m}^3$ (Doppler) at 75-m range. In Diffuse-Flow mode, the horizontal azimuthal resolution is 1°. This results in an azimuthal distance between two adjacent beams of 0.5 m at 30 m range from COVIS. The spatial resolution along the acoustic line-of-sight is $\frac{cT_p}{2} \approx 0.2$ m where $T_p = 0.3$ ms.

In practice, we convert the amplitude of the backscatter data in Imaging and Doppler modes to acoustic volume backscattering coefficient s_v in units m^{-1} (i.e., backscattering

cross-section per unit solid angle per unit volume) based on the calibration factors given in Xu et al. (2013) (Appendix E) and target cross-section in units m^2 in Diffuse Flow mode. For Imaging-mode data, we interpolate s_v of the backscatter received through the 'fans' at successive 1° steps within a sweep onto a uniform 3-D rectangular grid with $40 \times 30 \times 45$ m dimensions and 0.5 m intervals in all three coordinates. To plot acoustic images of the buoyant plumes discharging from Grotto (Figure 1.8), we covert the gridded s_v to volume backscattering strength (S_v) by taking logarithm: $S_v = 10 \log_{10} s_v$. For Doppler-mode data, we estimate the flow rate, volume transport, and expansion rate of the buoyant plumes above Grotto from the Doppler-shift in the backscatter following the procedures described in Section 3.1 (Xu et al., 2013). For Diffuse-Flow-mode data, we apply the acoustic scintillation thermography (AST) method described in Rona et al. (1997) to detect and map the diffuse-flow areal distribution based on the decorrelation between the backscatter from consecutive pules (Rona et al., 2015).

1.5 Motivation

A ridge-axis hydrothermal system resides in a dynamic environment where myriad processes of geological, oceanic, and atmospheric natures (e.g., earthquakes, tides, ocean currents, surface-generated eddies) have been found to have significant influences on local hydrothermal venting (e.g., Sohn et al., 1998; Lilley et al., 2003; Larson et al., 2009; Baker et al., 2012; Larson et al., 2007; Crone et al., 2010; Rona et al., 2006; Barreyre et al., 2014; Adams et al., 2011). Furthermore, previous studies suggested hydrothermal cooling of the oceanic crust can cause microseismicity beneath the ridge axis (e.g., Tolstoy et al., 2008) and the buoyant hydrothermal plumes can drive local circulation (e.g., Thomson et al., 2003). Therefore, instead of being a remote, isolated niche in the deep ocean, a ridge-axis hydrothermal system is a hot spot of interactions among geological, oceanic, atmospheric, and hydrothermal processes. Studying these interactions is key to understanding the role of hydrothermal processes in the Earth-ocean system—a long-term goal of hydrothermal vent research. Driven by this goal, this dissertation aims to address the question of how the heat transport and fluid discharge from a ridge-axis hydrothermal system change in time and react to geological events in the Earth interior, ocean currents in the water column, and atmospheric forcing

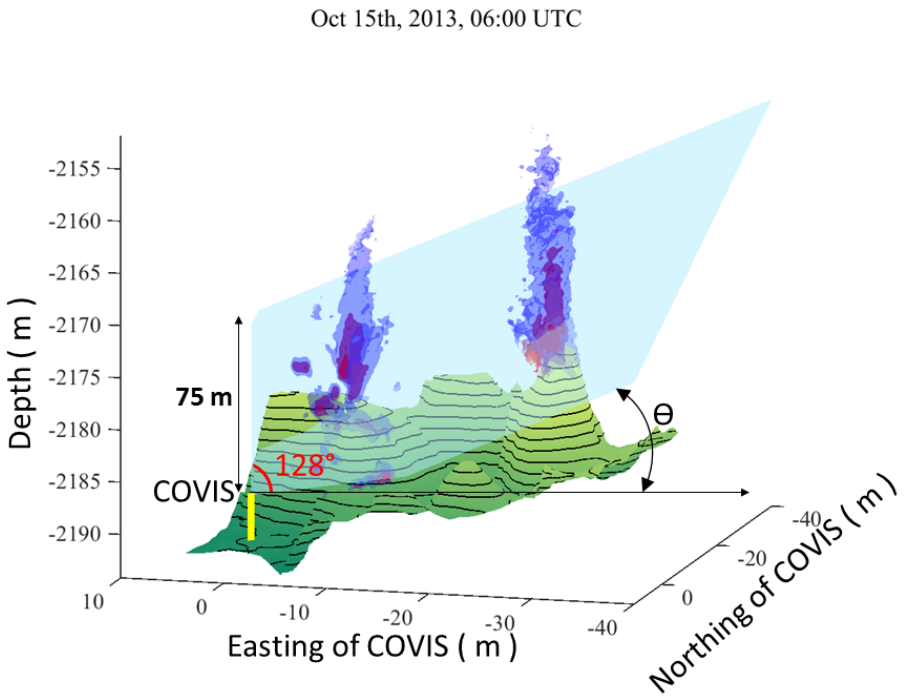

Figure 1.8: 3-D image of the black-smoker plumes above the bottom topography of Grotto (contours in 1 m intervals) produced by processing the COVIS Imaging data collected on October 15th, 2013 at 06:00 UTC time. The bathymetric data used to produce the bottom topography was collected during an AUV survey in 2008 (Clague et al., 2008, 2014). COVIS (yellow bar) scans the plumes with an acoustic beam of 128° azimuthal coverage. Within one scanning cycle, the sonar rotates up and down from $\theta = 19°$ to 59° (Imaging mode) or $\theta = 20°$ to 57° (Doppler mode) from the horizontal plane in 1° increments. The slanting plane in the figure illustrates the acoustic beam at $\theta = 30°$. The isosurfaces of the plumes correspond to volume scattering strength (S_v) as: -50 dB (red), -60 dB (magenta), -70 dB (blue).

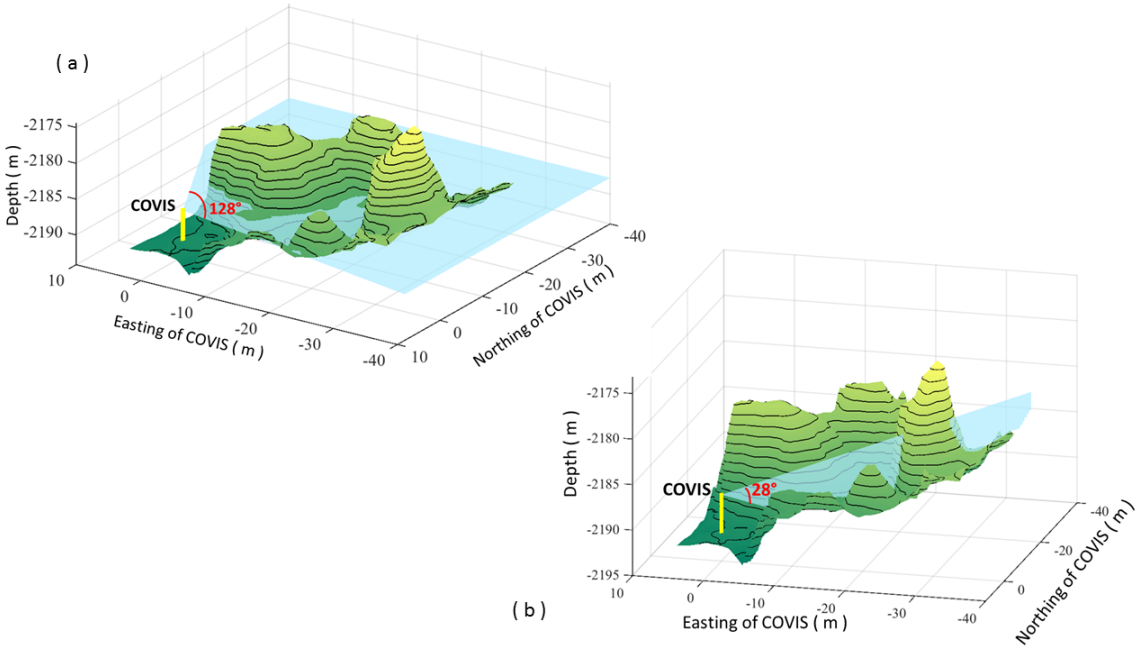

Figure 1.9: Schematic diagram illustrating a Diffuse-Flow scan. The acoustic beam applied has 128° horizontal beam-width (a) and 28° vertical beam-width (b). The bottom topography of the Grotto mound (contours in 1 m intervals) is produced from the bathymetric dataset collected during an AUV survey in 2008 (Clague et al., 2008, 2014).

on the sea surface. On different spatial scales, the 'hydrothermal system' in the aforementioned question can refer to the hydrothermal processes in the global ocean, on a ridge segment (e.g., Endeavour), in a vent field (e.g., Main Endeavour Field), or at a venting sulfide structure (e.g., the Grotto mound). Although finding global answers to those questions is the ultimate goal, resolving them on the smallest scale (e.g., a venting sulfide structure) is more tangible and practical. In this dissertation, our goal is to bring insights into the aforementioned questions for the hydrothermal processes at the Grotto mound in light of the observational data recorded by COVIS and other NEPTUNE observatory instruments. The following is a detailed discussion of the motivation behind this research.

In water, light attenuates rapidly, yet sound propagates to much greater distance. Therefore, acoustics has become a crucial tool for oceanographic research. In numerous studies, scientists use acoustic methods to obtain quantitative information of myriad oceanic phenomena such as currents, turbulence, suspended sediments, hydrothermal plumes, just to name a few (Thomson et al., 1989; Ross and Lueck, 1992; Lavery et al., 2013; Thorne and Meral, 2008; Rona et al., 2002, 2006; Xu and Di Iorio, 2012; Bemis et al., 2015).

COVIS is an innovative acoustic instrument that images and quantitatively monitors hydrothermal plumes using backscattered acoustic signals (Rona and Light, 2011; Xu et al., 2013, 2014; Rona et al., 2015; Bemis et al., 2015). Several mechanisms can potentially produce the acoustic backscatter observed in the plume image (Figure 1.8), among which suspended particles and temperature fluctuations are the two potential major scatterers (Xu and Di Iorio, 2011). Although processing and interpreting COVIS data does not require precise knowledge of the scattering mechanisms, determining the dominant mechanism is important for the selection of correct acoustic models that can potentially convert the acoustic data to powerful tools for remote sensing of the properties of either the particles or the temperature field within the plumes imaged by COVIS.

Long-term, time-series observations are requisite for studying the temporal variations of a hydrothermal system that span a broad range of time scales (e.g., hours to years). Almost all the previous time-series measurements of seafloor hydrothermal discharge were conducted either close to the orifices of 'black smoker' vents or right on top of diffuse flow patches. While those data are important for studying the properties of the end-member hydrothermal

fluids and the gross output from a hydrothermal system, they provide little information on the evolution of the buoyant plumes above the vents and the interactions of the plumes with the hydrodynamical processes in the ambient water column. Studying how a buoyant hydrothermal plume interacts with its ambient environment is key to understanding the dispersal of the vent-generated materials (e.g., dissolved and particulate minerals) from a vent field to the abyssal ocean, which has profound implications on the contribution of hydrothermal venting to the geochemical budget of the global ocean.

The successful installation of COVIS in the NEPTUNE observatory has provided vent researchers an unprecedented opportunity to study the temporal variations of a ridge-axis hydrothermal system (Rona and Light, 2011; Bemis et al., 2015). The long-term time series of the hydrodynamical properties (volume transport, flow rate, and expansion rate) of the largest buoyant plume above Grotto obtained using COVIS is a powerful tool for studying the temporal variations of a buoyant hydrothermal plume over time scales ranging from hours to years (Xu et al., 2013; Bemis et al., 2015). In conjunction with the contemporaneous time-series measurements of the ambient ocean currents and the geochemical properties (e.g., temperature, chemical composition) of the hydrothermal effluents from a 'black smoker' vent and diffuse flow patches on Grotto using other observatory instruments, the COVIS time-series measurements can help form an integrated view of the hydrothermal activity at Grotto and in particular the interaction of the buoyant hydrothermal plume with ambient hydrodynamic processes (Xu et al., 2013).

Quantifying the heat transports from hydrothermal systems has been a long-term goal of vent researchers (Baker, 2007; Di Iorio et al., 2012). This is by no means an easy task because of the world-wide distribution, spatial and temporal variability, and various venting types of hydrothermal systems. Most vent fields discovered to date are located more than hundreds of kilometers off coasts and thousands of meters below the sea surface, making them expensive and laborious to access. Such remoteness of vent fields largely contributes to the limited number of field measurements of hydrothermal heat transport (see compilation in Ramondenc et al. (2006); Baker (2007)). Previous attempts to measure hydrothermal heat transport were made over spatial scales ranging from ridge segments (e.g., Thompson et al., 2005) to vent fields (e.g., Bemis et al., 1993; Ginster et al., 1994; Stahr et al., 2000) and

individual venting sulfide structures (e.g., Germanovich et al., 2009; Xu and Di Iorio, 2012; Xu et al., 2014). Baker (2007) gives a comprehensive summary of the previous heat transport measurements and the corresponding methods applied. Although large-scale heat-transport measurements (e.g., over an entire ridge segment) are key to quantifying the contribution of hydrothermal systems to the heat budget of the global ocean, fine measurements on smaller scales (e.g., a vent field or a venting sulfide structure) are more important to address the spatial and temporal variation of hydrothermal systems and the heat partitioning among different venting types (e.g., 'black smokers', diffuse flows).

Previous heat transport measurements on a vent-field or sulfide-structure scale were based on either point measurements at individual vents on the seafloor or observations of hydrothermal plumes in the water column (Baker, 2007; Di Iorio et al., 2012; Rona et al., 2015). The heat transport of a vent field measured using different methods can differ by up to on order of magnitude (see compilation in Ramondenc et al. (2006); Baker (2007)), reflecting the large uncertainties of those measurements. Moreover, previous heat transport measurements were mostly snapshots obtained during infrequent field visits and were thus insufficient to study the temporal variation of a hydrothermal system on short time scales (e.g., days, months) and the immediate response of the system to external perturbations (e.g., tidal forcing, seismic/volcanic events) (Ramondenc et al., 2006; Baker, 2007; Bemis et al., 2012; Rona et al., 2015). Addressing this question requires long-term time-series heat transport measurements with reasonable accuracy, which have rarely been achieved to date (Goto et al., 2003; Xu et al., 2014).

In light of the long-term time series of the hydrodynamical properties (volume transport, flow rate, and expansion rate) of the buoyant plume above Grotto obtained using COVIS, we have developed an inverse method of estimating the heat transport driving the plume from its volume transport estimates. The resulting long-term (> 3 years) high-resolution (averaged sampling rate > 1 per day) time series of hydrothermal heat transport, in conjunction with the contemporaneous seismic data recorded by an observatory seismometer, is a powerful tool for studying the temporal evolution of the heat source driving the hydrothermal venting at Grotto and its response to seismic/volcanic events (Xu et al., 2014).

1.6 Dissertation Structure

The following is a synopsis of the rest of this dissertation. Chapters 2, 3, and 5 are adapted form three self-contained manuscripts, of which two have been published at the time of writing (Xu et al., 2013, 2014). Chapter 2 presents a detailed investigation of the dominant acoustic backscattering mechanism within the buoyant plumes imaged by COVIS. The result is used to explore the potential of inverting the acoustic backscatter to get quantitative information on either the particles or temperature fluctuations within the plume. Chapter 3, adapted from Xu et al. (2013), presents a 26-day time-series of the hydrodynamical properties (volume transport, flow rate, expansion rate) of the largest buoyant plum above Grotto obtained by processing the Doppler-mode data recorded by COVIS in September to October 2010. Further analyses of this time series sheds light on the linkage between the dynamics of a hydrothermal plume with the oceanic processes in the water column and the atmospheric forcing on the sea surface. Chapter 4 presents a 41-month (October 2011 to February 2015) extension to the time series presented in Chapter 3, which provides further evidence for the findings in Chapter 3 regarding the influences of ocean currents on the dynamics of a hydrothermal plume. Additionally, the plume bending observed in the 3-D acoustic images produced by COVIS is used to estimate the ambient horizontal currents in the immediate vicinity of Grotto. Comparing the result with the bottom currents measured by an ADCP sheds light on the complexity of the bottom currents within the vent field. Chapter 5, adapted from Xu et al. (2014), presents an inverse method of estimating the heat transport driving the buoyant plumes above Grotto and the resulting long-term high-resolution heat transport time series. This chapter also discusses the influence of seismic/volcanic events on hydrothermal venting at Grotto. Chapter 6 gives concluding remarks.

Chapter 2

The Relative Effect of Particles and Turbulence on Acoustic Backscatter from a Deep-sea Hydrothermal Plume

2.1 Introduction

Underwater acoustics, as an important remote-sensing tool of oceanographic research, has been applied in many hydrothermal studies (e.g., Rona et al., 1991, 2002, 2006; Di Iorio et al., 2005; Xu and Di Iorio, 2011, 2012; Xu et al., 2013, 2014; Bemis et al., 2002, 2015)). In these studies, researchers apply active acoustic techniques (e.g., acoustic scintillation, acoustic imaging) to acquiring quantitative information (e.g., flow rate, volume transport, heat transport, expansion rate, plume orientation, and areal distribution of hydrothermal discharge) of hydrothermal plumes by analyzing the scattered acoustic signals. The resultant acoustic measurements have the advantages of having no instrumental interference and large spatial scales over the data obtained using conventional instruments.

Acoustics is an effective tool for studying hydrothermal plumes because the plumes are strong sound scatterers due to the suspended particles and temperature fluctuations within them. However, the existence of multiple scattering mechanisms within a plume complicates the nature of the scattered acoustic signals, which has been ignored in most previous studies. Understanding the relative importance of different scattering mechanisms within a hydrothermal plume is important for the selection of appropriate acoustic models that can transform the existing acoustic techniques to tools of remote sensing of the properties of the suspended particles and temperature fluctuations within the plume. The dominance of temperature fluctuations within a hydrothermal plume as a scattering mechanism has been previously asserted by Xu and Di Iorio (2011), with strong observational evidence in the case of forward scattering. However, their result is inconclusive for backward scattering due to the lack of contemporaneous acoustic backscatter observation and direct measurements

of particle grain size.

In this study, we reconsider the relative importance of backscattering from particles and temperature fluctuations by theoretically estimating the acoustic backscatter from suspended particles based on the in-situ measurements of particle grain size and mass concentration. We then compare the theoretical estimate with the acoustic backscatter recorded by the Cabled Observatory Vent Imaging Sonar (COVIS) to determine the relative contribution of particles to acoustic backscatter from a hydrothermal plume. Furthermore, we explore the potential of inverting backscatter data to obtain information about the temperature fluctuations within a hydrothermal plume.

2.2 Observational Data Collection

2.2.1 Acoustic Imaging of Hydrothermal Plumes

The idea of acoustic imaging of hydrothermal plumes stems from the detection of plumes as sonar targets during a seafloor terrain survey at the East Pacific Rise (Palmer et al. (1986); Bemis et al. (2015)). During the following decades, acoustic imaging has come a long way from being a tool of visualizing hydrothermal plumes to a quantitative means of estimating multiple plume properties (e.g., radius, flow rate, volume transport, heat transport) (Bemis et al., 2015). COVIS is an innovative sonar system designed to image and quantitatively monitor seafloor hydrothermal plumes. In September 2010, COVIS was connected to the Ocean Networks Canada's NEPTUNE observatory to monitor the hydrothermal discharge from the Grotto mound, a hydrothermal sulfide structure on the Endeavour Segment of the Juan de Fuca Ridge in the Northeast Pacific (Rona and Light (2011); Bemis et al. (2015)). COVIS records acoustic backscatter data in three different modes: Imaging, Doppler, and Diffuse for visualizing (Figure 2.1), quantifying outflow transports of buoyant plumes, and mapping diffuse flows on Grotto respectively (Section 1.4). The rest of this chapter employs the backscatter data recorded in the Imaging and Doppler modes.

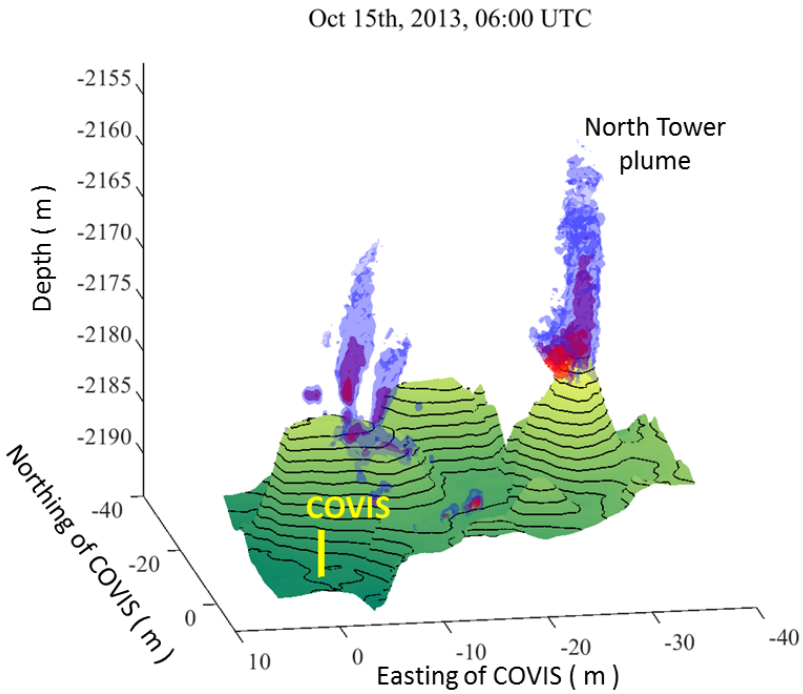

Figure 2.1: 3-D image of the black-smoker plumes above the bottom topography of Grotto (contours in 1 m intervals) produced by processing the COVIS Imaging data collected on October 15th, 2013 at 06:00 UTC time. The bathymetric data used to produce the bottom topography was collected during an AUV survey in 2008 (Clague et al., 2008, 2014). The yellow bars marks the location of COVIS. The isosurfaces of the plumes correspond to volume scattering strength (S_v) as: -50 dB (red), -60 dB (magenta), -70 dB (blue).

2.2.2 Plume Particle Samples

In order to estimate the contribution of suspended particles to the backscatter signals recorded by COVIS, we need to know the grain size distribution and mass concentration of the suspended particles within the plumes above Grotto. The rest of the section gives a brief summary of previous studies of hydrothermal plume particles and efforts of sampling the buoyant plumes above Grotto followed by a detailed description of the analyses of the particle samples taken from the major plume above the North Tower of Grotto (the larger plume in Figure 2.1, which we call the North Tower plume hereafter) in May 2014.

An iconic feature of a seafloor hydrothermal plume is the dark-hued 'smoke' particles that occur when hydrothermal fluids mix with ambient seawater. Previous studies of hydrothermal plume particles registered a wide range of particle mineralogy and size that vary considerably with the height above the vent where a sample was taken and the source conditions of the vent (e.g., temperature, flow rate, substrate crustal properties) (e.g., Feely et al., 1987, 1990, 1994, 1998; Walker and Baker, 1988; Mottl and McConachy, 1990; Gartman et al., 2014; Yucel et al., 2011). According to those studies, the 'smoke' particles mainly comprise metal-rich sulfide, sulfate, and oxide particles (e.g., pyrite, pyrrohotite, barite, sphalerite, chalcopyrite, anhydrite, iron oxyhydroxides). The grain sizes of those particles range from tens of nanometers to hundreds of microns. Among the studies cited above, only one reported particle mass concentration (Mottl and McConachy, 1990) and two reported particle size distribution (Walker and Baker, 1988; Feely et al., 1998). The mass concentration reported in Mottl and McConachy (1990), which was measured from the samples taken from several vent fields on the East Pacific Rise (EPR) near 21°N, ranges from approximately 2000 mg/L at 3 m above the vent to below 3 mg/L at greater than 20 m above the vent. Walker and Baker (1988) reported the volume-concentration size distributions (i.e. the fractional volume of plume fluid occupied by the particles having a given grain size) of a series of samples taken at 3 to 177 m above a vent on the Southern Symmetrical Segment on the Juan de Fuca Ridge (Figure 2.2). Feely et al. (1998) reported the size distributions measured from the particle samples taken from the event plumes generated after the 1996 magmatic intrusion on the Gorda Ridge (Figure 2.3). Note that those

previous measurements of particle mass concentration and size distribution were obtained from different vent systems whose particle properties are unlikely to be representative of those at Grotto. Therefore, obtaining realistic estimates of the particle mass concentration and size distribution at Grotto requires taking samples from the local plumes.

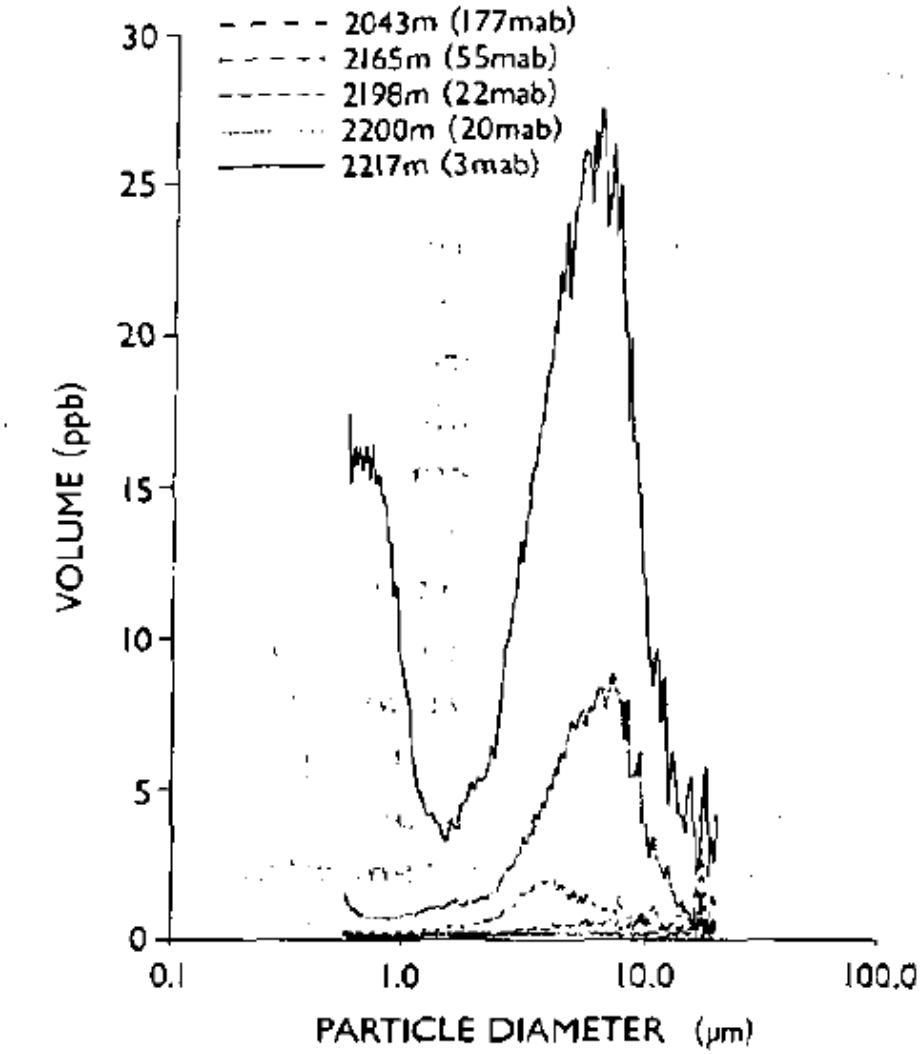

Figure 2.2: Volume-concentration size distributions measured from a series of particles samples taken at 3 to 177 m above a vent on the Southern Symmetrical Segment on the Juan de Fuca Ridge (figure reproduced from Figure 7 in Walker and Baker (1988)).

The particles in the buoyant plumes above Grotto were sampled on 5 cruises from 2011 to 2014. Spreadsheet A in the electronic supplementary materials of this dissertation

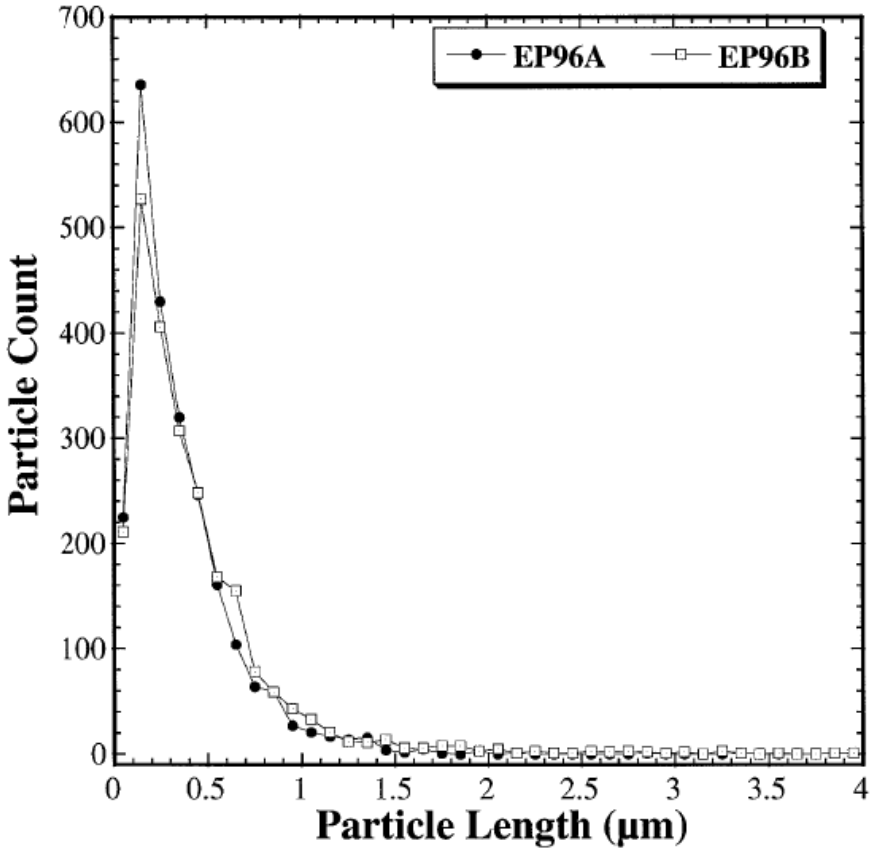

Figure 2.3: Discrete particle size distributions of two samples (EP96A and EP96B) taken from the event plume generated by 1996 magmatic intrusion event on the Gorda Ridge (figure reproduced from Figure 7 in Feely et al. (1998)).

summarizes the details of all samples. Among those samples, the ones taken on the 2014 cruise are considered best processed and preserved, and are thus used for the further analyses detailed below.

In May 2014, water samples were taken from the North Tower plume using two 2.5-L Niskin bottles carried by the remotely operated vehicle (ROV) ROPOS. The two Niskin bottles were fired at approximately 1 m above two most vigorous vents when the bottles were clearly submerged in the 'black smoke' (i.e. hydrothermal particles) carried by the plume. The presence of large amounts of plume particles and the relative low heights above the vents ensured the bottles were triggered in the close vicinity of the plume center. The water sample in each Niskin bottle was filtered aboard through one $0.2\,\mu$m Polycarbonate Isopore and three $0.02\,\mu$m Inorganic Anodisc membrane filters immediately after the Niskin bottles were back on deck. For the Isopore filters, 1 L of water sample was filtered through each filter, which had been acid-cleaned with 5% HCL solution and weighed before the cruise. For the three Anodisc filters used for each bottle, 70 ml of water sample was filtered through two filters respectively and 150 ml of water sample through the third one. A bottle was flipped up and down for 10 to 20 sec to remix the particles in the bottle every time before extracting fluid from it. After the filtration was complete, both the Isopore and Anodisc filters were rinsed with MilliQ water and placed in sealed mylar bags with oxygen absorbers. The mylar bags were kept in a $-20°C$ refrigerator during the rest of the cruise. After the cruise, the particle-laden filters were dried in a desicator purged with Nitrogen. Subsequently, the two Isopore filters were weighed using the same scale as pre-cruise weighing. The particle mass concentration is calculated as the weight increase of an Isopore filter divided by the volume of the filtered hydrothermal fluid (1 L). The resulting particle mass concentrations (M) are

$$\begin{aligned} M_{bottle1} &= 2.6\,\text{mg/L}, \\ M_{bottle2} &= 5.6\,\text{mg/L}. \end{aligned} \tag{2.1}$$

Note that the measurements above are much lower than those reported in Mottl and McConachy (1990), which have a maximum of approximately 2000 mg/L from a sample taken at 3 m above a vent on EPR near 21° N. Such a difference could reflect 1) the

EPR plume has much higher particle concentration than the North Tower plume and/or 2) the 2014 North Tower plume particle concentration measurements are underestimates. An underestimate of M could result from 1) samples taken outside the plume, 2) bottle not thoroughly flushed with plume fluids before triggering, and/or 2) particles are lost during the filtration process. We consider the former two causes unlikely since the Niskin bottle had been clearly submerged in plume fluids for approximately 10 sec before each sample was taken. The vertical flow rate of the North Tower plume at 1 m above the source vents estimated from COVIS Doppler-mode data is approximately 0.2 m/s (Figure C.1a). Therefore, 10 sec should be enough to flush the Niskin bottle which is approximately 0.8 m tall. As for the third cause, since only 1 L out of the 2.5 L plume fluid in a Niskin bottle was filtered, it is possible that some large particles that had settled down to the bottom of the bottle were missed despite the effort to resuspend the particles in the bottle before extracting fluid from it (see discussion in the preceding paragraph). However, we consider this third cause unlikely because the samples taken in 2013 (see Spreadsheet A in the electronic supplementary materials) at similar levels of the North Tower plume, of which most of the fluid in a Niskin bottle was filtered, give similar results. Therefore, the substantial difference between the current measurements and those of Mottl and McConachy (1990) likely reflect the disparate particle concentrations in the two different plumes.

In order to estimate the particle size distribution, we took microscopic photos of the particle-laden Anodisc filters using a field emission scanning electron microscope (FESEM). We cut a sliver of each filter and attached it to an aluminum specimen mount using carbon tape. We then coated the sample with 20 nm gold for FESEM analysis. Figure 2.4 shows an example of the FESEM photos of the particles on the filters. In this photo, the majority of particles have radii $\ll 1\,\mu$m, and aggregate to form a layer of 'mud cake' that covers almost the entire filter (Figure 2.4b). Larger particles ($> 1\,\mu$m) are found on top of this 'mud cake' layer with far smaller quantities. The particles composing the 'mud cake' appear to have radii smaller than $0.05\,\mu$m. Their prevalence in our plume samples is consistent with the notion that nanoparticles (i.e. particles with one or more dimensions less than 0.1 μm in size) are a widespread component of high-temperature hydrothermal discharges (Gartman et al., 2014).

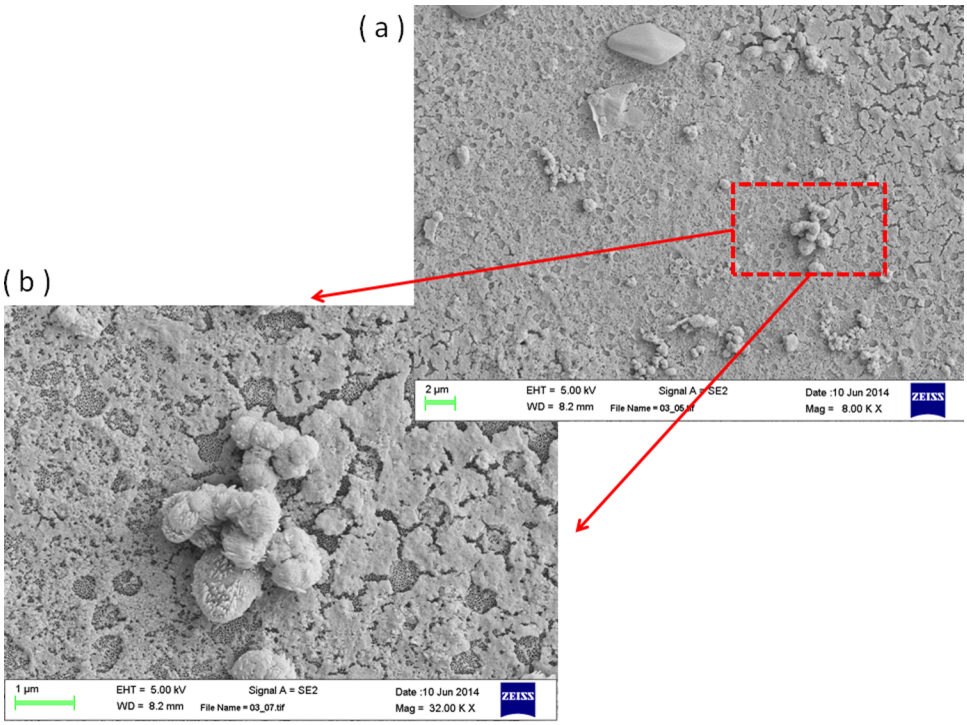

Figure 2.4: FSEM photos of the suspended particles within the major buoyant plume above the Grotto mound obtained by filtering the water sample collected in the first Niskin bottle. (a) large particles (grain size $> 1\,\mu m$) underlaid by the aggregate of small particles (grain size $\ll 1\,\mu m$) covering almost the entire filter surface. (b) a close up of the aggregate of small particles.

In practice, we measure the radii (i.e. radii of circles having equivalent surface area as the particles) and count the numbers of individual particles and particle aggregates that can be clearly distinguished in the FESEM photos, which in general have radii greater than $0.2\,\mu$m. We neglect the particles composing the 'mud cake' because their dense aggregation makes it impossible to distinguish them from one another. In this way, we obtain a discrete size distribution of particles having radii between 0.2 and 18 μm (the largest observed particle radius) in 0.1 μm intervals (see Figure A.2 and the discussion in Appendix A for more details). For particles having radii smaller than 0.2 and larger than 0.01 μm (the hypothesized smallest particle radius), we fit a log-normal distribution curve having the following mathematical expression to the discrete size distribution obtained above

$$n(a) = \frac{\Lambda}{a} \exp\left(-\frac{[\log(a) - \Upsilon]^2}{\Sigma^2}\right) \tag{2.2}$$

where n is particle count, a is particle radius, and Λ, Υ, Σ are adjustable constants. The choice of the log-normal distribution is based on its similarity to the overall shape of the discrete particle size distribution shown in Figure A.2.

For particles having radii greater than $18\,\mu$m, we assume the particle count decreases with the radius exponentially as

$$n(a) = n_{18} \exp\left(-[a - 18\,\mu\text{m}]^2/b^2\right) \tag{2.3}$$

where n_{18} is the number of particles having radii of $18\,\mu$m, and b is the e-folding radius of the exponential decrease which is arbitrarily set to $2\,\mu$m. In this way, we obtain a discrete particle size distribution over the size range $0.01 \leq a \leq 500\,\mu$m (the maximum particle size reported in Feely et al. (1987) based on the samples taken from several vents on the Endeavour Segment) in $0.1\,\mu$m intervals. We then calculate the probability density function (PDF) of particle size distribution as

$$P(a) = \frac{n(a)}{N\Delta a} \tag{2.4}$$

where $P(a)$ is the PDF so that $P(a)\Delta a$ is the probability of a plume particle having a radius between a and $a + \Delta a$, N is the total number of particles over the whole size range, and $\Delta a = 0.1\,\mu$m. Figure 2.5 shows the resulting PDF over the size range $0.01 \leq a \leq 20\,\mu$m.

Note that the PDF obtained this way is biased towards large particles because the small particles composing the 'mud cake' have been neglected. It should also be noted the mass concentrations in equation (2.1) were obtained based on the mass of all the particles on a given filter including the 'mud cake' particles. Table 2.1 defines mathematical symbols used and gives values of constant parameters in this chapter.

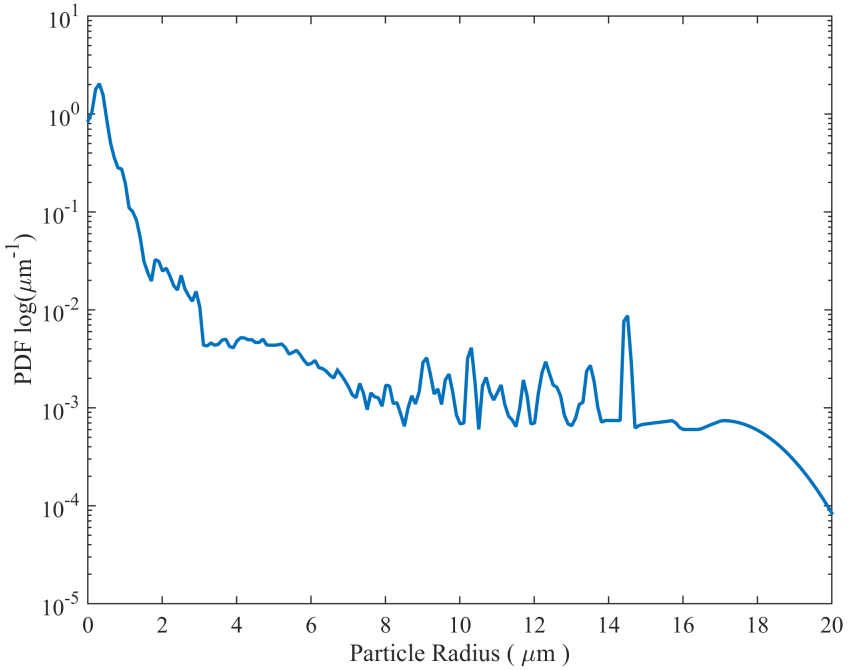

Figure 2.5: Probability density function (PDF) of particle size distribution over the size range $0.01 \leq a \leq 20\,\mu$m.

2.3 Theoretical Estimations of Acoustic Backscatter

As discussed in Section 2.1, suspended particles and temperature fluctuations are two major sound scatterers within a hydrothermal plume. The acoustic backscatter from the particles has two components: 1) backscatter from individual particles, and 2) backscatter from the microstructure on the scales of the acoustic wavelength in the spatial distribution of particles. These two components along with temperature fluctuations are thus three possible sources of backscatter from a hydrothermal plume. The following three subsections give the

Table 2.1: Symbols and Values of Parameters

Symbol	Description	Values and Units
A_s	backward scattering amplitude of a particle	m
a	particle grain size	m
a_0	mean particle grain size	m
a_T	fractional change in sound speed due to temperature change	$2.5 \times 10^{-3}\,^{\circ}\mathrm{C}^{-1}$
b	plume radius	m
C	fundamental constant in the 3-D spatial spectrum	1.542
c	sound speed	1500 m/s
e	ratio of particle bulk modulus to seawater bulk modulus	40
f_0	central frequency of COVIS	400 kHz
h	ratio of particle density to seawater density	4
k_0	sonar wavenumber of COVIS	1.7×10^3 rad/m
k_T	molecular thermal diffusivity	$1.5 \times 10^{-7}\,\mathrm{m}^2/\mathrm{s}$
K_L	wavenumber corresponding to the largest eddies within the plume	6.3 rad/m
M	particle mass concentration	$\mathrm{kg/m}^3$
$n(a)$	probability density function (PDF) of the particle size distribution	m^{-1}
$n_g(a)$	PDF of the Gaussian distribution	m^{-1}
$n_l(a)$	PDF of the log-normal distribution	m^{-1}
q	straining constant	3.7
W	plume centerline vertical flow rate	m/s
z	height above the source vents	m
α	entrainment coefficient	
α_T	thermal expansion coefficient	$1.3 \times 10^{-4}\,^{\circ}\mathrm{C}^{-1}$
$\overline{\beta}$	fractional volume of the plume occupied by particles	
$\overline{\beta'^2}$	variance of β	
ϵ	turbulent kinetic energy dissipation rate	W/kg
$\overline{\chi_\xi}$	acoustic impedance variance dissipation rate	s^{-1}
$\overline{T'^2}$	variance of plume temperature	$^{\circ}$C
σ	particle grain size standard deviation	m
ρ	density of plume fluid	$1000\ \mathrm{kg/m}^3$
ρ_w	density of seawater	$1028\ \mathrm{kg/m}^3$
ρ_s	particle density	$4000\ \mathrm{kg/m}^3$
s_v	volume backscattering coefficient	m^{-1}
s_{vp}	contribution of individual particles to s_v	
s_{vm}	contribution of particle microstructure to s_{vm}	
s_{vT}	contribution of temperature fluctuations to s_v	
ξ	normalized acoustic impedance fluctuations	
σ_ξ	standard deviation of ξ	
μ	dynamic viscosity of plume fluid	$10^{-3}\,\mathrm{Pa \cdot s}$
ν	kinematic viscosity of plume fluid	$10^{-6}\,\mathrm{m}^2/\mathrm{s}$

formulas used for estimating the backscatter from those three sources respectively.

2.3.1 Individual Particles

Mathematical formulas used to quantify the combined backscatter from individual particles have been developed and applied in many previous studies (e.g., Sheng and Hay, 1988; Thorne et al., 1993; Thorne and Meral, 2008; Xu and Di Iorio, 2011). Applying the single scattering approximation and the Rayleigh scattering theory gives the combined backscatter from individual particles as

$$s_{vp} =< |A_s(a)|^2 > \left(\frac{3M}{4\pi\rho_s < a^3 >} \right). \tag{2.5}$$

The derivation of equation (2.5) and justifications of the underlying assumptions are given in Appendix B. Within equation (2.5), s_v is the volume backscattering coefficient in units m^{-1} (i.e., backscattering cross-section per unit solid angle per unit volume), which is a measure of the strength of a scatterer, and the subscript p refers to individual particles; $|A_s(a)|^2$ is the squared backward scattering amplitude of a particle, which is proportional to the sixth power of particle radius (a) in the Rayleigh scattering regime (equation (B.4)) (Palmer, 1996), M is the particle mass concentration in units kg/m^3, and ρ_s is the mass density of a single particle. The angular bracket '<>' represents an average over the particle size distribution

$$< |A_s(a)|^2 >= \int_0^\infty |A_s(a)|^2 P(a) da, \tag{2.6}$$

$$< a^3 >= \int_0^\infty a^3 P(a) da, \tag{2.7}$$

where $P(a)$ is the PDF of particle size distribution.

2.3.2 Microstructure within Particle Suspension

The microstructure in the spatial distribution of particles exists due to the turbulence within the plume. Flows are generally considered as fully turbulent if the Reynolds number (R_e) satisfies $R_e > 10^4$. The Reynolds number of a buoyant plume can be calculated as

$$R_e = \frac{Wb\rho}{\mu} \tag{2.8}$$

where W is the plume's vertical flow rate, b is the plume's radius, ρ is the density of plume fluid, and μ is the dynamic viscosity of the plume fluid. Processing COVIS Doppler-mode data gives $0.15 \leq W \leq 0.25$ m/s and $1 \leq b \leq 3$ m over the initial 10-m rise of the North Tower plume (Figure C.1a,d). Substituting these along with $\rho = 1000\,\mathrm{kg/m^3}$ and $\mu = 10^{-3}\,\mathrm{Pa \cdot s}$ gives $2.5 \times 10^5 \leq R_e \leq 4.5 \times 10^5$. Thus the North Tower plume can be regarded as fully turbulent. The turbulent microstructure of plume particles leads to fluctuations of the acoustic impedance, which in turn scatters sound waves. The resulting volume backscatter coefficient is

$$s_{vm} = \frac{q\nu^{1/2}\overline{\beta'^2}H\kappa_L^{2/3}k_0}{24\epsilon^{1/6}C}\exp(-qK^2/\kappa_{B\xi}^2) \tag{2.9}$$

with

$$H = \frac{1}{4}\left[\frac{3(1-h)}{1+2h} - \frac{1}{e} + 1\right]^2.$$

The derivation of equation (2.9) is given in Appendix C. Within equation (2.9), the subscript m refers to microstructure in particle spatial distribution; $\beta = M/\rho_s$ is the fractional volume of the plume occupied by particles, and $\overline{\beta'^2}$ is its variance; H is a factor dependent on the elastic properties of particles including $e = K_s/K_w$, the ratio of particle bulk modulus (K_s) to seawater bulk modulus (K_w), and $h = \rho_s/\rho_w$, the ratio of particle density (ρ_s) to seawater density (ρ_w); $\kappa_L = 2\pi/L$ is the wavenumber corresponding to the outer scale of the inertial-convective subrange, in which $L = 2b_e$ and b_e is the plume's e-folding radius obtained by processing the Doppler-mode data recorded by COVIS following the procedures described in Section 3.1 (Figure C.1d); $k_0 = 2\pi f_0/c$ is the wavenumber associated with the acoustic signals used in the Imaging and Doppler modes of COVIS where $f_0 = 396000$ Hz is the sonar frequency and $c = 1500$ m/s is the sound speed; ϵ is the turbulent kinetic energy dissipation rate (Figure C.1d, see Appendix C for the estimation of ϵ); $K = 2k_0$ is the Bragg wavenumber; $\kappa_{B\xi} = (\epsilon/(\nu k_T^2))^{1/4}$ is the Batchelor wavenumber associated with acoustic impedance where ν is the kinematic viscosity and k_T is the molecular thermal diffusivity; C is a fundamental constant determined by Ross (2003) to be 1.542; $q = 3.7$ is the straining constant (Oakey, 1982).

2.3.3 Temperature Fluctuations

The same turbulence responsible for the presence of microstructure in particle spatial distribution also causes fluctuations in the temperature, salinity, and velocity fields within the plume. These fluctuations lead to variations of acoustic impedance, which in turn scatter sound waves. According to Di Iorio et al. (2005), the sound-scattering effect of salinity variations in a hydrothermal plume is small compared to that of temperature variations. Additionally, turbulent velocity has zero effect on backward scattering (Ross, 2003). Therefore, we neglect the effects of salinity and velocity fluctuations on backscatter in this study. The volume scattering coefficient of the turbulence-induced temperature fluctuations is

$$s_{vT} = \frac{q\nu^{1/2}\overline{T'^2}(a_T - \alpha_T)^2\kappa_L^{2/3}k_0}{96\epsilon^{1/6}C}\exp(-qK^2/\kappa_{B\xi}^2) \tag{2.10}$$

The derivation of equation (2.10) is given in Appendix C.2. Within equation (2.10), the subscript T refers to temperature fluctuations, $\overline{T'^2}$ is the variance of temperature fluctuations, a_T is the fractional change in sound speed due to temperature change, and α_T is the thermal expansion coefficient. To compare the estimated backscatter with observation, we convert the volume backscattering coefficient to volume backscattering strength $S_v = 10\log_{10}(s_v/m^{-1})$ in units dB. The following section discusses the results.

2.4 Results and Discussion

2.4.1 Estimated vs Observed Acoustic Backscatter

To estimate the combined acoustic backscatter from individual particles, we substitute M and the probability density function (PDF) of particle size distribution estimated from the samples taken from the North Tower plume (Section 2.2.2) into equations (2.5) to (2.7) and solve the integral numerically (the upper limit of the integral is set to be 500 μm). The resulting volume backscattering strength is $S_v = -85$ dB for $M = 2.6$ mg/L and $S_v = -82$ dB for $M = 5.6$ mg/L. In order to quantify the error in those estimates that is caused by the uncertainty in the particle size distribution applied, we conduct Monte-Carlo simulations based on the following procedures. First, we randomly pick 30 out of the 51 views (i.e. a 'view' refers to the area within a microscopic photo of a particle-laden filter taken with 500X

magnification, see Appendix A) used to calculate the PDF shown in Figure 2.5. Second, we use those 30 views to calculate a new PDF and substitute it along with $M = 5.6$ mg/L into equation (2.5) to calculate the volume scattering coefficient (s_v). Lastly, we repeat the previous two steps 5000 times and calculate the standard deviation of the resulting s_v estimates. The result, which is approximately 10% of the mean value, corresponds to a 0.4 dB error in S_v. In addition, we assume the standard deviation of M equals 50% of the mean, which leads to a 1.8 dB error in S_v. As a result, the combined uncertainty in particle size distribution and mass concentration leads to an error in S_v of $0.4 + 1.8 = 2.2$ dB. It should be noted that the oxidative dissolution and precipitation of particles in the Niskin bottles during the time period between sample collection and recovery (several hours) and during the filtration process (a couple of hours) introduce inherent uncertainty in the estimated particle size distribution and mass concentration, which subsequently leads to additional error in S_v. This error is neglected based on the assumption that the effect of oxidative dissolution and precipitation on particle mass concentration and size distribution is insignificant. In addition, S_v is likely biased towards an overestimate because the particle size distribution used in the calculation is biased towards large particles (Section 2.2.2) and the combined backscatter from individual particles is proportional to the third power of particle radius (equations (B.4) and (2.5)).

To investigate the sensitivity of acoustic backscatter to particle size and distribution shape, we use hypothetical size distributions instead of the measured one to estimate the combined backscatter from individual particles. The Gaussian and log-normal distributions are two common particle distributions observed in marine environments (Horn and Walton, 2007; Jonasz, 1983). The corresponding PDFs of the two distributions are

$$\begin{aligned} P_g(a) &= \frac{1}{\sigma\sqrt{2\pi}} \exp\left[-(a-a_0)^2/2\sigma^2\right], \\ P_l(a) &= \frac{1}{a\sqrt{2\pi}\gamma} \exp\left[-(\ln(a)-m_0)^2/2\gamma^2\right]. \end{aligned} \tag{2.11}$$

Within equation (2.11), P_g and P_l are the PDFs of the Gaussian and log-normal distributions respectively; $a_0 = \int_0^\infty an(a)da$ is the mean particle radius; $\sigma = \left(\int_0^\infty (a-a_0)^2 n(a)da\right)^{1/2}$ is the standard deviation of particle radius; $\gamma = \sqrt{\ln[(\sigma/a_0)^2+1]}$, and $m_0 = \ln\left(a_0^2/\sqrt{a_0^2+\sigma^2}\right)$.

Substituting those hypothetical size distributions with varying a_0 and $\sigma = a_0$ into equation (2.5) yields the predicted volume backscattering strength (S_v) as a function of a_0, which is shown in Figure 2.6. The particle mass concentration used in the calculation is $M = 6$ mg/L. Table 2.1 lists the values of the other constant parameters involved in the calculations.

Figure 2.6 suggests acoustic backscatter is sensitive not only to the mean of but also to the shape of a particle size distribution. Note that the S_v estimates for the log-normal distribution exceed those for the Gaussian distribution by approximately two orders of magnitude. Such a difference is due to the slower falloff of the PDF of the log-normal distribution relative to the Gaussian distribution towards large particles. Equations (B.4) and (2.5) show that the combined backscatter from individual particles is proportional to the 3rd power of particle radius and is thus heavily weighted in favor of large particles.

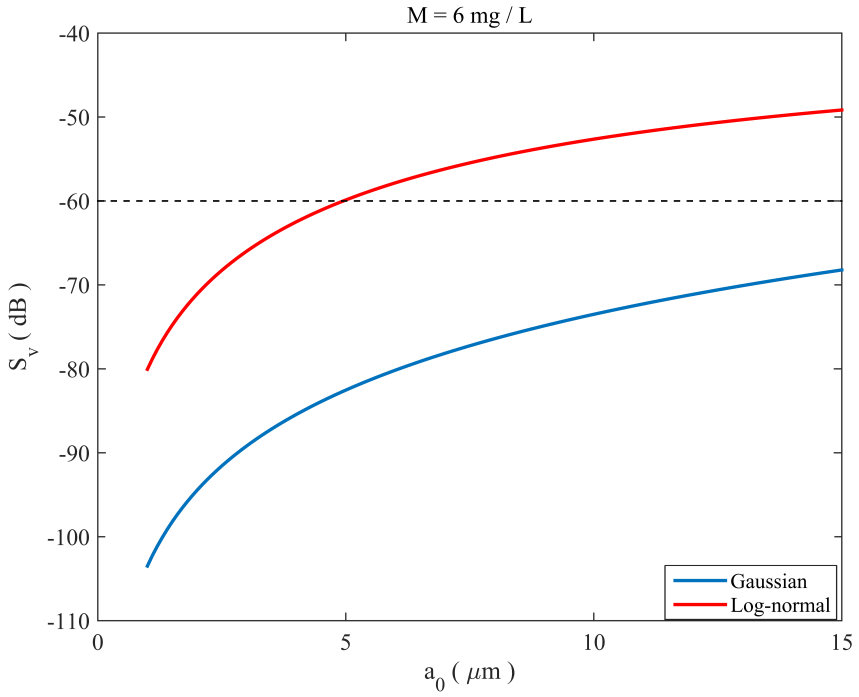

Figure 2.6: Predicted volume backscattering strength (S_v) of a particulate suspension with mass concentration $M = 6$ mg/L and the Gaussian (blue) or log-normal size distribution having mean grain size $1 \leq a_0 \leq 15\,\mu$m and standard deviation $\sigma = a_0$. The black dashed lines mark COVIS measurement of S_v close to the center of plume (Figure 2.7).

We estimate the backscatter from the microstructure in particle spatial distribution using equation (2.9). Assuming $\sqrt{\overline{\beta'^2}}$ equals one-forth of the mean value of β and applying the values of constant parameters listed in Table 2.1 gives $S_v = -173$ dB for $M = 6$ mg/L and $S_v = -123$ dB for $M = 2000$ mg/L. Note that these estimates are much smaller than the estimate of the combined backscatter from individual particles (~ -80 dB). This suggests the backscatter from the microstructure in particle spatial distribution is negligible compared with the combined backscatter from individual particles.

Figure 2.7 shows the backscatter measured by COVIS over a horizontal cross-section of the North Tower plume at approximately 1 m above the source vents, which is approximately the same level where the plume samples were taken. The corresponding acoustic dataset was recorded no more than 3 hours before the collection of plume samples. Figure 2.7 shows $S_v > -60$ dB close to the center of the plume, which is more than two orders of magnitude higher than the estimated backscatter from particles (~ -80 dB). Equation (2.5) suggests the combined backscatter from individual particles is proportional to their mass concentration $s_v \sim M$. Therefore, in order for the backscatter from particles to reach the observed level, one needs a particle mass concentration that is two orders of magnitude higher than the measurement: $M \sim 600$ mg/L with the estimated particle size distribution shown in Figure 2.5. Furthermore, Figure 2.6 shows, with $M = 6$ mg/L, the particles must have $a_0 \sim 5\,\mu$m to account for the backscatter observed close to the center of the plume for the log-normal distribution, while a far larger a_0 is needed for the Gaussian distribution.

For the acoustic backscatter at heights beyond 1 m above the source vents, the 3-D acoustic backscatter data recorded by COVIS suggests a general decrease with height (Figure 2.8). Within Figure 2.8, the blue curve shows the variation of the estimated S_v at the centerline of the North Tower plume as a function of the height above the source vents (z). As described in Xu et al. (2013), we estimate the centerline value of S_v at a given height by fitting a 2-D Gaussian curve to the measured horizontal cross-section of S_v at that height and taking the peak value of the Gaussian curve (red curve in Figure 2.8). The green curve in Figure 2.8 shows the estimated S_v at the plume boundary, which is defined as $1/\exp(2) \approx 14\%$ of the corresponding centerline estimate. The general decrease in backscatter with height shown in Figure 2.8 is expected because both the temperature

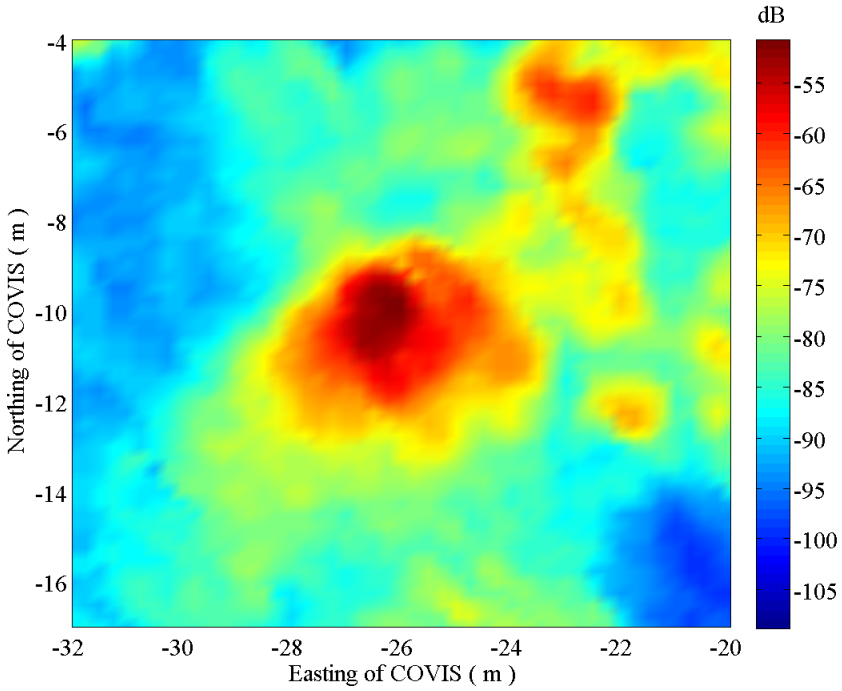

Figure 2.7: Volume backscattering strength (S_v) measured by COVIS over the horizontal cross-section of the North Tower plume at 1 m above the source vents. The acoustic measurement, conducted on May 20th, 2014 at 15 hours UTC, preceded the collection of plume particle samples by 2 hours.

fluctuations and particle concentration reduce as the plume gets increasingly diluted during its buoyant rise by mixing with ambient seawater.

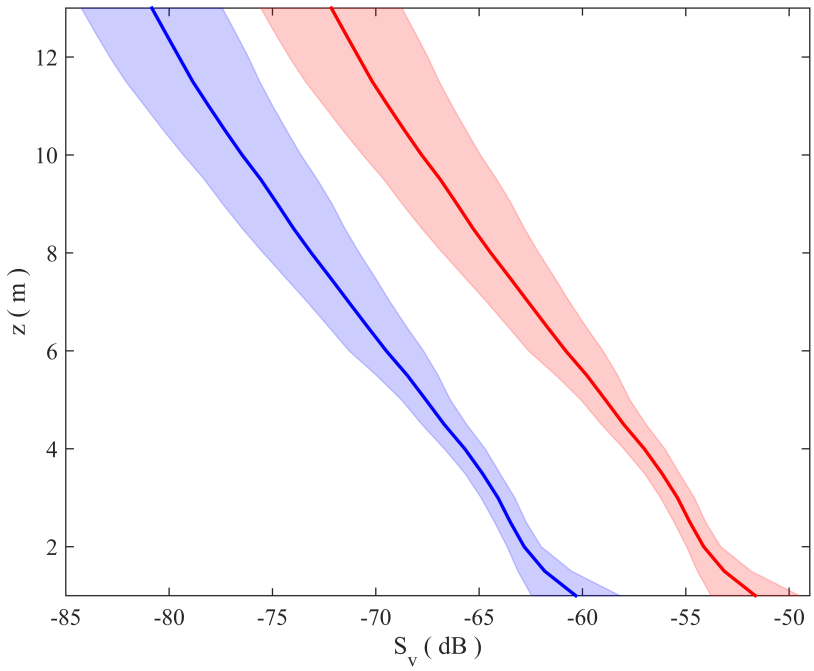

Figure 2.8: Volume backscattering strength (S_v) at the centerline (red) and boundary (blue) of the North Tower plume as a function of height above the source vents (z) obtained from the 3-D acoustic backscatter datasets recorded by COVIS in May 2014. The solid curves denote the monthly means, and the edges of the shaded areas are at one standard deviation away from the means.

Estimating the contribution of particles to the acoustic backscatter observed at levels higher than 1 m above the source vents requires knowledge of the particle mass concentration (M) and size distributions at those levels. In Appendix D, we develop a formula for estimating the variation of M with height for particles having a given radius. The formula is based on the classic particle sedimentation theory described in Bursik et al. (1992); Ernst et al. (1996); Bemis et al. (2006), which uses the plume flow rate and radius estimated by processing COVIS Doppler-mode data along with a given initial value of M at $z = 1$ m as the input data. The results shown in Figure 2.9 exhibit a general decrease in M with height, and the slope of the decrease increases with increasing particle grain size. The decrease of M with height is due to both the dilution of the plume as it mixes with ambient seawater

and the fallout of particles through the plume's lateral and bottom boundaries. The fallout of particles accelerates with increasing particle size and so does the decrease in M with height. In the absence of particle fallout, the decrease of M with hight is a sole result of plume dilution and is thus independent of particle size. In this case, all the curves in Figure 2.9 would overlap. Note that the 50 μm and 170 μm curves in the figure almost overlap. This suggests the vertical flows within the plume are strong enough to carry particles up to 170 μm through the initial 12 m rise. Since the vast majority of the particles observed in the samples collected from the North Tower plume are well below 170 μm, it is sensible to assume the particle fallout is negligible and the predicted variation of M with height to follow the 50 μm curve in Figure 2.9. Similarly, it is reasonable to assume particle size distribution to be invariant through the initial 12 m plume rise.

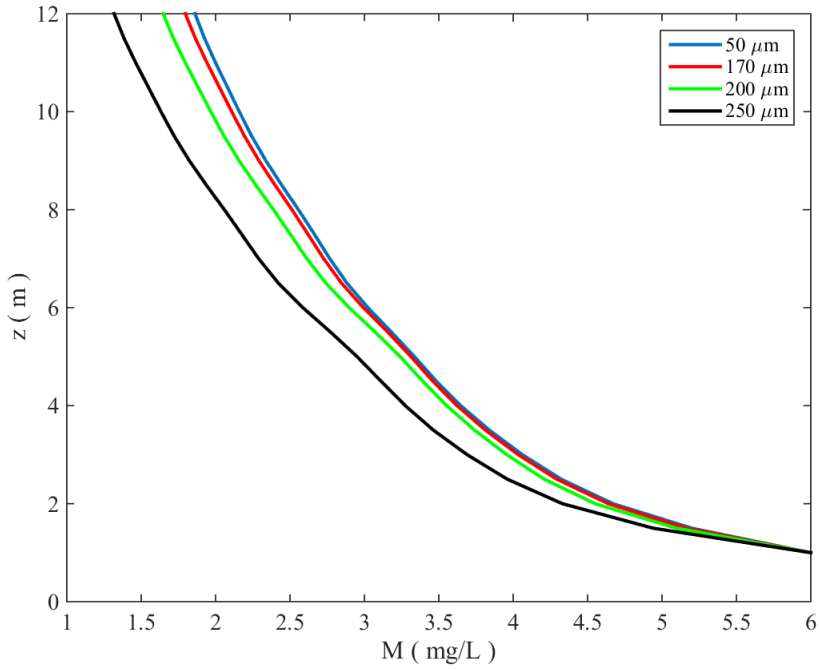

Figure 2.9: Predicted variation of particle mass concentration (M) as a function of height above the source vents (z) estimated using the formulas described in Appendix D for particles having grain size from 50 to 250 μm. The plume vertical flow rate and radius used to constrain the formulas are averaged over the COVIS Doppler data recorded from 2012 to 2014. The initial value of M at $z = 1$ m is 6 mg/L.

Substituting the predicted particle mass concentration (M) obtained above and the probability density function (PDF) of particle size distribution estimated from plume particle samples (Figure 2.5) into equation (2.5) gives the estimated variations of volume backscattering strength (S_v) with height in Figure 2.10. As discussed at the beginning of this section and Section 2.2.2, S_v is likely overestimated because the particle size distribution used in the calculation is biased towards large particles. The result shown in Figure 2.10 suggests the estimated particle-generated backscatter is ubiquitously lower than the measurements. The backscatter from particles is approximately 1% of the measurement at the plume boundary at $z = 1$ m and this percentage increases to 30% at $z = 12$ m. This result suggests the relative importance of plume particles to acoustic backscatter increases with height, which is apparent in Figure 2.10 as the estimated backscatter from particles decreases with height more slowly than the measurements. This result implies the contribution of particles to acoustic backscatter could be significant at higher levels of the plume ($z \gg 10$ m).

2.4.2 Estimation of Temperature Variability from Acoustic Backscatter

The discussion in the preceding section suggests the contribution of particles to the acoustic backscatter recorded by COVIS from the initial tens-of-meter rise of the North Tower plume is negligible. This on the other hand suggests the temperature fluctuations are the dominant scattering mechanism causing the backscatter signals received by COVIS. As a result, it is sensible to assume temperature fluctuations to be the only backscattering mechanism. Under this assumption, one can invert the acoustic backscatter to obtain estimates of the temperature fluctuations within the plume using equation (2.10). In practice, we substitute the observed centerline volume backscattering strength (S_v) shown in Figure 2.8 along with the values of ϵ and b_e (used to calculated κ_L) shown in Figure C.1(c)(d) into equation (2.10) to estimate the corresponding centerline temperature standard deviation ($\sqrt{\overline{T'^2}}$). The values of the constant parameters used in the calculation are given in Table 2.1.

Figure 2.11 shows the acoustically estimated $\sqrt{\overline{T'^2}}$ and its comparison with the $\sqrt{\overline{T'^2}}$ estimated from the in-situ temperature measurements made within the North Tower plume. We made the temperature measurements using a conductivity-temperature-depth instrument (CTD) mounted on the ROV ROPOS. We conducted a total of 6 CTD profiles during

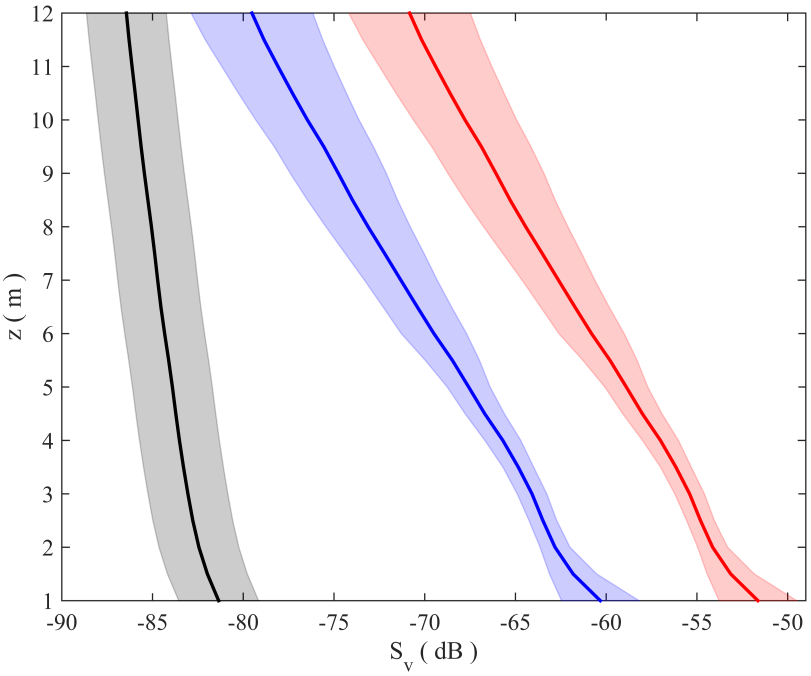

Figure 2.10: The black curve is the estimated volume backscattering strength (S_v) from plume particles as a function of the height above the source vents (z). The particle size distribution used in the estimation is obtained from the particle samples taken at 1 m above the source vents (Figure 2.5), which is assumed to be invariant with height. The particle mass concentration used in the estimation follows the 50 μm curve in Figure 2.9. The black shaded area marks the 2.2 dB error in S_v as discussed at the beginning of this section. The red and blue curves and shaded areas denote the means and standard deviations of the COVIS measurements of S_v at the plume centerline and boundary respectively over the month of May in 2014.

the same ROV dive where the plume particle samples were collected. During each profile, the ROV first entered the plume at approximately 1 m above the source vents. The ROV adjusted its position within the plume until the real-time temperature reading from the CTD reached a maximum–an indicator that the CTD is at or close to the plume centerline. The ROV then slowly ascended to 15 m above the vents and then descended back to the starting level in the same manner. We grouped the temperature samples in the 6 profiles into 0.5-m vertical bins and calculated the standard deviation of each bin. The comparison exhibits a reasonable match with the CTD measurements having a slightly steeper decrease with height than the acoustic estimates. The reasonable fit in Figure 2.11 corroborates the idea that turbulence-induced temperature fluctuations are the dominant mechanism causing the acoustic backscatter from the initial 10-m rise of the North Tower plume. It also demonstrates the potential of using acoustic backscatter as a remote sensing tool to measure the temperature fluctuations within a hydrothermal plume.

2.5 Chapter Summary

In this chapter, we investigate the relative importance of particles and temperature fluctuations as backscattering mechanisms within a hydrothermal plume based on in-situ plume particle samples and near-contemporaneous acoustic backscatter measurements made by an imaging sonar. We estimate the size distribution and mass concentration of plume particles by analyzing the in-situ particle samples. The estimated size distribution suggests the number of particles with radii much smaller than 1 μm far exceeds the number of larger particles. The theoretically estimated backscatter from plume particles based on their estimated size distribution and mass concentration is approximately two orders of magnitudes smaller than the observed backscatter. This finding suggests turbulence-induced temperature fluctuations, rather than plume particles, are the dominant backscattering mechanism during the initial ten-meter rise of the plume. However, the relative contribution of plume particles to acoustic backscatter increases with height and can possibly be significant at higher levels of the plume. We invert the measured acoustic backscatter to obtain estimates of the temperature standard deviations within the plume, which exhibit a reasonable match with CTD measurements. This finding corroborates the idea that temperature fluctuations

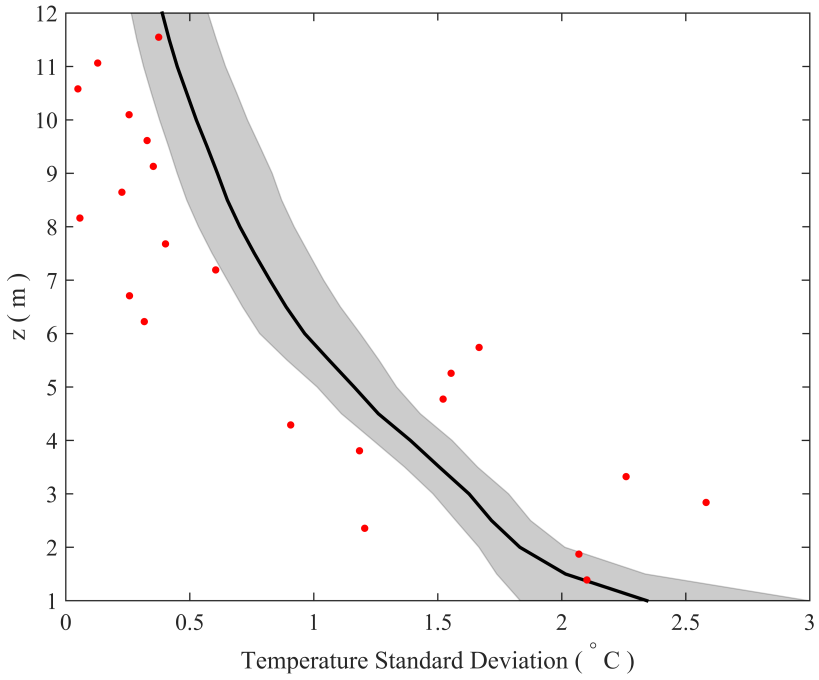

Figure 2.11: The black curve is the temperature standard deviation ($\sqrt{\overline{\overline{T'^2}}}$) estimated from the observed acoustic backscatter along the centerline of the North Tower plume (Figure 2.8) as a function of the height above the source vents (z). The gray shade marks the uncertainty in the estimated $\sqrt{\overline{\overline{T'^2}}}$ caused by the uncertainty in the observed backscatter. The red dots denote the $\sqrt{\overline{\overline{T'^2}}}$ estimated from the CTD data recorded on the same ROV dive on which the plume particle samples were taken.

are the dominant backscattering mechanism and demonstrates the potential of using acoustic backscatter as a remote-sensing tool to measure the temperature variability within a hydrothermal plume.

Chapter 3

Time-series Measurements of the Dynamics of a Deep-sea Hydrothermal Plume: 2010 Data

This chapter aims to investigate the temporal variations of the dynamics of a buoyant hydrothermal plume and its interactions with the hydrodynamical processes in the ambient water column. The key observational data presented in this chapter is the 26-day time-series of the volume transport, vertical flow rate, and expansion rate of the North Tower plume above Grotto obtained by processing the Doppler-mode data recorded by COVIS in October 2010 (Section 1.4, Ocean Networks Canada Data Archive (2011)). The temporal variations observed in the time series reveal significant influences of ocean currents on the mixing of the plume with the ambient seawater, which serves as the linkage between the dynamics of a hydrothermal plume with the oceanic processes in the water column and the atmospheric forcing on the sea surface. This chapter is adapted from Xu et al. (2013). Section 3.1 introduces the methodology along with its underlying assumptions and uncertainty. Section 3.3 discusses the temporal variability observed in the 26-day time series and its implications on the influences of tidal and atmospheric forcing on the dynamics of the plume. Section 3.4 gives concluding remarks.

3.1 Methods

3.1.1 Plume vertical velocity estimation

We estimate the plume velocity component along the acoustic line-of-sight V_r from the Doppler frequency shift observed in the backscatter signals recorded in Doppler mode using the covariance method described in Jackson et al. (2003) (Appendix F). Similar to the Imaging-mode data (Section 1.4), we interpolate the volume backscattering coefficient

s_v (i.e., backscattering cross-section per unit solid angle per unit volume) and V_r of the backscatter received through the 'fans' at successive 1° steps within a sweep onto a uniform 3-D rectangular grid with $35 \times 30 \times 50$ m points and 0.5 m intervals in all three coordinates.

In order to estimate the plume vertical volume transport, the plume velocity component along the acoustic line-of-sight V_r is converted to the plume vertical velocity component W using the geometric technique developed by Jackson et al. (2003), which is summarized in the following two subsections.

Plume centerline location

According to the 'dominant eddy' concept (Chu, 1994), a plume's centerline can be defined as an axis or streamline that describes the direction of the coherent motion within the plume. Applying the method developed by Rona et al. (2002), we construct the centerline of the plume by connecting the local maxima on successive horizontal cross-sections of the 3-D-gridded volume backscattering coefficient s_v. Instead of searching for the absolute maxima, the locations of which are unstable due to the turbulence within the plume, we locate the local maxima by fitting a 2-D Gaussian curve to each cross-section and pinpointing the peak of the Gaussian fit. The choice of a Gaussian function is motivated by both its ease of use and its traditional application to describing the distribution of plume properties (i.e. flow velocity, temperature, turbulent intensity) about the centerline of the plume (Papanicolaou and List, 1988). The mathematical expression of the 2-D Gaussian curve is

$$s_v(r) = s_{vc} \exp\left(-\frac{r^2}{b_{sv}^2}\right) + s_{va} \tag{3.1}$$

$$r = \sqrt{(x - x_0)^2 + (y - y_0)^2} \tag{3.2}$$

where s_{vc} is the peak value of the profile given zero background ($s_{va} = 0$), r is the radial distance from the centerline, $[x_0, y_0]$ are the coordinates of the Gaussian peak, b_{sv} is the e-folding radius of the Gaussian profile (the distance from the peak to the point where the s_v decreases to $1/e$ (37%) of its peak value). Note that b_{sv} will be used as a measure of the plume radius to determine the expansion rate in Section 3.1.2. As can be seen from Figure 3.1, the above Gaussian profile gives a good fit to the data. We then construct the

plume centerline by fitting a cubic curve to the local s_v maxima on successive horizontal cross-sections (Figure 3.2).

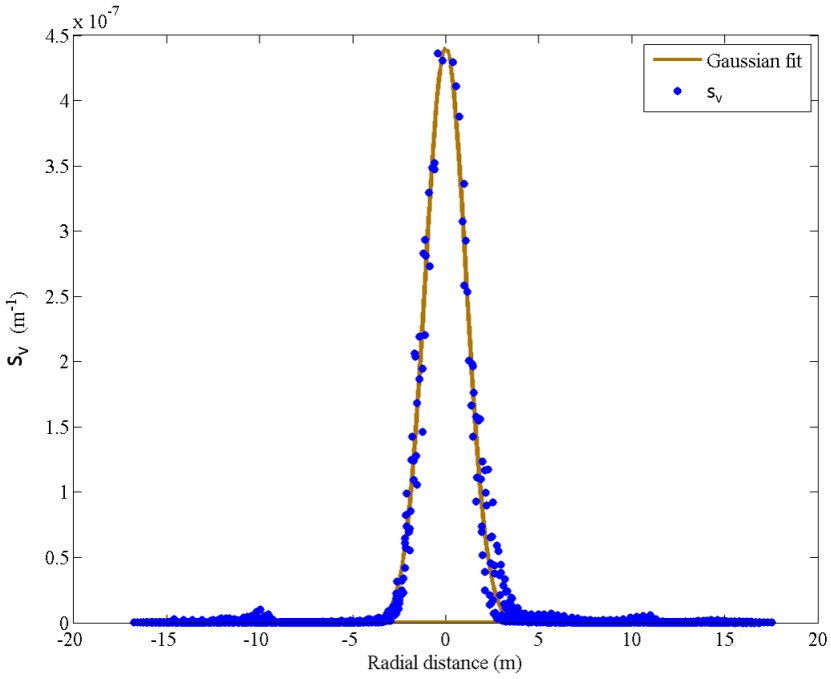

Figure 3.1: Volume backscattering coefficient s_v profile across a horizontal cross-section at 12 m above the North Tower of Grotto and the Gaussian fit. The cross-sectional profile is extracted from the 3-D gridded s_v collected on October 10, 2010. This figure is reproduced from Figure 3 in Xu et al. (2013).

Geometric conversion

We convert the plume velocity component along the acoustic line-of-sight V_r to the plume vertical velocity component W based on the centerline location obtained using the method outlined in the preceding subsection and relative angles between the acoustic line-of-sight, vertical and axial (tangential to the plume centerline) directions shown in Figure 3.3. We use symbols in bold fonts to denote vectors (i.e. velocities) and non-bold fonts for velocity magnitudes and components in this and the following sections.

The first step is to calculate the magnitude, V_c, of the plume velocity at a given point C on the plume centerline. By assumption, the plume centerline is also a streamline; therefore,

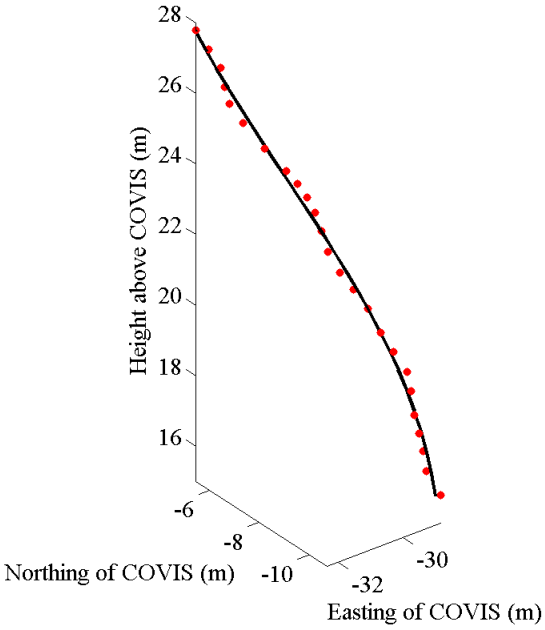

Figure 3.2: Construction of plume centerline from the 3-D gridded s_v collected on October 17th, 2010. Solid line: cubic fit; red dots: volume backscattering coefficient s_v maxima on successive horizontal cross-sections. Note that this figures shows a single instant of the plume centerline that varies with instantaneous ambient horizontal velocity structure over time. This figure is reproduced from Figure 4 in Xu et al. (2013).

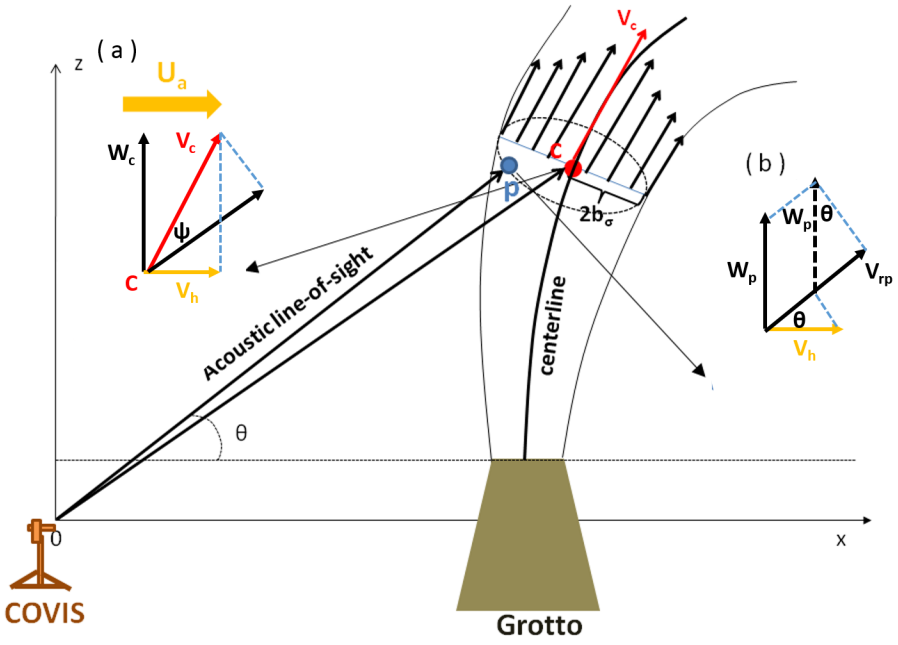

Figure 3.3: (a) Schematic diagram of the integrated plume above the North Tower of Grotto under ambient horizontal flows with plume velocities depicted on x-z plane for graphic convenience, which does not reflect the 3-D nature of the plumes behavior. C (red dot) is any given point located on the plume centerline at a certain altitude above Grotto. p (blue dot) is any given point at the same level of C within the plume. Velocity notations: $\mathbf{U_a}$ (thick yellow arrow), ambient horizontal flows; $\mathbf{V_c}$ (red arrow), plume velocity at C (note that $\mathbf{V_c}$ is in the axial direction according to the definition of plume centerline); V_{rc}, line-of-sight velocity component at C; $\mathbf{V_h}$ (yellow arrow), horizontal velocity at C; W_c, vertical velocity component at C; V_{rp}, line-of-sight velocity component at p; W_p, vertical velocity component at p. Note that the horizontal velocity at p is assumed to be the same as that at C (see text and Appendix F). (b) Geometric relationships among W_p, V_{rp} and $\mathbf{V_h}$. This figure is reproduced from Figure 5 in Xu et al. (2013).

the plume velocity at C is in the axial direction (tangential to the centerline) and thus its magnitude can be obtained using the following equation

$$V_c = \frac{V_{rc}}{\mathbf{e_c} \cdot \mathbf{e_r}} = \frac{V_{rc}}{\cos(\psi)} \tag{3.3}$$

where V_{rc} is the component of velocity along the acoustic line-of-sight at C, $\mathbf{e_c}$ is a unit vector tangent to the plume centerline, $\mathbf{e_r}$ is a unit vector pointing from the sonar to C, and ψ is the angle between $\mathbf{e_c}$ and $\mathbf{e_r}$ (Figure 3.3). Note that $\mathbf{e_c}$ and $\mathbf{e_r}$ can be readily calculated using the plume centerline and the coordinates of C in the 3-D grid. The horizontal velocity at C is thus

$$\mathbf{V_h} = (V_c \mathbf{e_c} \cdot \mathbf{e_x})\mathbf{e_x} + (V_c \mathbf{e_c} \cdot \mathbf{e_y})\mathbf{e_y} \tag{3.4}$$

where $\mathbf{e_x}$ and $\mathbf{e_y}$ are unit vectors in the x and y directions.

The horizontal flow field within the plume is a combination of ambient horizontal cross-flows ($\mathbf{U_a}$) and entrainment inflows ($\mathbf{U_e}$). We assume $\mathbf{U_a}$ does not vary in time during each sweep ($\sim$ 23 min) and only varies in the vertical direction at any given moment; that is, for a given dataset (time step), $\mathbf{U_a}$ only varies vertically and is constant along each horizontal plane. We also neglect the contribution made by $\mathbf{U_e}$ (see Section 3.1.3 for the justification of this assumption). With these assumptions, the horizontal flow field inside the plume simply equals $\mathbf{U_a}$, and thus $\mathbf{V_h}$ can be used as a proxy for the ambient horizontal flows near Grotto.

The next step is to calculate the plume velocity component in the vertical direction W_p at any given point P at the same altitude as the centerline point C using the line-of-sight velocity component V_{rp} measured at P and the horizontal velocity $\mathbf{V_h}$ obtained in the first step. The equation applied is

$$W_p = \frac{V_{rp} - \mathbf{V_h} \cdot \mathbf{e_{rp}}}{\sin(\theta)}, \tag{3.5}$$

in which the numerator eliminates the contribution of $\mathbf{V_h}$ to V_{rp}, where $\mathbf{e_{rp}}$ is the unit vector pointing from the sonar to P and θ is the angle between $\mathbf{e_{rp}}$ and the horizontal

plane. The geometric relationships among W_p, V_{rp} and $\mathbf{V_h}$ based on which equation (3.5) is derived are shown in Figure 3.3(b).

3.1.2 Estimation of plume properties

While the plume centerline vertical velocity component W_c could be obtained from equation (3.5) and substitution of the measured centerline acoustic line-of-sight velocity component V_{rc} and the calculated horizontal velocity $\mathbf{V_h}$ at the same altitude into . Nevertheless, it is preferable to obtain W_c as the peak of the 2-D Gaussian fit applying a mathematical expression equivalent to equation (3.1) to the calculated plume vertical velocity distributions on successive horizontal cross-sections of the 3-D grid. The averaging nature of the Gaussian-fitting process can help reduce the uncertainty in the W_c estimates caused by the turbulence inside the plume and the intrinsic imprecision of the Doppler velocity measurements (Jackson et al., 2003).

We estimate the plume vertical volume transport Q by integrating the plume vertical velocity component W_p calculated using equation (3.5) over successive horizontal cross-sections of the 3-D grid. In order to reduce the error in W_p estimates caused by background noise and ambient oceanic currents, we define the boundary of the plume at $2b_{sv}$ away from the centerline, where b_{sv} is the e-folding radius of the plume (equation (3.1)). We then eliminate the velocity estimates at the points where the volume backscattering coefficient s_v is smaller than its value at the boundary of the plume. According to equation (3.1), s_v at the boundary is approximately 2% of the s_v maximum. A region-growing technique is then applied to eliminate the residual velocity signals outside the plume area originating from the sporadic large s_v values outside the plume. It can be shown that this procedure leads to a systematic 2% underestimate of the volume transport. This bias is neglected in our uncertainty quantification as being insignificant in comparison to statistical error.

The expansion rate E_x (m/m) quantifies how fast a plume expands due to the entrainment of ambient seawater into the plume. Consequently, E_x is a natural measure of entrainment because a plume grows faster (with larger E_x) under greater entrainment. In practice, we reconstruct the 2-D cross-sections of the 3-D grid of the volume backscattering coefficient perpendicular to the plume centerline determined in section 3.1.1. We then fit

the 2-D Gaussian curve (equation (3.1)) to successive cross-sections to obtain the e-folding radius $b_{sv\perp}$ of the plume. Finally, we determine E_x by performing linear regression on the growth of $b_{sv\perp}$ as a function of the height above the vents,

$$b_{sv\perp} = E_x Z + A, \tag{3.6}$$

where Z is the height above the vents, and A is an adjustable constant.

3.1.3 Justification of Neglecting the Entrainment Inflows

The geometric conversion described in section 3.1.1 neglects the inhomogeneities in the horizontal flow field inside the plume caused by the entrainment inflows $\mathbf{U_e}$. Laboratory studies indicate that $|\mathbf{U_e}|$ reaches a maximum on the plume boundary and gradually decreases to zero towards the plume centerline (Chaengbamrung, 2005). Consequently, the horizontal velocity $\mathbf{V_h} = \mathbf{U_a}$ at the plume centerline and thus $\mathbf{U_e}$ has zero or negligible contribution to the plume horizontal velocity $\mathbf{V_h}$ calculated at the plume centerline.

As for the flow field about the centerline, according to the entrainment hypothesis (Morton et al., 1956), the magnitude of $\mathbf{U_e}$ at the boundary of the plume is proportional to the plume's centerline vertical velocity component W_c

$$|\mathbf{U_e}| = \alpha W_c, \tag{3.7}$$

where α is the entrainment coefficient. For a plume discharging into seawater with strong horizontal cross-flows ($|\mathbf{U_a}| \gg W_c$), the plume is bent toward the direction of $\mathbf{U_a}$, which dominates the horizontal flow field within the plume. In such a case, $\mathbf{U_e}$ can be neglected and $\mathbf{V_h} \approx \mathbf{U_a}$ everywhere inside the plume. For a plume discharging with much greater initial velocity than the ambient flow $|\mathbf{U_a}| \ll W_c$), the plume is largely vertical as it arises from the source vents. In such a case, $\mathbf{U_e}$ dominates the horizontal flow field inside the plume and thus cannot be neglected. However, we argue that neglecting $\mathbf{U_e}$ has negligible effect on the plume volume transport estimation for the following reason.

As is described in section 3.1.2, the plume vertical volume transport is calculated through integrating plume vertical velocity $\mathbf{W_p}$ over horizontal cross-sections of the plume. According to laboratory studies (Chaengbamrung, 2005), $\mathbf{U_e}$ is axisymmetric and pointing

perpendicularly towards the plume centerline when horizontal cross-flows are negligible (in the case of vertical plumes). The error in W_p induced by neglecting the contribution of $\mathbf{U_e}$ to $\mathbf{V_h}$ is also axisymmetric because of the linearity of equation (3.5), and is thus canceled out in the integration adopted to calculate the volume transport.

3.1.4 Uncertainty Quantification

The overall uncertainties in the plume vertical volume transport Q and centerline vertical velocity component W_c stem from two major error sources. First, we introduce uncertainty into Q and W_c by using an arbitrary plume boundary at $2b_{sv}$ away from the centerline to filter the velocity estimates. In order to quantify such 'arbitrariness' of the choice of the plume boundary, we allow the plume boundary to vary from $1.75b_{sv}$ to $2.25b_{sv}$ and calculate the corresponding variations in Q and W_c. Note that the range used here is broad enough to include all the reasonable choices of plume boundaries. The results indicate the uncertainty levels are 27% in Q and 6% in W_c (percent of the mean value derived by using the default threshold with plume boundary defined at $2b_{sv}$ away from the centerline, blue lines in Figure 3.7).

The second source of uncertainty is the imprecision of the Doppler measurement of line-of-sight velocity V_r, which propagates into Q and W_c through the geometric conversion and integration described in Section 3.1.1 and 5.1.2. The total imprecision in V_r estimates consists of contributions from different sources including the intrinsic error of the Doppler estimator, background noise, turbulence in the plume and ambient oceanic currents, and the bias due to finite resolution and gridding. A major, and largely unknown, source of imprecision is the turbulence in the plume. Therefore, direct quantification of the overall imprecision in V_r is not feasible, and thus we use its standard deviation V_{std} as a proxy (Appendix F and Jackson et al. (2003)). Propagating V_{std} through the calculations described in section 3.1.1 and 5.1.2 following the rules given in Taylor (1982) gives the uncertainty in Q and W_c of 4% and 24% respectively (percent of mean, Figure 3.7).

3.2 Results

Figure 3.4 summarizes the 26-day time series COVIS obtained for plume vertical volume transport Q, centerline vertical velocity component W_c, and expansion rate E_x at the North Tower of Grotto in October 2010 (Ocean Networks Canada Data Archive, 2011). The time series spans the beginning sector of the plume from $S = 5$ to 15 m, where S is the axial distance (distance away from the North Tower of Grotto, approximately 17 m above the feet of COVIS according to Figure (1.5), along the plume centerline). Here we note the key observations. Both Q and W_c show strong ($> 30\%$) short-term variations within the measurement period, but no distinct long-term trend (Figure 3.4 (a-b)). The mean vertical volume transport $< Q >$ (not shown in Figure 3.4) averaged over the axial distance $5 \leq S \leq 15$ m varies from 1.93 to 5.09 m^3/s. The mean centerline vertical velocity component $< W_c >$ (Figure 3.4(c)) averaged over the same axial distance varies from 0.11 to 0.24 m/s. The measured expansion rate E_x ($0.082 - 0.21$ m/m) correlates negatively with $< W_c >$ with a significant coefficient of determination $R^2 \sim 0.5$ and a P-value $\sim 10^{-6}$ (a P-value this small indicates it is extremely unlikely the correlation is an outcome of random noise). Note that the above ranges for $< Q >$, $< W_c >$ and E_x are the central 80% quantiles of their histograms (Figure 3.5). Table 3.1 summarizes the mean values and standard deviations of Q and W_c at $S = 5$, 10, and 15 m.

Table 3.1: Mean Values and Standard Deviations (Std) of Q and W_c

S (m)	S = 5 m	S = 10 m	S = 15 m
Mean Q (m^3/s)	1.88	3.50	5.83
Std Q (m^3/s)	0.95	1.46	2.85
Mean W_c (m/s)	0.21	0.18	0.16
Std W_c (m/s)	0.06	0.06	0.07
Std/Mean W_c (observation)	28.6%	33.3 %	43.8 %
Std/Mean W_c (tidal loading)	11.6%	12.5%	12.9%
tidal loading/observation	40.6%	37.5%	29.5%

Our measurements of E_x (average ~ 0.14 m/m) are consistent with the values reported in a previous study ($0.12 - 0.25$ m/m) at the same location using a different imaging sonar (Rona et al., 2006). The entrainment coefficient α (the constant of proportionality relating the entrainment inflows U_e to the centerline vertical velocity of the plume W_c

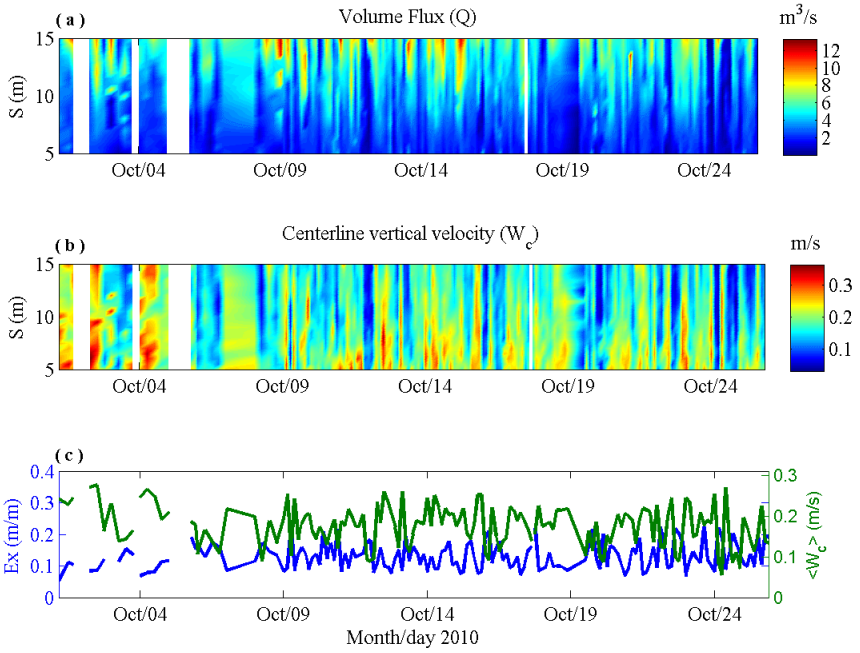

Figure 3.4: 26-day times series of (a) vertical volume transport Q and (b) centerline vertical velocity component W_c along the axial distance range $5 < S < 15$ for the plume above the North Tower of Grotto measured in 2010. (c) Comparison between the 26-day time series of the expansion rate E_x (blue line) and the mean centerline vertical velocity component $< W_c >$ averaged over the axial distance $5 < S < 15$ m (green line). Note that the white stripes in the time series indicate no data were collected at those times. This figure is reproduced from Figure 6 in Xu et al. (2013).

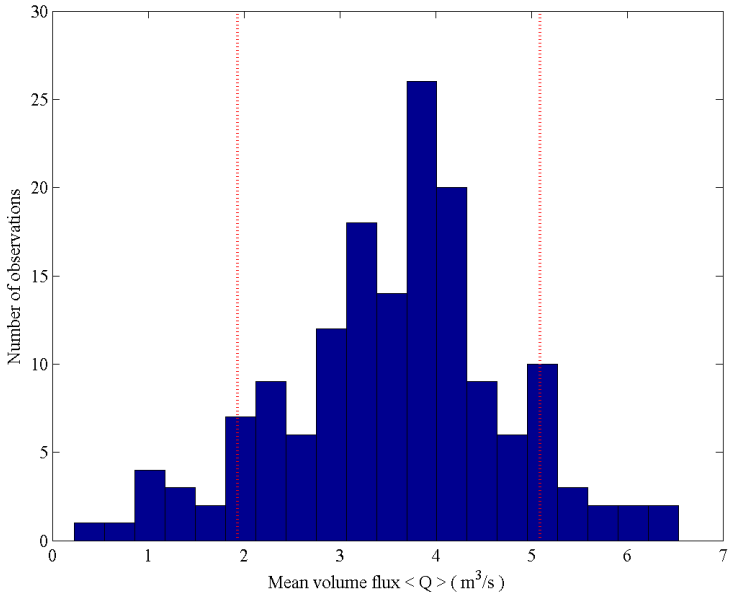

Figure 3.5: Histogram of the mean volume transport $< Q >$ time series. The red dotted lines denotes the cut-offs of the central 80% quantile.

(Morton et al., 1956)) is a key parameter quantifying the mixing of the plume with ambient seawater. Applying the formula generalized in Papanicolaou and List (1988), we calculate the entrainment coefficient α as

$$\alpha = (5/6)E_x/1.2, \tag{3.8}$$

where the factor 1/1.2 is an empirical constant reflecting the assumption that the acoustic backscatter has a cross-sectional profile as dissolved tracers rather than velocity. Laboratory experiments and numerical simulations have estimated α for buoyant plumes in uniform or stably stratified non-flowing (horizontal cross-flows $U_a = 0$) environments (0.083 ± 0.004 (Fischer et al., 1979); 0.083 (Tao et al. (2013), see Appendix G). These estimates fall into the lower sector of our calculated values ($0.06 - 0.14$).

Figure 3.6 shows the smoothed, normalized periodogram of W_c (see Appendix H for the details of the calculation of the periodogram). The periodogram has spectral peaks (with $< 5\%$ significance level) centered at the frequencies consistent with the semi-diurnal tidal constituents (~ 1.95 cycle/day) and the local inertial oscillations (~ 1.5 cycle/day).

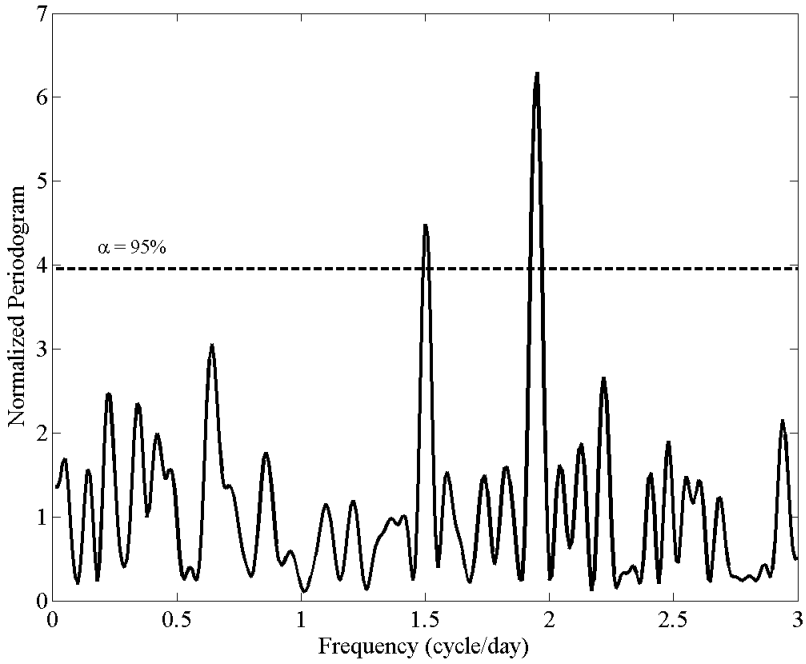

Figure 3.6: Smoothed and normalized periodogram of W_c (refer to Appendix H for the details of the calculation of the periodogram). The dashed line denotes the 5% significance level. This figure is reproduced from Figure 7 in Xu et al. (2013).

Figure 3.7 shows the profiles (averaged over the time series in Figure 3.4(a),(b)) of the variations of Q and W_c over the axial distance range $5 < S < 15$ m. The color-shaded areas denote the uncertainty levels coming from the two error sources mentioned in section 3.1.4. The total uncertainty levels in the vertical volume transport Q and centerline vertical velocity component W_c are approximately 31% and 30% of the results obtained using the default plume boundary at $2b_{sv}$ away from the centerline respectively (blue lines in Figure 3.7).

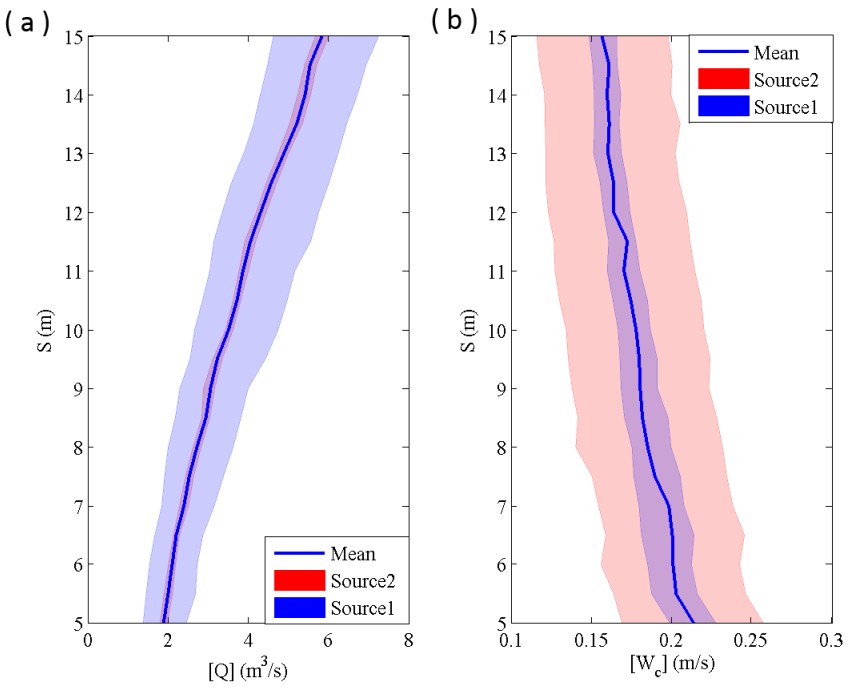

Figure 3.7: Profiles of (a) vertical volume transport $[Q]$ and (b) centerline vertical velocity component $[W_c]$ averaged over the 26-day time series shown in Figure 3.4 with uncertainties caused by the imprecision of the line-of-sight velocity measurements (Source 2, red areas) and by filtering the velocity estimates with the plume boundaries defined at $1.75b_{sv}$ and $2.25b_{sv}$ away from the centerline (Source 1, blue areas); blue lines: mean values calculated with the plume boundary defined at $2b_{sv}$ away from the centerline (see Section 3.1.4) This figure is reproduced from Figure 8 in Xu et al. (2013).

3.3 Discussion

3.3.1 Advances in Data Collection

To illustrate the uniqueness of the COVIS data, we briefly review the few other recent efforts at obtaining time series of plume velocity. Xu and Di Iorio (2012) used acoustic scintillation to obtain a 40-day time series of plume vertical velocity at 20 m above the Dante mound in the MEF. Although this data set is longer than the 26-day time series obtained by processing COVIS data shown in this chapter, each time step only provides a single mean velocity averaged over the 20-m acoustic line-of-sight rather than the complete 3-D data set of 1-m resolution cross-sections at 10 different heights provided by COVIS. Crone et al. (2010) collected 44 days of video of the near vent (first 2m) region of a hydrothermal plume discharging from an individual black smoker on MilliQ vent in the MEF; they used an optical analysis technique to obtain a 44-day record of flow rate changes. While this is also a longer record than the 26-day time series shown in this chapter, it only measures flow from a single black smoker; as a result, extrapolation is required to infer flow through the entire sulfide mound. In contrast, the plume COVIS imaged is fed by all of the 5-6 black smokers distributed on the North Tower of Grotto; thus COVIS's flow and transport measurements reflect more directly the integrated flow through the North Tower portion of the mound.

Thus, the COVIS time series of plume vertical volume transport, centerline vertical flow rate, and expansion rate represent a significant advance in data collection over earlier plume studies due to the ability to track the evolution of the plume (from $\sim$ 5 m to $\sim$ 15 m above the vents along the centerline) and due to the confidence with which the plume is imaged (3-D resolution allows the plume to be accurately located).

3.3.2 Sources of Temporal Variations

Tidal Loading Effects

In previous studies, the tidal loading effects (i.e. response of hydrothermal venting to the changes in seafloor pressure) have been reported to introduce tidal oscillations into the flow rates (Crone et al., 2010) and chemical concentrations and temperatures (Larson et al., 2007)

of the hydrothermal plumes close to the vent orifices. These near-vent tidal oscillations can propagate downstream (vertically) and be observed at higher levels of the plumes. The variations of the temperatures measured by Larson et al. (2007) at high temperature vents orifices are $< 6\%$ of the mean values. The variation in the flow rate within the beginning 2 m of the plume at a high-temperature vent measured by Crone et al. (2010) has a maximum $\sim 40\%$ of the mean value. Given the close proximity of these observations to the vent orifices, it is reasonable to consider them good approximations to the variations of the initial temperatures and flow rate of the plumes observed in the respective studies.

Using the formulations described in Morton et al. (1956); Morton (1959), we calculate the variations of the centerline vertical velocity at multiple levels (5, 10, and 15 m above the vent) of a buoyant plume caused by the initial temperature and flow-rate variations with the observed magnitudes mentioned above (6% for initial temperature and 40% for initial flow rate, see Appendix I). The results (Tables 3.1 and I.1) indicate the tidal loading effects can potentially cause variations in the plume centerline vertical velocity component W_c $\sim 12\%$ of the mean value, which is $\sim 36\%$ of the observed temporal variations. Note that these results are subject to additional uncertainty due to using the variability magnitudes observed at different vents from Grotto; however, the paucity of data gives no better idea of typical (if any) variations.

Current-driven Entrainment

According to Thomson et al. (2003) and Veirs et al. (2006), the semi-diurnal frequency dominates the tidal oscillations in the oceanic currents within the axial valley confining the Grotto mound. In addition, Berdeal (2006) observed significant inertial oscillations in a 11-month (June 2001 - April 2002) time series of the near-bottom (< 1 m above seafloor) horizontal flows measured within the axial valley approximately 100 m to the south of the North Tower of Grotto (Figure 2.2 in Berdeal (2006)). The similar periodicity of the plume centerline vertical velocity component W_c, as is indicated by the presence of the semi-diurnal (~ 2 cycle/day) and inertial (~ 1.5 cycle/day) frequencies in the spectrum (Figure 3.6), is therefore a strong indicator of the plume's response to the ambient oscillatory currents.

As discussed in Section 5.1.2, the plume grows faster (with larger E_x) under greater

entrainment. Larger measured values of E_x, therefore, indicate greater entrainment is occurring. Thus, the significant negative correlation between E_x and the mean centerline vertical velocity component $< W_c >$ shown in Figure 3.4(c) indicates the plume rises slower under enhanced entrainment as more ambient seawater with zero or negligible vertical momentum mixes with the rising plume.

According to previous laboratory and field measurements (Fan, 1967; Rona et al., 2006; Xu and Di Iorio, 2012), ambient horizontal cross-flows (U_a) can enhance entrainment. As reported in Thomson et al. (2003), the currents within the southern sector of the axial valley (where Grotto is) can be decomposed as near-rectilinear tidal oscillations ($\sim$ 3 cm/s, sweeping back and forth along the axis of the axial valley with dominant semi-diurnal constituents) superimposed on a northward mean flow ($\sim$ 5 cm/s). Such ambient currents enhance and introduce tidal oscillations into the entrainment at nearby hydrothermal plumes. Through the negative correlation discussed in the preceding paragraph, the tidally-driven entrainment leads to the similar tidal variability (semi-diurnal band) observed in the plume centerline vertical velocity component W_c (Figure 3.6). In addition, such reasoning explains the fact that our calculated entrainment coefficients (α) are in general larger than empirically determined values for buoyant plumes rising in non-flowing environments (Section 5.1.2).

Although the tidal loading effects discussed in the preceding section can possibly cause $\sim$ 36% of the temporal variations observed in W_c, this theoretical estimation contradicts our observation: surface gravity waves at pure inertial frequency have zero sea-surface height variation; the sea-floor pressure, the source of the tidal loading effects, is thus free of inertial oscillations (Figure 3.8), which contrasts with our observations of strong inertial oscillations in W_c. Such a discrepancy, along with the significant negative correlation of $< W_c >$ with E_x, suggests the dominant source of the temporal variations in W_c is the current-driven entrainment.

3.3.3 Effect of Atmospheric Forcing on Hydrothermal Vents

Based on the current-driven entrainment mechanism described in the preceding section, the near-inertial peak in the spectrum (Figure 3.6) suggests the existence of significant

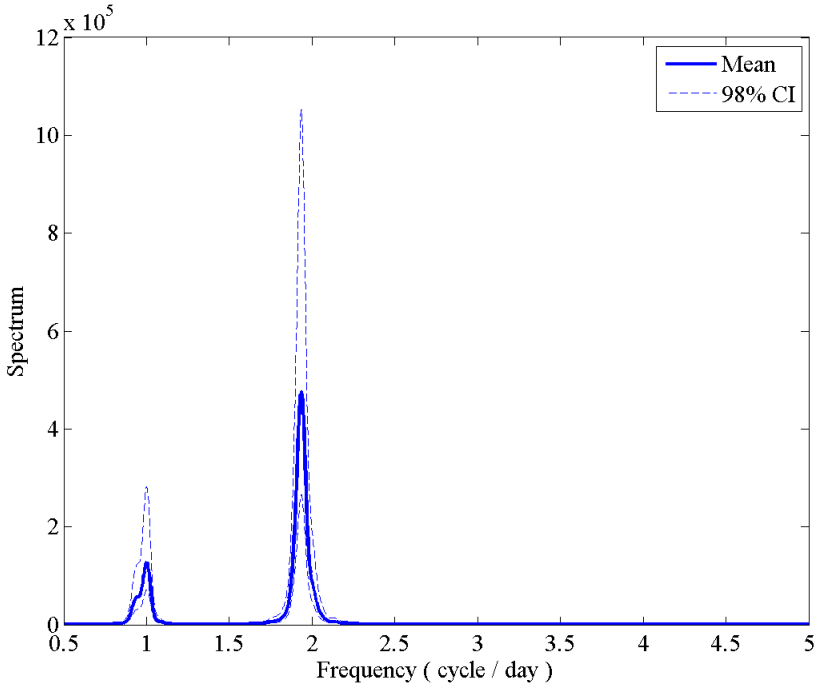

Figure 3.8: Power Spectrum of a year-long seafloor pressure time series (April 1st, 2011 to Apri 1st, 2012) measured by a mooring (RCM-NE, NEPTUNE Canada) deployed approximately 3 km to the north of Grotto within the axial valley. The dashed lines denote the 98% confidence interval of the spectrum (solid line). Note that the spectrum has two spikes at semi-diurnal and diurnal frequencies but no spike within the inertial band (around 1.5 cycle/day).

inertial oscillations in the surrounding currents at Grotto during the measurement period. Atmospheric forcing, such as storms, can generate large inertial oscillations in the surface ocean. Part of the surface-generated inertial energy exits the mixed layer as internal waves that propagate downward to the deep ocean (Thomson et al., 1990). Therefore, it is possible for the observed inertial oscillations to have a surface origin.

In order to investigate the relation between the observed inertial oscillations and the atmospheric forcing, we fit a sinusoidal function with the observed inertial frequency (1.5 cycle/day) to the mean centerline vertical velocity component $< W_c >$ shown in Figure 3.4(c) to isolate the inertial oscillations (Appendix J). We then compare the isolated inertial oscillations with the daily averaged wind speed observed by a buoy (Station 46005, National Data Buoy Center) deployed approximately 230 km to the south of Grotto (Figure 3.9). The typical scale ($\sim$ 1000 km) of the forcing wind in the open ocean is much larger than the horizontal distance ($\sim$ 230 km) between Grotto and the buoy. Therefore, it is reasonable to expect high horizontal coherence between the wind fields at the two locations. Given that the surface generated inertial energy propagates downward at the finite group velocity of internal waves, we anticipate a lag between the plume inertial oscillations and the wind speed. As shown in Figure 3.9, a 13-day lag leads to a maximum correlation coefficient of $R \sim 0.77$ with a near-zero P-value. Assuming this time lag reflects the time taken by the internal waves to transfer the surface-generated inertial energy downward to Grotto (at 2197 m depth), the vertical group velocity of the internal waves is thus

$$C_{gz} = \frac{2197\,\mathrm{m}}{13\,\mathrm{days}} = 169\,\mathrm{m/day}. \tag{3.9}$$

According to Kundu and Thomson (1985), C_{gz} can be calculated as

$$C_{gz} = \frac{U[(2\pi f)^2 - (2\pi f_0)^2]^{3/2}}{4\pi^2 f f_0 N}, \tag{3.10}$$

where f is the 'blue-shifted' inertial frequency observed at the bottom, f_0 is the original inertial frequency, U is the translation speed of a storm, and N is the buoyancy frequency. Substituting equation (3.9) along with $f_0 = 1.4851$ cycle/day, $U = 5$ m/s (Mei et al., 2012) and $N = 0.0063$ rad/s (this value is obtained by averaging the vertical profile of N, which is measured by Emery et al. (1984) in a region close to the MEF, from the bottom of the

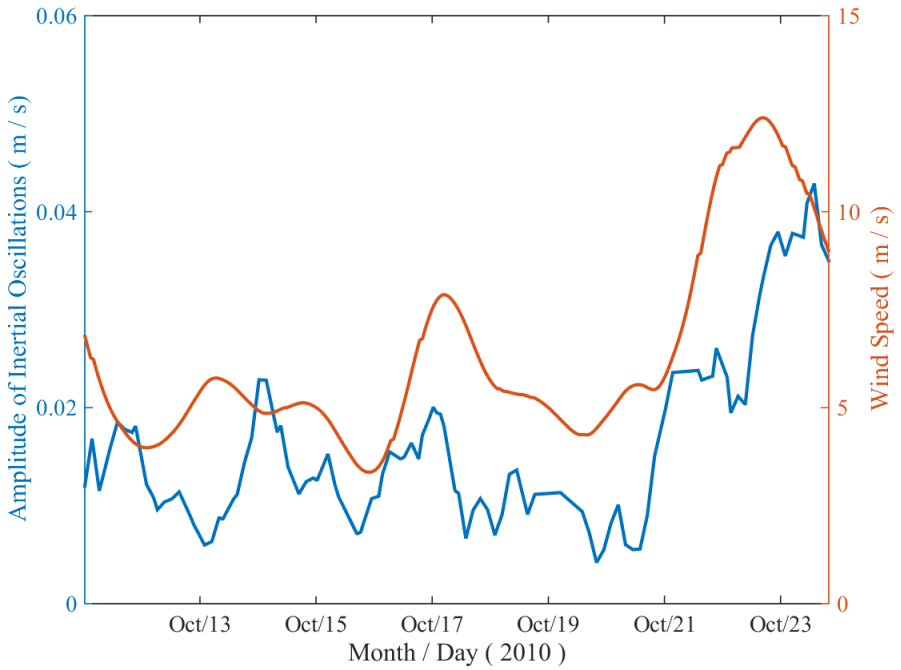

Figure 3.9: Amplitude of the inertial oscillations isolated from the mean centerline vertical velocity component $< W_c >$ shown in Figure 3.4(c) (blue) and daily averaged wind speed observed by a buoy (Station 46005, National Data Buoy Center) deployed 230 km to the south of Grotto with a 13-day lag (orange).

pycnocline to 2000 m depth) into equation (3.10) gives $f = 1.5451$ cycle/day. This value is larger but close to the observed peak of the inertial band ($f \sim 1.5$ cycle/day, Figure 3.6) given the resolution of the spectrum $\Delta f \sim 0.06$ cycle/day.

The significant correlation between the amplitude of the isolated plume inertial oscillations and the wind speed observed by the buoy, along with the consistency between the observed and calculated 'blue-shifted' inertial frequencies, suggests the downward propagation of the surface-generated inertial energy into the ambient currents at Grotto. The inertial oscillations are then introduced into the plume vertical velocity component W_c through the current-driven entrainment discussed in the previous section. This discovery is evidence for the influence of atmospheric forcing on the dynamics of hydrothermal plumes, which was largely overlooked in previous vent studies. Similar evidence was reported in Adams et al. (2011) for the influence of surface-generated mesoscale eddies on the low-frequency background currents around a hydrothermal vent field. The downward propagation of surface-generated inertial oscillations into vent fields has potential to influence the transport of hydrothermal chemical and heat transports and the dispersal of larvae of vent animals.

3.4 Chapter Summary

In this chapter, we use the Doppler-processed data from the Cabled Observatory Vent Imaging Sonar (COVIS) to measure a 26-day time series of the vertical volume transport, centerline vertical velocity component and expansion rate of the buoyant plume discharging from a venting sulfide structure. We present methods of acoustic data processing and uncertainty quantification. The results support COVIS's capability of long-term measurement of the volume transport and flow rate of a hydrothermal plume with reasonable uncertainty levels. The temporal variability of the flow rate shows frequencies of the inertial oscillations and the semi-diurnal tidal constituents, which reflects the plume's response to the ambient ocean currents within the axial valley through current-driven entrainment. The observed inertial oscillations in the plume's flow rate suggest a significant influence of atmospheric forcing on the dynamics of hydrothermal plumes.

Chapter 4

Time-series Measurements of the Dynamics of a Deep-sea Hydrothermal Plume: 2011-2015 data

This chapter aims to further explore the temporal variations of the dynamics of a buoyant hydrothermal plume and its interactions with the hydrodynamic processes in the ambient water column based on the 41-month extension (October 2011 to February 2015, Ocean Networks Canada Data Archive (2015b)) to the 26-day time-series measurements of the volume transport, vertical flow rate, and expansion rate of the North Tower plume above Grotto presented in Chapter 3. The temporal variations observed in the 41-month time-series corroborate the findings in Section 3.3.2 regarding the influences of ocean currents on the mixing of the plume with the ambient seawater. In addition, we estimate the ambient horizontal currents near Grotto from the bending angles of the North Tower plume. We then compare the estimated horizontal currents with those measured by the ADCP (Ocean Networks Canada Data Archive, 2015a) deployed approximately 80 m to the south of Grotto, which reveals the complexity of the horizontal flow field within the MEF.

4.1 Plume Property Time Series: 2011-2015

Figure 4.1 shows the 41-month time series of the vertical volume transport Q of the North Tower plume over axial distance $5 \leq S \leq 15$ m obtained by processing COVIS Doppler-mode data recorded from October 2011 to February 2015. Similar to the 26-day time series shown in Figure 3.4(a), the 41-month volume transport times series has strong short-term variations but no pronounced long-term trend. The mean vertical volume transport $< Q >$ averaged over the axial distance $5 \leq S \leq 15$ m has a standard deviation of $1.26\,\mathrm{m}^3/\mathrm{s}$ which is 40% of the mean (Figure 4.2). In addition, the time series features a slight decreasing trend with a slope of -0.13 m^3/s per year with the 95% confidence interval (CI) of [-0.16,

-0.10] m^3/s per year. The short-term variations of Q feature strong tidal modulation which is evident in the smoothed, normalized spectrum calculated from the time series of Q between January 2012 and May 2014 following the procedures detailed in Appendix H (Figure 4.3). The spectrum suggests the principal lunar semi-diurnal constituent M_2 dominates the tidal oscillations in Q. The other significant tidal constituents observed in the spectrum include the principal solar semi-diurnal constituent S_2, the larger lunar elliptic semi-diurnal constituent N_2, and the lunar diurnal constituents K_1 and O_1. In addition, there is a significant peak at 14-day periodicity caused by the spring-neap tidal cycle in the magnitude of tidal current velocity.

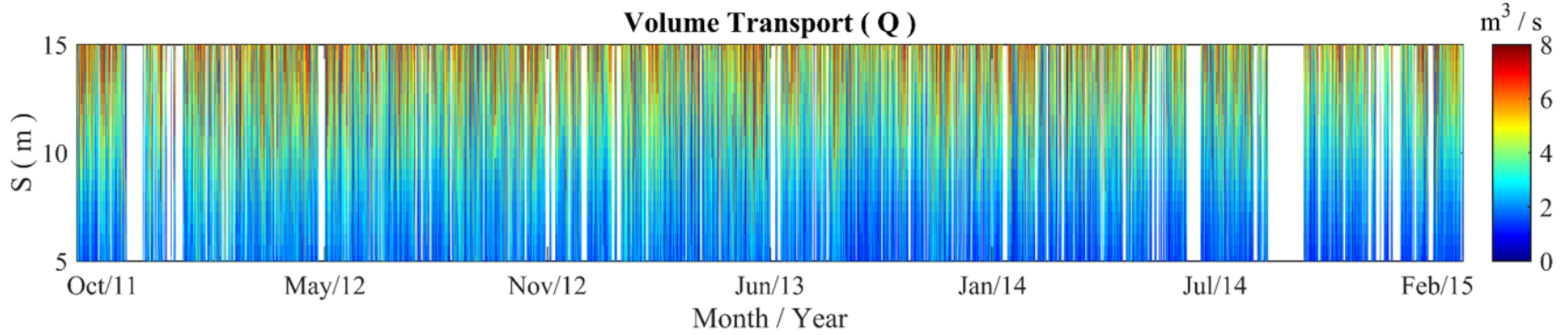

Figure 4.1: Time series of the vertical volume transport Q of the North Tower plume over axial distance $5 \leq S \leq 15$ m from October 2011 to February 2015.

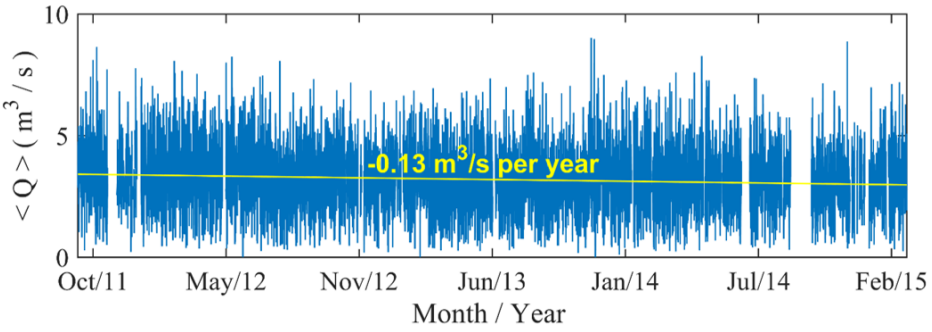

Figure 4.2: Time series of the mean vertical volume transport $< Q >$ averaged over axial distance $5 \leq S \leq 15$ m from October 2011 to February 2015. The yellow line marks the linear regression with a slope of -0.13 m^3/s per year. The 95% confidence interval of the slope is [-0.16 -0.10] m^3/s per year.

Figure 4.4 shows the 41-month time series of the centerline vertical velocity component W_c of the North Tower plume over axial distance $5 \leq S \leq 15$ m obtained by processing COVIS Doppler-mode data recorded from October 2011 to February 2105. Figure 4.5 shows the time series of the mean centerline vertical velocity component $< W_c >$ averaged over the axial distance $5 \leq S \leq 15$ m, which has a standard deviation of 0.049 m/s that is 25% of the mean. In addition, the time series features a slight decreasing trend with a slope of -0.44 cm/s per year with . Similar to the time series of Q shown in Figure 4.1, the times series of W_c has strong short-term variations but no pronounced long-term trend. As is shown in Figure 4.5, the mean centerline vertical velocity component $< W_c >$ averaged over the axial distance $5 \leq S \leq 15$ m has a standard deviation of 0.049 m/s that is 25% of the mean. In addition, the time series features a slight decreasing trend with a slope of -0.44 cm/s per year with the 95% CI of [-0.55 -0.33] cm/s per year. The short-term variations of W_c feature strong tidal modulation which is evident in the smoothed, normalized spectrum calculated from the time series of W_c between January 2012 and May 2014 following the procedures detailed in Appendix H (Figure 4.6). Similar to Q, the M_2 constituent dominates the tidal oscillations in W_c. However, the diurnal tidal constituents K_1 and O_1 observed in Q are absent from the spectrum of W_c which also has a more pronounced peak at the 14-day periodicity caused by the spring-neap tidal cycle.

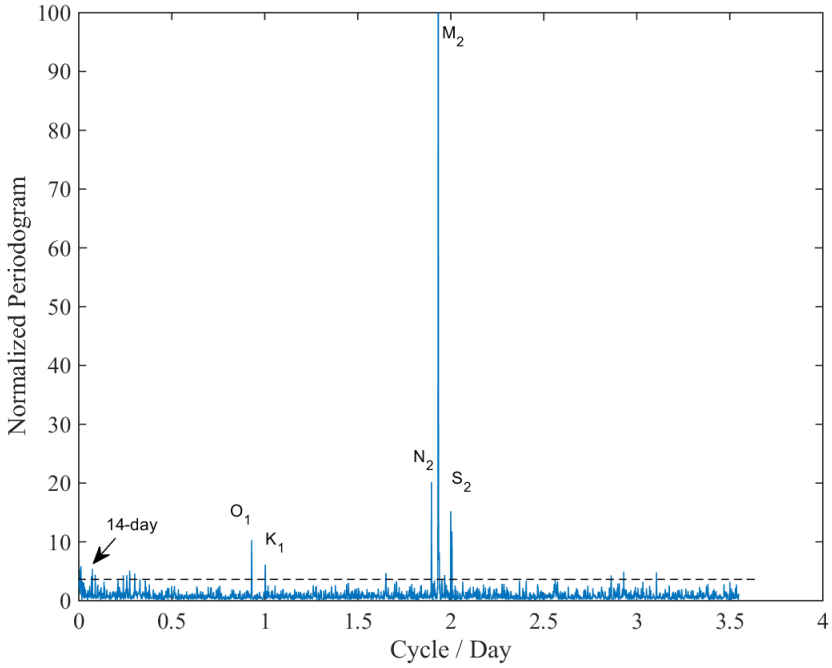

Figure 4.3: Smoothed, normalized periodogram calculated from the time series of Q between January 2012 and May 2014 following the procedures given in Appendix H. The dashed line marks the 5% significance level and the labels denote the significant tidal constituents. The peak of the semi-diurnal constituent M_2 is clipped at 100 to make the other peaks discernible. The actual M_2 peak is at 258.

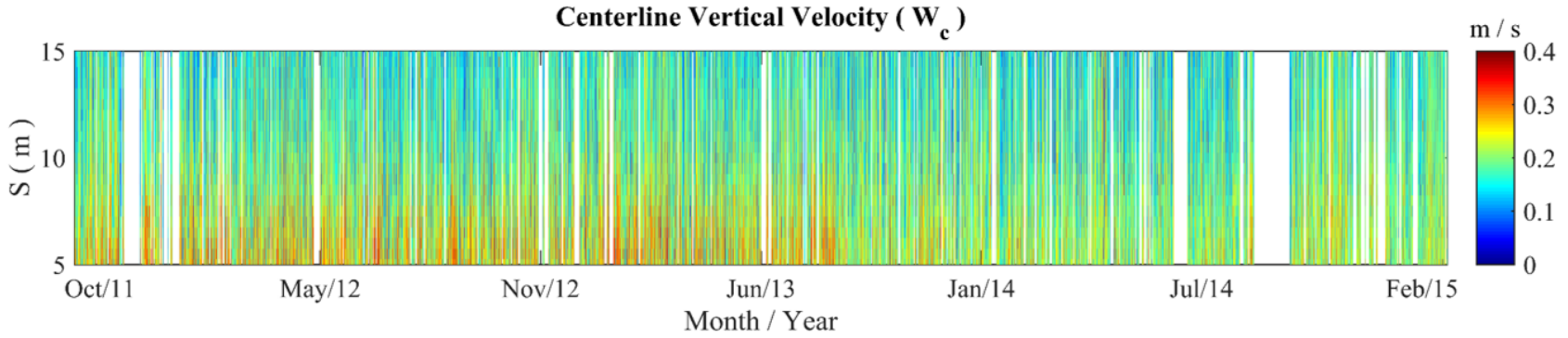

Figure 4.4: Time series of the centerline vertical flow rate W_c of the North Tower plume over axial distance $5 \leq S \leq 15$ m from October 2011 to February 2015.

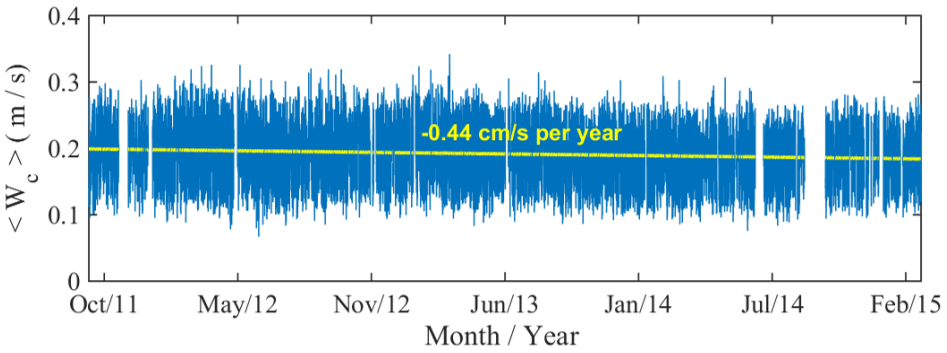

Figure 4.5: Time series of the mean centerline vertical velocity component $< W_c >$ averaged over axial distance $5 \leq S \leq 15$ m from October 2011 to February 2015. The yellow line marks the linear regression with a slope of -0.44 cm/s per year. The 95% confidence interval of the slope is [-0.55 -0.33] cm/s per year.

4.2 Current-driven Entrainment with Further Evidence

The presence of significant tidal oscillations in Q and W_c is further evidence that the tidal oscillations in the ambient currents are introduced into the flow field of the North Tower plume through the current-driven entrainment discussed in Section 3.3.2. To corroborate this idea, we compare the plume's mean vertical velocity component $< W_c >$ with its expansion rate E_x. The result suggests there is a negative correlation between $< W_c >$ and E_x with a correlation coefficient $R \sim -0.61$ and a P-value $\ll 10^{-6}$ over the 41-month period from October 2011 to February 2015 (Figure 4.7). As discussed in Section 3.3.2, the negative correlation between E_x and $< W_c >$ suggests the plume rises slower and grows faster under enhanced entrainment as more ambient seawater with zero or negligible vertical momentum mixes with the rising plume. To test the hypothesis that the enhanced entrainment is driven by ambient currents, we need to know the horizontal cross-flows in the vicinity of the North Tower plume. Because a plume injected into a cross-flow will bend towards its downstream direction, we can estimate the direction of the horizontal cross-flow in the vicinity of the North Tower plume from the azimuthal angle (Φ) of the plume's centerline. In addition, since the plume will bend more when the cross-flow is stronger, we can estimate the relative amplitude of the cross-flow from the inclination angle (Θ) of the plume's centerline. In

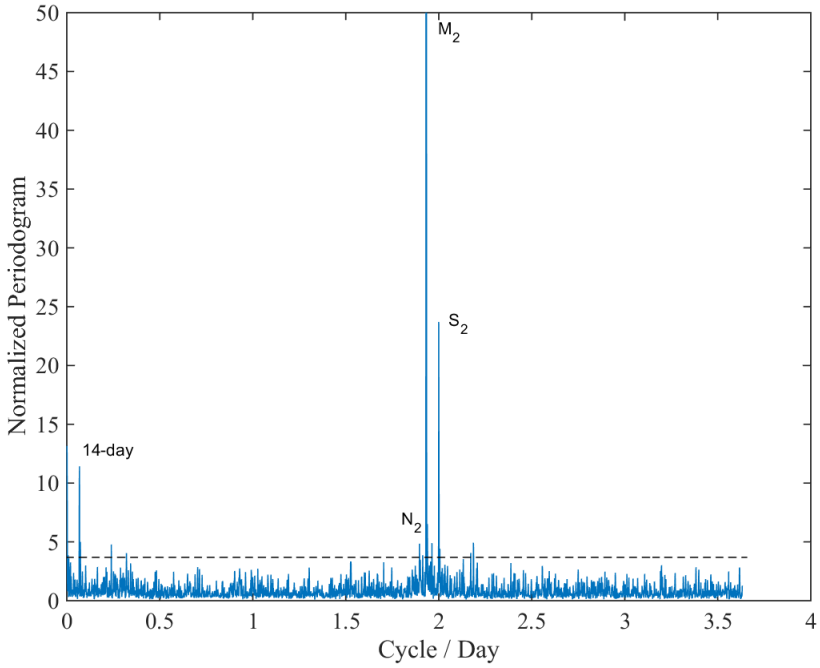

Figure 4.6: Smoothed, normalized periodogram calculated from the time series of W_c between January 2012 and May 2014 following the procedures given in Appendix H. The dashed line marks the 5% significance level and the labels denote the significant tidal constituents. The peak of the semi-diurnal constituent M_2 is clipped at 50 to make the other peaks discernible. The actual M_2 peak is at 348.

practice, we estimate Φ and Θ by fitting a straight line in the least-squares sense to the local volume backscattering coefficient (s_v) maxima on successive horizontal cross-sections of the grid used in the Doppler mode (Figure 4.8). Subsequently, we determine Φ as the angle between the projection of the best-fit line on the horizontal plane and the x-axis and Θ as the angle between the best-fit line and the vertical axis (Figure 4.8). In this way, we construct the relative cross-flow velocity $\mathbf{U_r}$ as

$$\mathbf{U_r} = [\mathbf{u_r}, \mathbf{v_r}] \tag{4.1}$$

$$u_r = \frac{\Theta}{\pi}\cos(\Phi) \tag{4.2}$$

$$v_r = \frac{\Theta}{\pi}\sin(\Phi) \tag{4.3}$$

where u_r and v_r are the east-west, north-south components of $\mathbf{U_r}$. The factor $\frac{1}{\pi}$ is used to make u_r and v_r dimensionless. Figure 4.9 is a scatter plot of $\mathbf{U_r}$ estimated from the plume bending angles obtained from COVIS backscatter data recorded from October 2011 to February 2015. According to the figure, $\mathbf{U_r}$ is mainly confined in the north-south direction with an asymmetry favoring the northward flow. The first principal axis of the velocity vector obtained using principal component analysis (PCA) approximately aligns with true north with an offset of 1.59° towards north-northwest. Figure 4.10 is a scatter plot between the amplitude of the relative cross-flow velocity Θ/π and E_x. According to the figure, there is a positive correlation between the two variables with a correlation coefficient $R \sim 0.78$ and a P-value $\ll 10^{-6}$. This result suggests the entrainment of ambient fluids into the plume increases with the amplitude of ambient cross-flow, which corroborates the current-driven entrainment discussed in Section 3.3.2.

4.3 Bottom Currents at MEF

The interactions amongst ambient currents, buoyant plumes, and bottom topography generates a complex flow field within the axial valley on the Endeavour Segment, which plays a key role in the recruitment of vent larvae and their along-ridge transport to adjacent vent fields. Previous study suggests the bottom currents within the axial valley features attenuated, rectified tidal and wind-driven oscillations superimposed on a steady near-bottom inflow that is driven by hydrothermal plumes (Thomson et al., 2003). The inflow draws

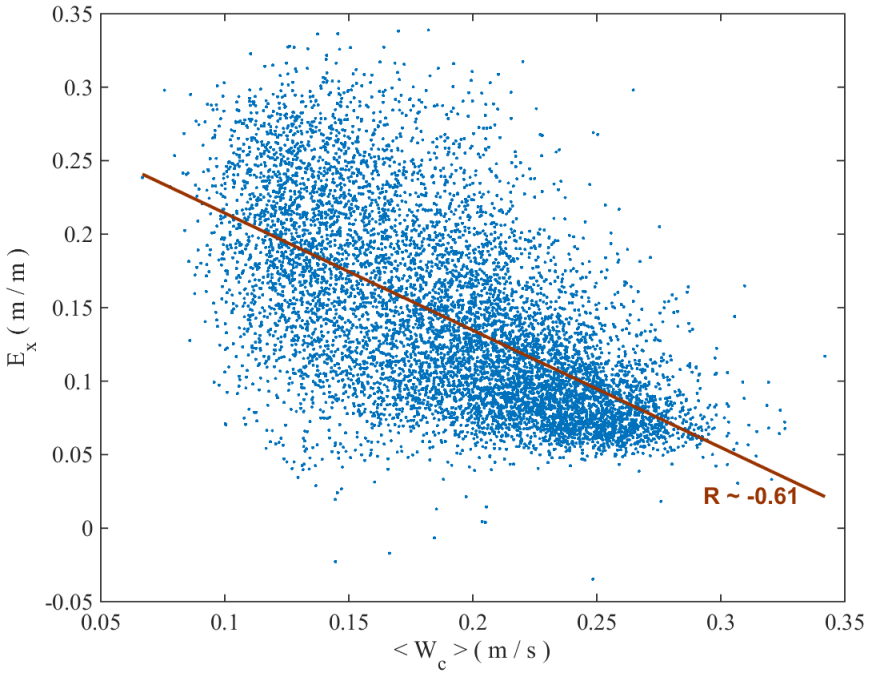

Figure 4.7: Scatter plot between plume mean centerline vertical velocity component $< W_c >$ and expansion rate E_x over the 41-month period from October 2011 to February 2015. The solid line is the linear regression. The correlation coefficient between $< W_c >$ and E_x is $R \sim -0.61$ with a P-value $\ll 10^{-6}$.

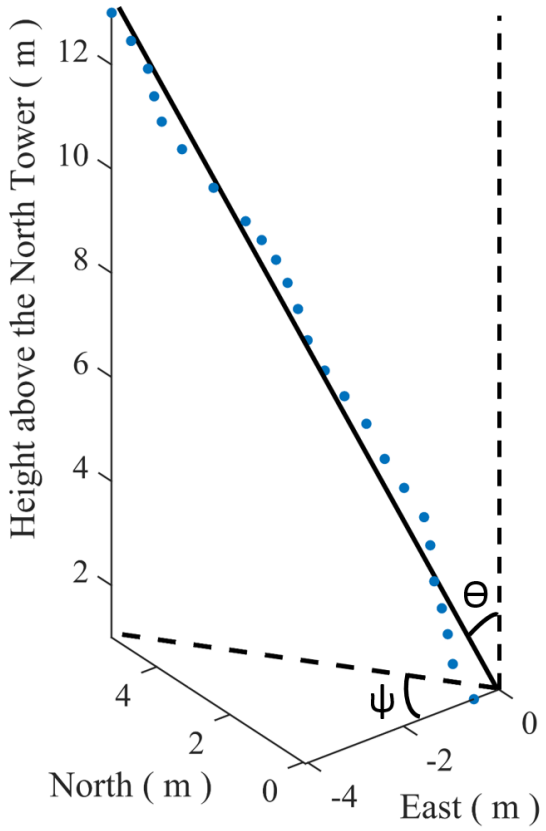

Figure 4.8: Construction of plume centerline from the 3-D gridded acoustic backscattering coefficient (s_v) collected on October 17th, 2010. Solid line: least-squares linear fit; dashed line: projection of the least-squares fit on the horizontal plane; blue dots: s_v maxima on successive horizontal cross sections. The azimuthal (Φ) and inclination (Θ) angles of the centerline are marked.

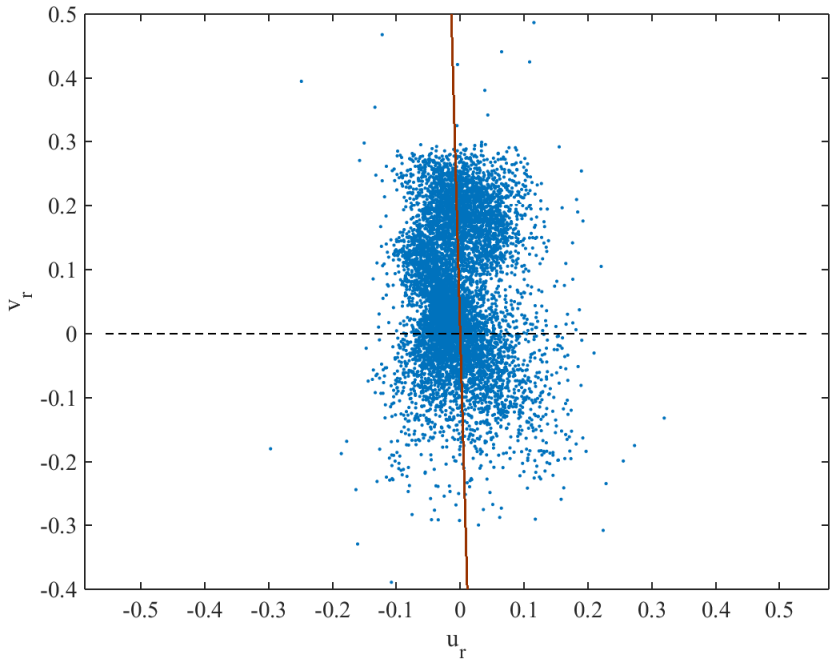

Figure 4.9: Scatter plot of the relative cross-flow velocity estimated from the plume bending angles obtained from the backscatter data recorded in the 41-month period from October 2011 to February 2015. The horizontal dashed line marks $V_r = 0$, and the solid line denotes the first principal axis of the velocity vector obtained using principal component analysis.

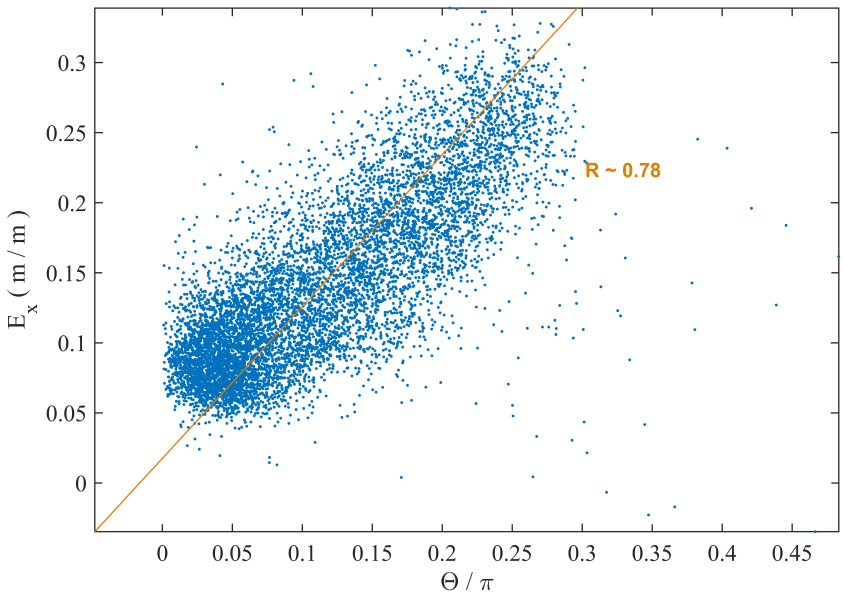

Figure 4.10: Scatter plot between the amplitude of relative cross-flow velocity Θ/π and plume expansion rate E_x over the 41-month period from October 2011 to February 2015. The solid line is the linear regression. The correlation coefficient between the two variables is $R \sim 0.78$ with a P-value $\ll 10^{-6}$.

bottom seawater into the valley from its two ends in the north and south. The northward inflow at the southern end is stronger than the southward inflow at the northern end. Such a difference is likely due to the higher hydrothermal output and deeper confinement in the southern and central sectors of the valley (Thomson et al., 2003).

4.3.1 Relative Cross-flow Velocity

In Section 4.2, we estimate the relative cross-flow velocity $\mathbf{U_r}$ from the orientation of the centerline of the North Tower plume. The result can serve as a proxy for the ambient currents in the immediate vicinity above the North Tower of Grotto. Figure 4.11 shows the rotary spectrum of $\mathbf{U_r}$ obtained from COVIS backscatter data recorded between June 2013 and February 2015 (Ocean Networks Canada Data Archive, 2015b) calculated using the Lomb-Scargle periodogram following the procedures described in Pardo-Iguzquiza and Rodriguez-Tovar (2012). Note that the aforementioned time range is chosen for the comparison of $\mathbf{U_r}$ with the measurements made by the acoustic Doppler current profiler (ADCP) discussed in the following section. According to the spectrum, the semi-diurnal constituent M_2 dominates the oscillations in $\mathbf{U_r}$. The clockwise component of M_2 is slightly larger than its counter-clockwise component. The second strongest signal in the spectrum is the S_2 semi-diurnal constituent, whose counter-clockwise component is slightly larger than the clockwise component. The diurnal constituents K_1 and O_1 are also present in the spectrum with much reduced magnitude compared with M_2 and S_2. The rotations of K_1 and O_1 currents are predominantly counter-clockwise.

Figure 4.12 shows the current ellipse of the M_2 constituent in $\mathbf{U_r}$. The tidal information needed to plot the ellipse is extracted from $\mathbf{U_r}$ using the harmonic analysis software T-Tide (Pawlowicz et al., 2002). Since T-Tide only works on evenly-spaced time series, we need to first fill the data gaps in $\mathbf{U_r}$ and turn it into an even-spaced time series. In practice, we calculate the complex Fourier spectrum of $\mathbf{U_r}$ using the method described in Hocke and Kampfer (2009) for unevenly spaced time series. Subsequently, taking the inverse Fourier transform of the complex spectrum gives an evenly-spaced time series of $\mathbf{U_r}$, to which T-Tide can be readily applied. Note that the evenly-spaced time series of $\mathbf{U_r}$ constructed this way preserves the frequency signatures of the original time series. According to Figure 4.12,

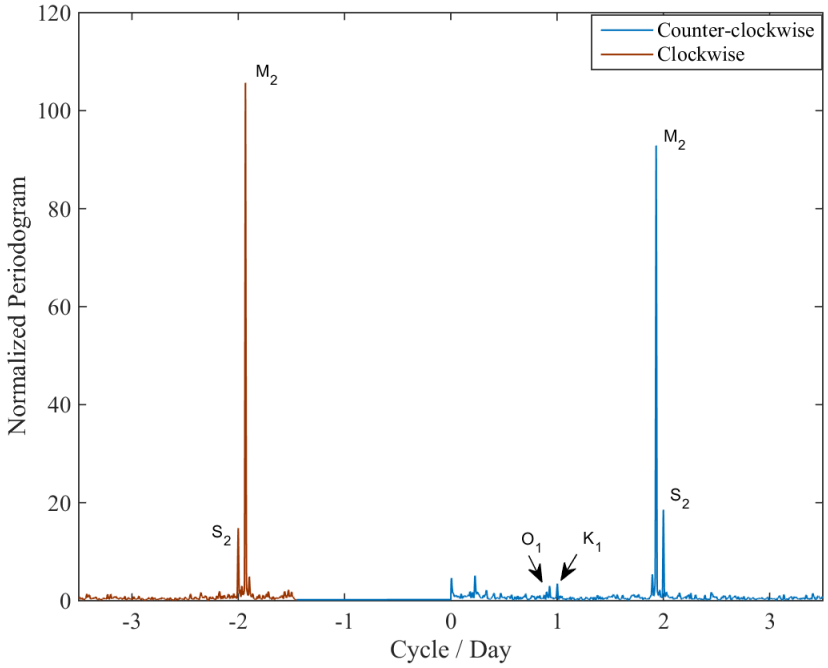

Figure 4.11: Rotary spectrum of the relative cross-flow velocity $\mathbf{U_r}$ from June 2013 to February 2015 calculated using the Lomb-Scargle periodogram following the procedures described in Pardo-Iguzquiza and Rodriguez-Tovar (2012). The negative frequencies refer to clockwise rotations and the positive frequencies refer to counter-clockwise rotations. The labels denote major tidal constituents.

the M_2 oscillations in $\mathbf{U_r}$ are nearly rectilinear with a major axis offsetting the north by 15° towards the northeast. Figure 4.13 shows the current ellipse of the S_2 constituent in $\mathbf{U_r}$. Similar to M_2, the S_2 currents are nearly rectilinear with the major axis offsetting the north by 10° towards the northeast.

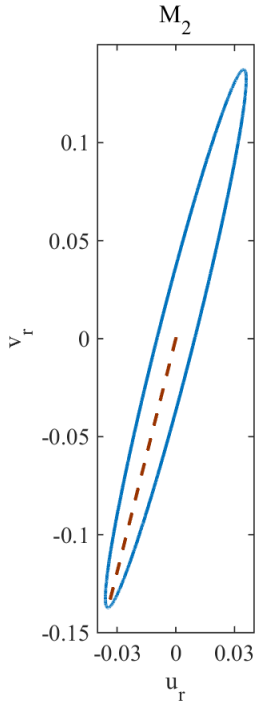

Figure 4.12: Current ellipse for the M_2 tidal constituent of $\mathbf{U_r}$. The angle between the dashed lines and the top vertice of the ellipse (clockwise rotation) mark the Greenwich phase of the constituent—the time shift between the peak northward flow and the time when the equilibrium forcing for the constituent is at its largest positive value at 0° longitude.

Figure 4.14 shows the power spectrum of the magnitude of the relative cross-flow velocity $|\mathbf{U_r}|$ from June 2013 to February 2015 calculated using the Lomb-Scargle periodogram following the procedures described in Pardo-Iguzquiza and Rodriguez-Tovar (2012). The similarity of this spectrum with those of plume vertical volume transport Q and centerline vertical velocity component W_c shown in Figures 4.3 and 4.6 further corroborates the idea that the tidal oscillations in Q and W_c originate from the ambient currents and are introduced into the plume through the current driven entrainment discussed in Sections 4.2 and 3.3.2.

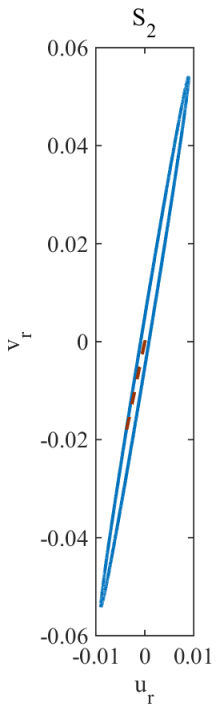

Figure 4.13: Current ellipse for the S_2 tidal constituent of $\mathbf{U_r}$. See caption of Figure 4.12 for graphical convention.

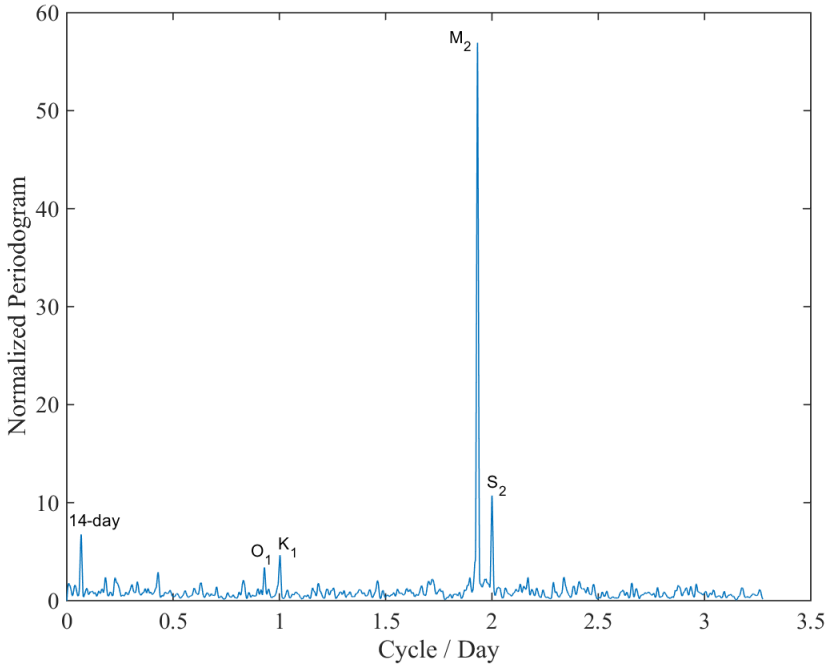

Figure 4.14: Power spectrum of the magnitude of the relative cross-flow velocity $|\mathbf{U_r}|$ from June 2013 to February 2015 calculated using the Lomb-Scargle periodogram following the procedures described in Pardo-Iguzquiza and Rodriguez-Tovar (2012).

Figure 4.15 shows the 36-hour mean current vectors of $\mathbf{U_r}$ from June 2013 to February 2015. The mean currents are predominantly northward with brief episodes of flow reversal that account for $< 6\%$ of the measurement duration. Figure 4.16 shows the mean current vector of $\mathbf{U_r}$ averaged from June 2013 to February 2015. The direction of the mean current is approximately northward with a 10 degree offset towards northeast. The predominantly northward mean current is consistent with the previous observations of prevalent northward mean flow within the southern and central axial valley (Thomson et al., 2003). The magnitude of the mean current, 0.2, exceeds the magnitude of the dominant M_2 oscillations, 0.14, by approximately 40%.

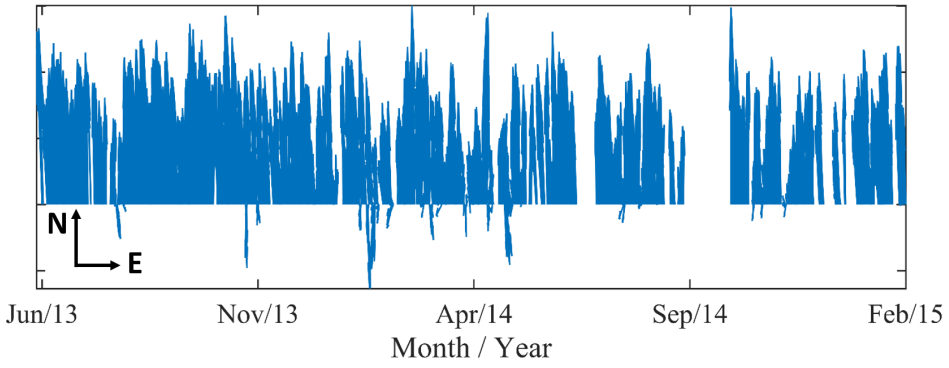

Figure 4.15: 36-hr mean current vectors of $\mathbf{U_r}$ from June 2013 to February 2015.

4.3.2 ADCP measurements

In June 2013, an acoustic Doppler current profiler (ADCP) was installed in the NEPTUNE observatory at 2189 m depth and approximately 100 m to the southwest of COVIS and midway between Grotto and Bastille—a large venting sulfide structure in the southern half of the MEF (Figure 4.17). The ADCP monitors the horizontal currents within 3 to 30 m above the seafloor. Figure 4.18 shows the rotary spectra of the horizontal current velocity $\mathbf{U}$ measured by the ADCP at 3, 13, and 27 m above the seafloor from June 2013 to February 2015 respectively (Ocean Networks Canada Data Archive, 2015a). According to Figure 4.18, the M_2 tidal constituent dominates the oscillatory flows at all three levels, of which the clockwise component is slightly larger than the counter-clockwise component.

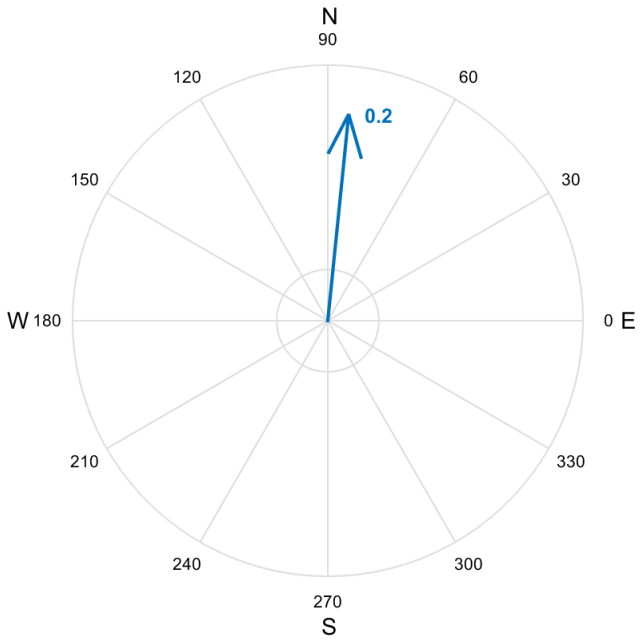

Figure 4.16: Compass plot of the mean current vector of $\mathbf{U_r}$ averaged from June 2013 to February 2015. The magnitude of the mean current is marked.

In addition, the diurnal constituents K_1 and O_1 are predominantly clockwise at all three levels .

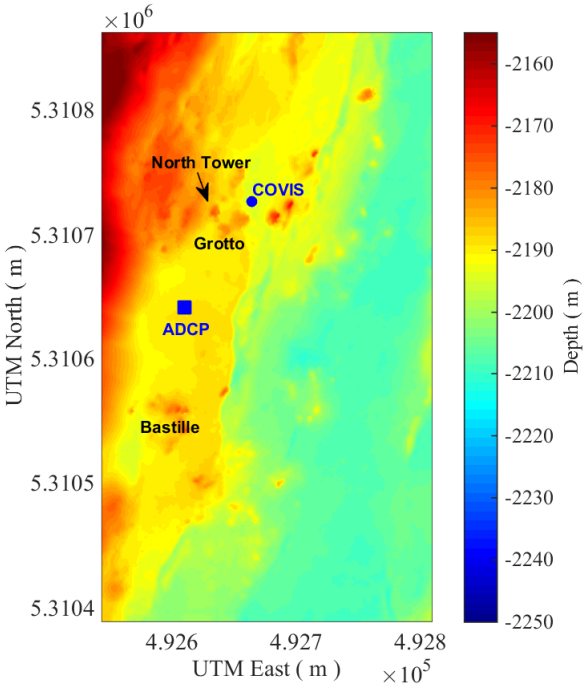

Figure 4.17: Bathymetric map of the Main Endeavour Field. The blue dot marks the location of COVIS. The blue square marks the location of the ADCP, which is approximately 100 m to the southwest of COVIS.

Figure 4.19 shows the current ellipses for the M_2 tidal constituent at 3, 13, and 27 m above the seafloor. In practice, we use the harmonic analysis software T-Tide to extract the tidal information needed to plot the ellipses from the time series of **U** between June 2013 and February 2015 (Pawlowicz et al., 2002). As shown in the figure, the M_2 currents are nearly rectilinear with predominant north-south components at all three levels. The major semi-axes of the ellipses increase from 3.2 cm/s at 3 m to 4.3 cm/s at 27 m above the seafloor. The major axis aligns with the north at 3 and 13 m above the seafloor, whereas the major axis at 27 m above offsets the north by 4° towards the northeast. Figures 4.20 to 4.22 show the current ellipses for the S_2, O_1, and K_1 tidal constituents at 3, 13, and 27 m above the seafloor. Similar to M_2, the S_2 currents are nearly rectilinear with predominant north-south component at all three depths. The major semi-axes increases from 1.1 cm/s

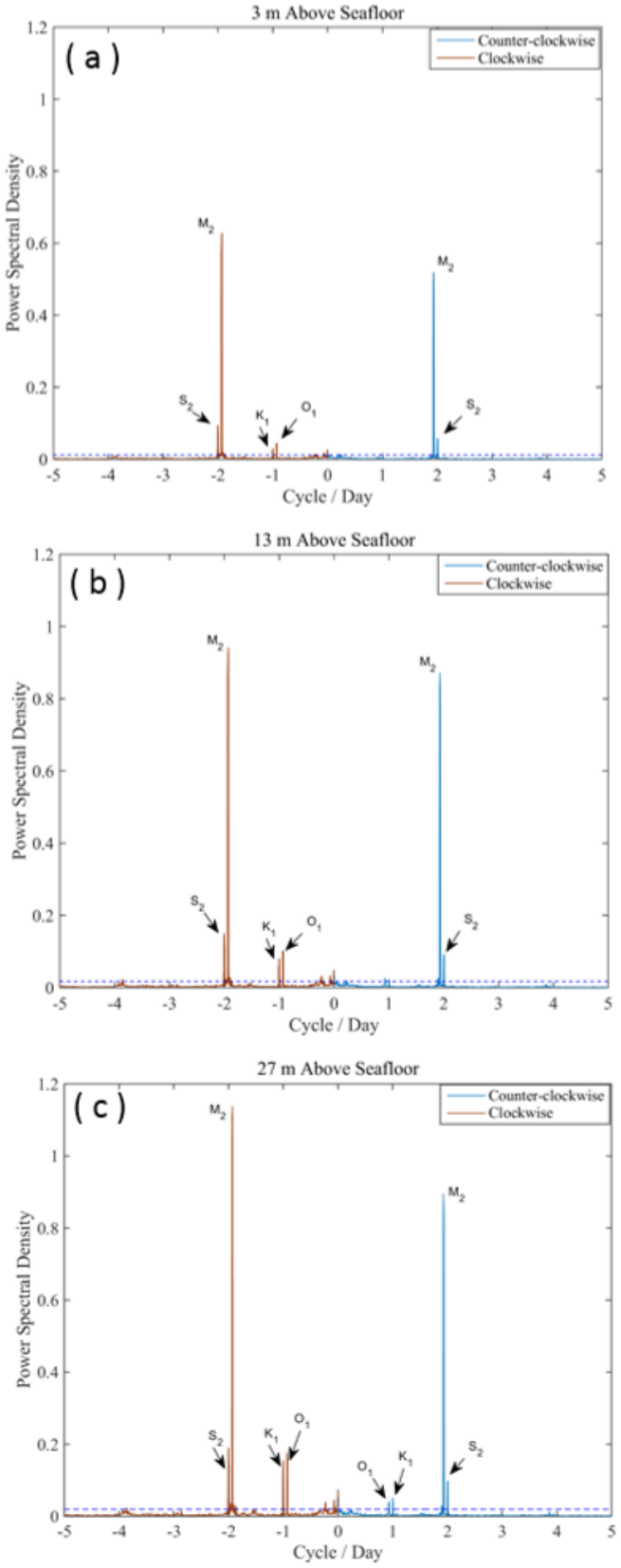

Figure 4.18: Rotary spectra calculated using the multi-taper method of the horizontal current velocity **U** measured by the ADCP at 3 (a), 13 (b), and 27 m (c) above the seafloor from June 2013 to February 2015. The horizontal dashed line marks the 5% significance level. The labels denote significant tidal constituents.

at 3 m to 1.5 cm/s at 27 m above the seafloor, which offsets the north by 7° at all three levels. For the diurnal constituents, the K_1 and O_1 currents are more circular compared to M_2 and S_2. For both K_1 and O_1, the major semi-axes of the ellipses increases with the height above the seafloor with northwest orientations.

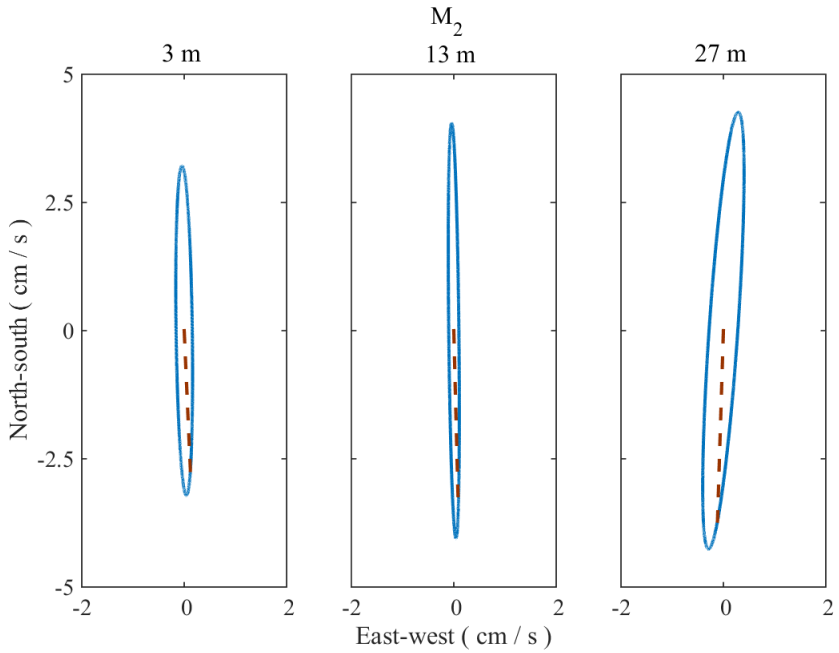

Figure 4.19: Current ellipses for the M_2 tidal constituent of **U** at 3, 13, and 27 m above the seafloor. The angle between the dashed lines and the top vertices of the ellipses (clockwise rotation) mark the Greenwich phase of the constituent—the time shift between the peak northward flow and the time when the equilibrium forcing for the constituent is at its largest positive value at 0° longitude.

Figure 4.23 shows the 36-hour mean current vectors of **U** measured by the ADCP at 3, 13, and 27 m above the seafloor from June 2013 to February 2015. At 3 m above the seafloor, the 36-hour mean currents are predominantly northward with brief episodes of flow reversal that account for $\sim 8\%$ of the measurement duration. At 13 m, the flow reversals occur much more frequently with northward currents accounting for $\sim 60\%$ of the time. At 27 m, the mean currents are predominantly southward with northward currents accounting for $\sim 20\%$ of the time. These results suggest there is a vertical shear present in the mean currents measured by the ADCP with northward flows near the bottom and southward flow

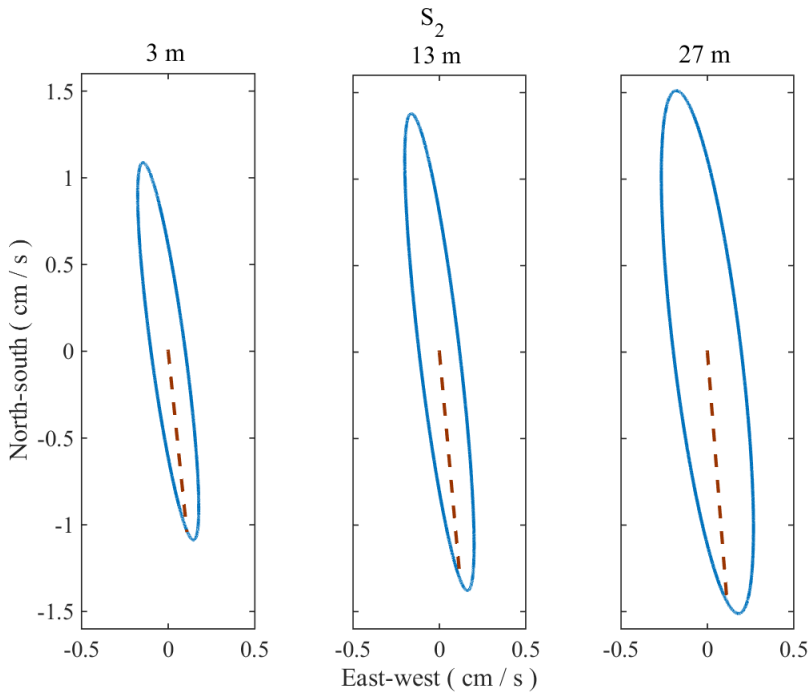

Figure 4.20: Current ellipses for the S_2 tidal constituent of **U** at 3, 13, and 27 m above the seafloor. See caption of Figure 4.19 for graphical convention

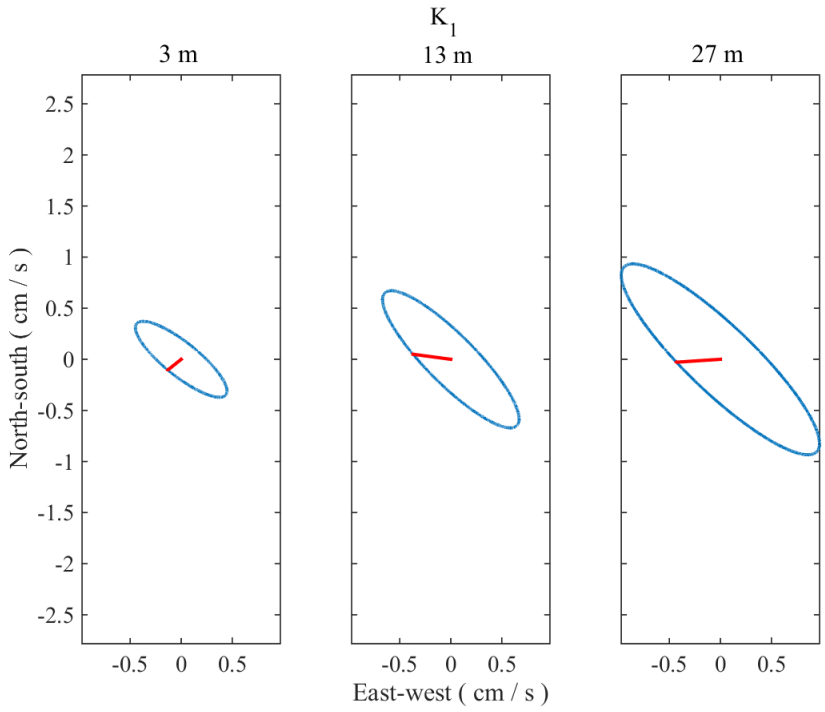

Figure 4.21: Current ellipses for the K_1 tidal constituent of **U** at 3, 13, and 27 m above the seafloor. See caption of Figure 4.19 for graphical convention

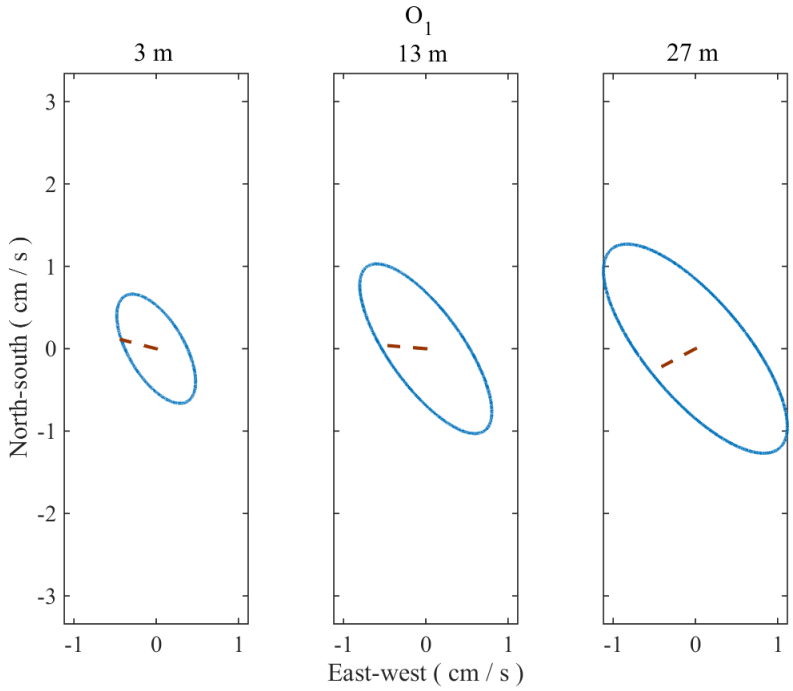

Figure 4.22: Current ellipses for the O_1 tidal constituent of **U** at 3, 13, and 27 m above the seafloor. See caption of Figure 4.19 for graphical convention

at 27 m above. Figure 4.24 is a compass plot showing the mean current vectors averaged over the measurement duration from 3 to 27 m above the seafloor in 4 m increments. As shown in the figure, the mean currents rotate clockwise from 15° due north at 3 m to near-southward at 27 m. The magnitudes of mean currents decrease from 3 to 15 m and increase thereafter to reach a similar magnitude at 27 m as at 3 m. The magnitude of mean currents at 3 m, 1.5 cm/s, is approximately 50% of the dominant M2 currents at the same level.

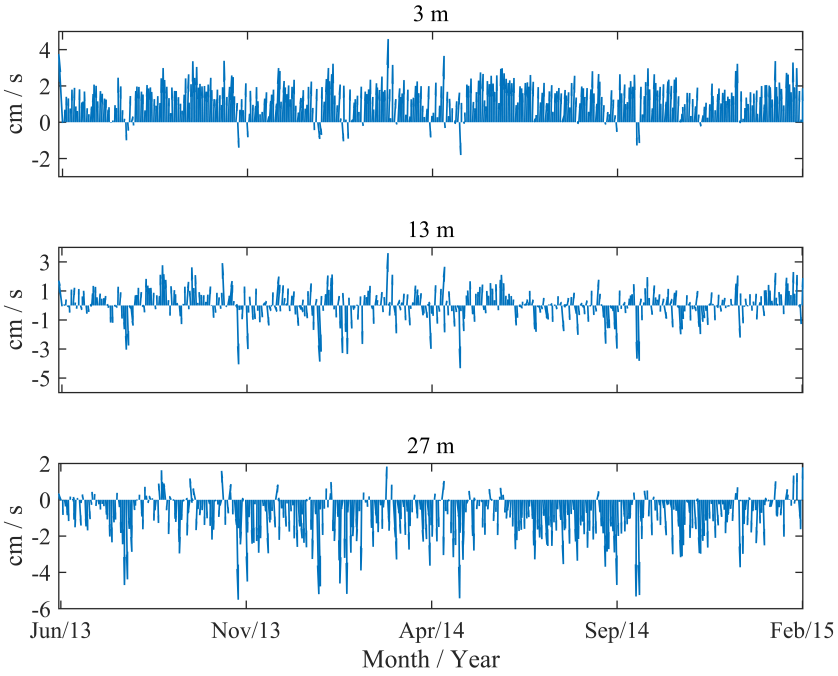

Figure 4.23: 36-hr mean current vectors of **U** measured by the ADCP at 3, 13, and 27 m above the seafloor.

4.3.3 Comparison between $\mathbf{U_r}$ and U

The relative cross flow velocity $\mathbf{U_r}$ estimated from plume bending angles reflects the horizontal currents in the immediate vicinity above the North Tower of Grotto. Despite its proximity to the ADCP ($\sim$ 80 m down south, Figure 4.17), there is significant difference between $\mathbf{U_r}$ and the horizontal current velocity **U** measured by the ADCP. Figure 4.25 shows the correlation coefficient between the directions of $\mathbf{U_r}$ and **U** (combined flow) at 3 to 27 m above the seafloor. The correlation coefficient first increases with height till 11

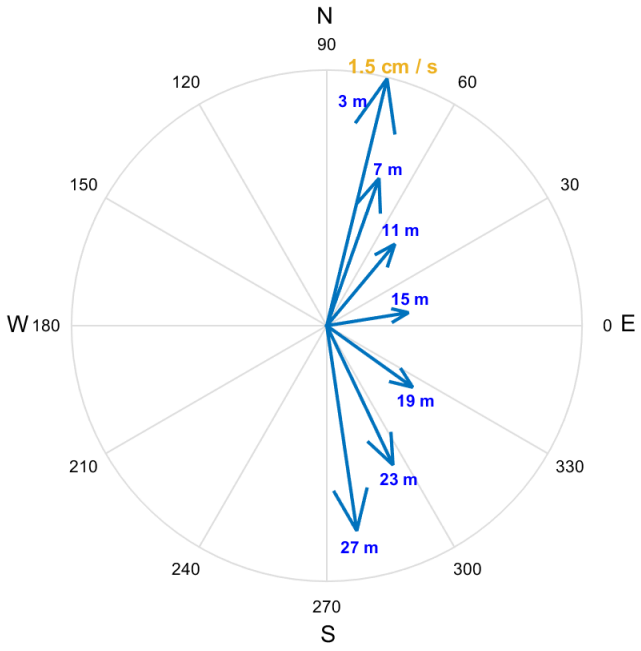

Figure 4.24: Compass plot of the current vectors of **U** averaged over the measurement period from June 2013 to February 2015 at 3 to 27 m above the seafloor in 4 m increments. The height of each current vector and the magnitude of the current vector at 3 m are marked.

m and then decreases with height thereafter. Figure 4.26 shows the correlation coefficient between the magnitudes of $\mathbf{U_r}$ and $\mathbf{U}$ (combined flow) at 3 to 27 m above the seafloor, in which the correlation coefficient decreases monotonically with height. These results suggest the similarity between $\mathbf{U_r}$ and $\mathbf{U}$ decreases with height in general. According to the bathymetric map shown in Figure 4.17, the top of the North Tower is at approximately 13 m above the ADCP and thus $\mathbf{U_r}$ reflects the ambient currents surrounding the North Tower at higher than 13 m above the ADCP. As a result, the decreasing similarity between $\mathbf{U_r}$ and $\mathbf{U}$ with height cannot be explained by their vertical separation. Furthermore, the mean current velocity $\mathbf{U_r}$ is predominantly northward (Figures 4.15 and 4.16), which is in the opposite direction of the mean current velocity of $\mathbf{U}$ at higher than 13 m above the ADCP (Figures 4.23 and 4.24).

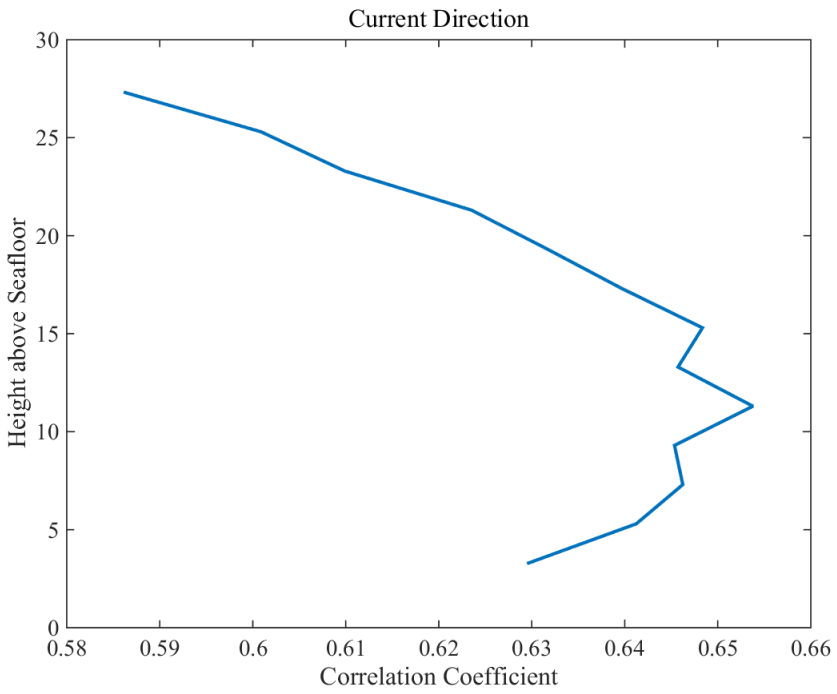

Figure 4.25: Correlation coefficient between the directions of $\mathbf{U_r}$ and $\mathbf{U}$ (combined flow) at 3 to 27 m above the seafloor.

The existence of mean currents in opposite directions within a short horizontal distance ($\sim$ 80 m) and the vertical shear of the mean current velocity of $\mathbf{U}$ are unexpected. One plausible explanation is the southward mean current at higher than 13 m above the ADCP

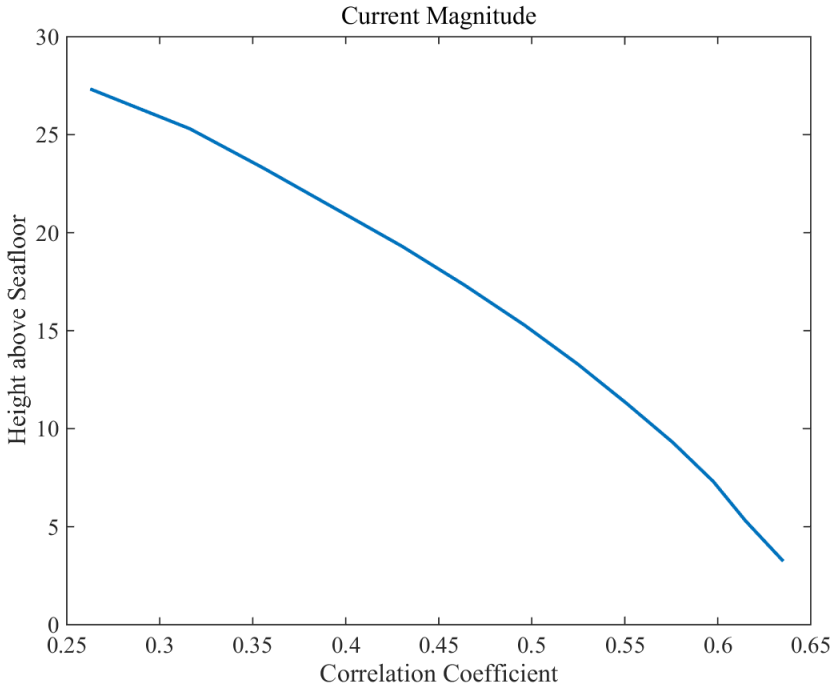

Figure 4.26: Correlation coefficient between the magnitudes of $\mathbf{U_r}$ and $\mathbf{U}$ (combined flow) at 3 to 27 m above the seafloor.

is drawn by the entrainment of the buoyant plumes discharging from the sulfide structure Bastille to the south of the ADCP (Figure 4.17), while the northward mean currents at lower levels above the ADCP and at the North Tower reflect the background northward mean flow in the MEF (Thomson et al., 2003). If true, this explanation would suggest the entrainment flow caused by the buoyant rise of a hydrothermal plume is strong enough to dominate the mean flow structure at almost a hundred meter away from the plume and thus can have a far-reaching impact on the flow structure within the MEF. It would also suggest that the entrainment flows can serve as important pathways for vent-generated chemicals and larvae released in the MEF to get entrained into local buoyant plumes and subsequently transported to hundreds of meters above the seafloor, where the vent-generated chemicals and larvae can escape the confinement of the axial valley and disperse to the abyssal ocean. However, previous observations suggest venting at Bastille is weaker than that at Grotto (Kelley et al., 2012) and the ADCP is slightly closer to Grotto than Bastille (Figure 4.17). Therefore, the entrainment flows of the North Tower plumes are likely to overpower the entrainment flows of the Bastille plumes and result in a northward mean current at higher than 13 m above the ADCP.

Regardless of its causal mechanism, the significant difference between $\mathbf{U_r}$ and $\mathbf{U}$ reflects the complex nature of the flow field within the MEF. One future research objective is to use numerical models to simulate the complex interactions among buoyant plumes, plume entrainment, tidal currents, and background mean flows within the MEF. The simulation results will contribute to a more complete view of the local flow field, which has significant impact on the recruitment of vent larvae and their along-ridge transport to adjacent vent fields.

4.4 Chapter Summary

In this chapter, we present the 41-month time-series measurements of the volume transport, vertical flow rate, and expansion rate of the North Tower plume above Grotto as an extension to the 26-day time series presented in Chapter 3. The 41-month time series of volume transport and vertical flow rate features significant short-term variations but no pronounced global trend, which points to the long-term steadiness of hydrothermal venting at Grotto

during the measurement period. Analysis of the short-term variations in the time series provides further evidence for the finding in Chapter 3 that the ambient ocean currents enhance the rate at which a hydrothermal plume mixes with the ambient seawater. Such current-driven entrainment introduces the oscillations in the ambient currents into the flow field within the plume, which leads to the significant short-term variations of its volume transport, vertical flow rate, and expansion rate.

Additionally, we estimate the ambient currents in the immediate vicinity of the North Tower of Grotto from the plume bending angles observed in 3-D acoustic images. Comparing the estimated ambient currents with those measured by the ADCP deployed 80 m to the southwest of Grotto reveals a surprising discrepancy: the mean flow estimated from the plume bending angles is predominantly northward while the mean flow measured by the ADCP is southward at similar levels. The existence of opposite mean flows within such a short distance ($\sim$ 80 m) reflects the complex nature of the current structure within the vent field, which is a result of the combined effects of plume-induced entrainment flows, background abyssal currents, and their interactions with the bottom topography within the axial valley.

Chapter 5

Time-series Measurement of Hydrothermal heat transport at the Grotto Mound, Endeavour Segment, Juan de Fuca Ridge

This chapter aims to investigate the temporal variations of the heat source driving a hydrothermal plume and its response to geological events. In this chapter, we develop an inverse method of estimating the source heat transport driving the North Tower plume based on the classic plume model developed by Morton et al. (1956). The resultant 41-month (October 2011 to February 2015), high-resolution (sampling rate ~ 1 per day) heat transport time series is an unprecedented look at the temporal variability of a hydrothermal system. Further analysis of this time series sheds light on the response of a hydrothermal system to local seismic events. This chapter is adapted from Xu et al. (2014). Section 5.1 gives an introduction to the inverse method along with its underlying assumptions and uncertainty followed by the field measurements that serve as the ground-truth for the acoustically-obtained heat transport estimates. Section 5.2 discusses the temporal variability of the heat transport driving the North Tower plume and its response to local seismicity in light of both contemporary and historical heat transport and seismic data. Section 5.3 gives concluding remarks.

5.1 Theories and Methods

5.1.1 Derivation of Heat Transport

A hydrothermal plume's source conditions largely dictate its downstream behavior. The source conditions consist of the initial specific transports of volume (Q_0), momentum (M_0)

and buoyancy (B_0)

$$Q_0 = \int_{A_0} W_0 dS,$$
$$M_0 = \int_{A_0} W_0^2 dS,$$
$$B_0 = \int_{A_0} W_0 g(\rho_w - \rho_0)/\rho_{ref} dS. \tag{5.1}$$

Within equation (5.1), W_0 is the exit velocity of the plume; A_0 is the area of the vent orifice; g is the gravitational acceleration; ρ_0, ρ_w, ρ_{ref} are the plume initial density, seawater density, and the reference density. According to Morton (1959), a plume driven by an actual source with finite transports ($Q_0, M_0, B_0 \neq 0$) asymptotically develops into a pure plume that can be considered discharging from a virtual point source of buoyancy only $(0, 0, B_0)$ below the actual source. According to Morton et al. (1956), the behavior of a pure plume in a homogeneous, quiescent environment is described by the conservation equations given in Appendix K (equation K.5). Solving those conservation equations leads to an expression of the plume's volume transport (Q) as

$$Q(B_0, z_i) = \left(\frac{3\pi^2(1+\lambda^2)}{2(5/(6\alpha))^4}\right)^{1/3} B_0^{1/3} z_i^{5/3}. \tag{5.2}$$

Within equation (K.9), α and λ are the plume entrainment coefficient and the concentration-to-velocity width ratio (Morton et al., 1956); z_i is the height of the plume above the virtual point source, which can be determined from the plume's e-folding radius, b_e (the distance in a horizontal plane from the center of the plume to the point where the plume's vertical flow rate decreases to $1/e \sim 37\%$ of the vertical flow rate at the plume's center), as

$$z_i = \frac{5}{6\alpha} b_e. \tag{5.3}$$

In practice, we estimate Q and b_e over 17 equally separated horizontal cross-sections spanning the initial 8 m plume rise (7 to 15 m in 0.5 m increments above the top of the North Tower at 2175 m depth) following the procedures detailed in Section 5.1.2. Substituting b_e into equation (5.3) gives z_i of the corresponding Q estimates. Subsequently, we determine B_0 as the optimal parameter in the least-squares sense by fitting equation (K.9) to Q estimates. Knowing B_0, the initial heat transport (H_0) of the plume is

$$H_0 = \frac{C_p \rho_{ref}}{g\alpha_T} B_0 \tag{5.4}$$

where C_p is the specific heat capacity and α_T is the thermal expansion coefficient.

5.1.2 Estimation of Plume Properties

Ideally, for a hydrothermal plume discharging into slack (no ambient currents and turbulence), clear (no suspended particles) seawater, the volume (Q) and momentum (M) transports at a height z above the vents are estimated by summing the plume's vertical flow rate W (obtained by processing the COVIS Doppler-mode data following the procedures described in Xu et al. (2013) and Section 3.1.1) across an infinite horizontal cross-section of the North Tower plume at the height z:

$$\begin{aligned} Q(z) &= \int_{-\infty}^{\infty}\int_{-\infty}^{\infty} W(x,y,z)dxdy, \\ M(z) &= \int_{-\infty}^{\infty}\int_{-\infty}^{\infty} W^2(z,y,z)dxdy. \end{aligned} \tag{5.5}$$

In practice, W estimates outside the plume are dominated by background noise and oceanic currents. Thus, we restrict W estimates to within the plume by eliminating all estimates corresponding to a backscatter intensity less than a threshold fraction ($s_{thresh} = 2\%$) of the maximum backscatter intensity over the cross-section. Additionally, to ensure a sufficient signal-to-noise ratio, we eliminate W estimates that are less than a threshold fraction ($W_{thresh} = 10\%$) of the maximum W estimated over the cross-section.

Generally speaking, using only the 'good' W estimates that satisfy the above two criteria, especially the second one, to calculate volume and momentum transports underestimates Q and M. This underestimation can be quantified as follows. The restricted transports Q_r and M_r satisfying the second criterion have the forms:

$$\begin{aligned} Q_r(z) &= \int_{W(z,r)>10\%W_c(z)} W(x,y,z)dxdy, \\ M_r(z) &= \int_{W(z,r)>10\%W_c(z)} W^2(x,y,z)dxdy \end{aligned} \tag{5.6}$$

where W_c is the maximum over a plume's cross-section. Assuming W has an axisymmetric Gaussian cross-section

$$W(z,r) = W_c(z)\exp\left(-r^2/b_e^2(z)\right), \tag{5.7}$$

where b_e is the plume e-folding radius and substituting into equation (5.5) to get Q and M in terms of b_e and W_c gives

$$Q(z) = 2\pi \int_0^\infty W_c(z) \exp\left(-\frac{r^2}{b_e^2(z)}\right) r dr = \pi b_e^2(z) W_c(z),$$
$$M(z) = 2\pi \int_0^\infty W_c^2(z) \exp\left(-\frac{2r^2}{b_e^2(z)}\right) r dr = \frac{\pi}{2} b_e^2(z) W_c^2(z). \tag{5.8}$$

Similarly, substituting equation (5.7) into equation (5.6) gives

$$\begin{aligned} Q_r(z) &= 2\pi \int_{W_r(z,r)>10\%W_c(z)} W_r(z,r) r dr \\ &= (0.9)\pi b_e(z)^2 W_c(z), \\ M_r(z) &= 2\pi \int_{W_r(z,r)>10\%W_c(z)} W_r^2(z,r) r dr \\ &= (0.99)\frac{\pi}{2} b_e^2(z) W_c^2(z). \end{aligned} \tag{5.9}$$

Finally, comparing equations (5.9) and (5.8) leads to

$$\begin{aligned} Q(z) &= \frac{1}{0.9} Q_r(z), \\ M(z) &= \frac{1}{0.99} M_r(z). \end{aligned} \tag{5.10}$$

Therefore, we acquire the desired transports Q and M by calculating the restricted transports Q_r and M_r using only 'good' W estimates and multiplying the results by the correction factors $\frac{1}{0.9}$ and $\frac{1}{0.99}$ respectively. Knowing Q and M, according to equation (5.8), we calculate the plume e-folding radius b_e as

$$b_e(z) = \frac{Q(z)}{\sqrt{2\pi M(z)}}. \tag{5.11}$$

Substituting b_e into equation (5.3) gives the height of the plume above the virtual point source, z_i, needed for the heat transport derivation described in Section 5.1.1. Table 5.1 defines the mathematical symbols used and gives default values of constant parameters in this chapter.

5.1.3 Justification of Simple-plume Formula

Equation (K.9) is valid for an individual buoyancy-driven plume discharging into a homogeneous, calm environment. The North Tower plume, however, is an integrated plume formed

Table 5.1: Symbols and Default Values of Constant Parameters

Symbol	Description	Value
α	entrainment coefficient	0.1
α_T	thermal expansion coefficient (low temperature)	$1.32 \times 10^{-4}\,^{\circ}\mathrm{C}^{-1}$
α_h	thermal expansion coefficient (high temperature)	
A	cross-sectional area of the plume	
A_0	orifice area	
B	buoyancy transport	
B_0	initial buoyancy transport	
b_{sv}	e-folding radius of Gaussian backscatter intensity cross-sectional profile	
b_e	e-folding radius of Gaussian velocity cross-sectional profile	
C_p	specific heat capacity of the plume	$3.92 \times 10^3\,\mathrm{J/kg/^{\circ}C}$
g	gravitational acceleration	$9.8\,\mathrm{m/s^2}$
H_0	initial heat transport	
M	momentum transport	
M_0	initial momentum transport	
Q	volume transport	
Q_0	initial volume transport	
r	radial distance of a point from the plume's central point over a cross-section	
T	temperature of the vent effluent at the orifice	
W	plume vertical flow rate	
W_c	peak vertical flow rate over a cross-section	
W_0	plume exit vertical flow rate	
W_{thresh}	vertical flow rate threshold	$0.1W_c$
x_0	x-coordinate of the plume's central points	
y_0	y-coordinate of the plume's central points	
z	height above the vents	
z_i	height above the virtual source	
ρ	plume density	
ρ_0	plume initial density	
ρ_w	seawater density	
ρ_{ref}	reference density	$1037\,\mathrm{kg/m^3}$
λ	concentration-to-velocity width ratio	1.06
s_{thresh}	volume backscattering coefficient threshold	0.02

by multiple merging plumes discharging into an oceanic environment with stratification and cross-flows. The next three paragraphs consider the implications of merging, cross-flows, and stratification respectively.

According to Figure 5.1, the plume's volume transport (Q) and e-folding radius (b_e) profiles approach those of a single buoyancy-driven plume at 7 m above the North Tower (Ocean Networks Canada Data Archive, 2015b). This suggests the individual plumes coalesce and behave like a single plume beyond that level. Therefore, restricting the Q and b_e estimations to a vertical range of $7 \leq z \leq 15$ m above the North Tower effectively eliminates the effect of plume merging. Furthermore, we quantify the 'closeness' of the estimated Q and b_e profiles to the ideal ones by calculating the Root-Mean-Square (RMS) errors of the least-squares fits. We then eliminate Q and b_e profiles with RMS errors larger than 20% and 2% of the corresponding profile means respectively.

The oceanic currents within the axial valley near MEF are characterized by tidal oscillations with an amplitude ~ 5 cm/s superimposed on a northward mean flow at $1 - 5$ cm/s (Thomson et al., 2003) (Section 4.3). Such ambient cross-flows bend the North Tower plume during its buoyant rise. To minimize the effect of the ambient cross-flows, we restrict the heat transport derivation to the moments when the inclination angle Θ of the plume's centerline (Figure 4.8) is less than 10°, such as the plume shown in Figure 2.1.

The background hydrography at Endeavour was measured in Sept 2007 in several Conductivity Temperature Depth (CTD) surveys. The hydrography measured outside the axial valley showed linear stratification with the buoyancy frequency $N = 1.11 \times 10^{-3}\,\mathrm{s}^{-1}$ (Xu and Di Iorio, 2012). The hydrography measured inside the axial valley close to Grotto was non-linear with reduced stratification in the initial 225 m above the bottom (Lavelle et al., 2013). According to Turner and Campbell (1987), the rise height of a buoyancy-driven plume (the height where the plume reaches neutral buoyancy and spreads laterally) is

$$Z_{max} = 3.8 B_0^{1/4} N^{-3/4}. \tag{5.12}$$

Assuming the initial heat transport of the North Tower plume $H_0 = 18$ MW and substituting into equation (5.4) gives $B_0 = \frac{g\alpha_t}{C_p \rho_{ref}} H_0 = 0.0057\,\mathrm{m}^4/\mathrm{s}^3$. Plugging B_0 and N into equation (5.12) gives $Z_{max} \sim 172$ m. Note that applying the nonlinear hydrography measured inside

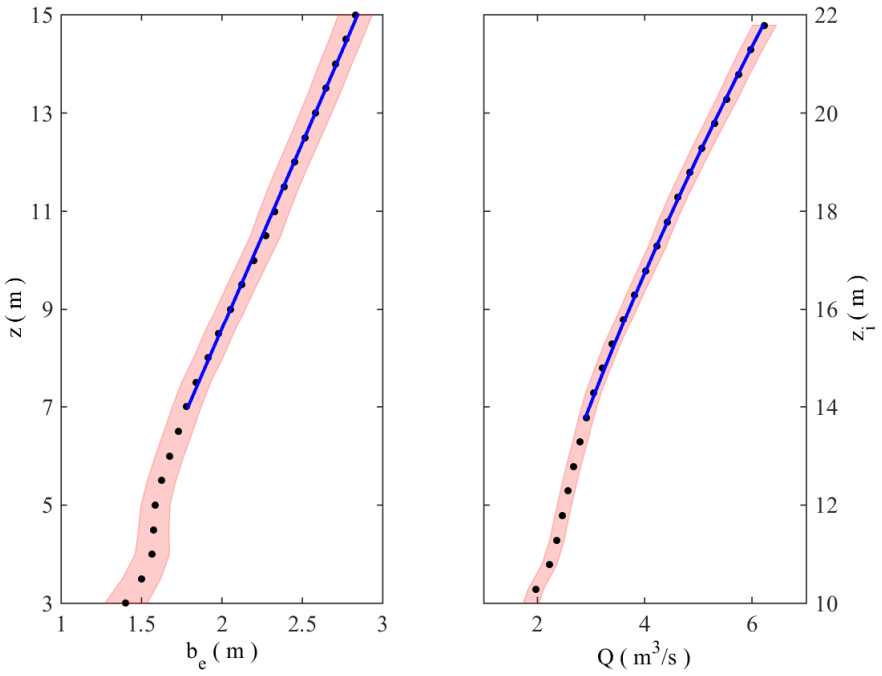

Figure 5.1: E-folding radius (b_e, left) and volume transport (Q, right) profiles of the North Tower Plume. Both profiles (black dots) are averaged over a 26-month measurement period (October 2011 to November 2013) when the plume's bending angle is smaller than 10 degree from the vertical direction (Ocean Networks Canada Data Archive, 2015b). The left y-axes are the height above the North Tower (z), and the right y-axes are the height above the virtual source (z_i). The blue lines are the theoretical profiles ($b_e = p_1 z_i$; $Q = p_2 z_i^{5/3}$, where $z_i = \frac{5}{6\alpha} b_e$ and p_1 and p_2 are the least-square fit parameters) expected for a single buoyancy-driven plume. The red shades delimits the uncertainty caused by the imprecision in the vertical flow rate estimates (the first error source mentioned in Section 5.1.4). This figure is modified from Figure 4 in Xu et al. (2014).

the axial valley instead will result in a larger Z_{max} due to the reduced stratification. Since Z_{max} is much larger than the vertical range $7 \leq z \leq 15$ m of interest, the effect of ambient stratification on our heat transport measurements is negligible.

5.1.4 Uncertainty Quantification

The overall uncertainty in the heat transport estimate, H_0, stems from three error sources. The first error source is due to the imprecision of the plume vertical flow rate estimation, W_{err}. A major contributor to this error source is the turbulence in the plume. In practice, W_{err} is quantified using the method described in Xu et al. (2013). Propagating W_{err} through equations (5.8) to (5.11) following the rules described in Taylor (1982) gives the resultant uncertainties in Q and b_e as $\sim 4\%$ of their mean values (Figure 5.1). The second error source stems from the uncertainties in the applied constant parameters (Table 5.1). Among those parameters, the entrainment coefficient, α, and concentration-to-width ratio, λ, are the least constrained and dominate the error source. Previous laboratory measurements of α for a buoyancy-driven plume vary from 0.08 to 0.120 (Table 2 in Carazzo et al. (2006)), of which the mean 0.1 is used as the default value in the heat transport derivation. For a buoyancy-driven plume, previous studies reported λ values ranging from 0.92 to 1.2 (Table 3 in Wang and Law (2002)), of which the mean 1.06 is taken as the default value. According to Carazzo et al. (2006), the variations in the laboratory measurements of α and λ suggest both parameters, rather than being universal constants, vary as functions of the cross-sectional profiles of the velocity, buoyancy, and turbulent stress within a plume. Such variability will in turn cause random fluctuations in the heat transport estimated based on constant α and λ values. The third error source stems from the bias introduced by using arbitrary thresholds s_{thresh} and W_{thresh} when calculating the volume and momentum transports (Section 5.1.2).

We quantify the random error stemming from the first two sources using the Monte Carlo simulation detailed in Appendix L. The result suggests a magnitude of random error from the two sources combined of $H_{err} = 3.18$ MW. To quantify the bias introduced by the third source, we allow the arbitrary thresholds to vary: $1.5\% \leq s_{thresh} \leq 5\%$; $0 \leq W_{thresh} \leq 20\%$. The mean values of H_0 averaged over a 6-month period (January 1st - June 30th 2012) are calculated using 16 combinations of different values of s_{thresh} and W_{thresh} (Table 5.2). The

mean values of H_0 vary from 16.32 to 20.36 MW and the bias is taken as half of this range as $H_{bias} = 2.02$ MW.

Table 5.2: Mean Values of the Heat Transport Driving the North Tower Plume (MW) Averaged over a 6-month Period (January to June 2012) Corresponding to Different Combinations of the Thresholds s_{thresh} and W_{thresh}.

W_{thresh} (%) \ s_{thresh} (%)	1.5	2.1	3.5	5.0
0	20.36	17.97	17.55	17.23
6.7	19.52	17.42	17.19	16.82
13.3	19.23	17.17	16.61	16.32
20.0	19.19	17.08	16.65	16.36

5.1.5 In-situ Heat Transport Estimation

In order to verify the acoustically derived heat transport described above, we obtained an independent heat transport estimate by conducting in-situ temperature measurements within the North Tower plume following the method described by Rona et al. (1993). The underlying formula of this method is (Bemis et al., 1993)

$$T_c(z + z_0) = \frac{b}{(\alpha_T g)^{1/3}(\rho_{ref} C_p)^{2/3}} H_0^{2/3}(z + z_0)^{-5/3} \tag{5.13}$$

where T_c is the mean temperature anomaly at the plume centerline relative to ambient seawater, z is the height above the vents, z_0 is the distance of the virtual point source below the vent orifices, and $b = 14.29$ is an empirically determined constant (Papanicolaou and List, 1988). Similar to the acoustic heat transport estimation, we determine H_0 and z_0 by a least-squares fit of equation (5.13) to T_c estimated at varying levels in the plume.

The in-situ temperature measurements needed to estimate T_c were conducted on June 19, 2012 using the Conductivity-Temperature-Depth instrument (CTD) mounted on the Remotely Operated Vehicle (ROV) *ROPOS*. We obtained a total of 10 vertical profiles of plume temperature samples. During each profile, the ROV first entered the North Tower plume at approximately 5 m above the vents and adjusted its position within the plume until the real-time temperature reading from the CTD reached a maximum—an indicator that the CTD was at or close to the plume centerline. The ROV then slowly ascended to

25 m above the vents and descended back to the starting level in the same manner while maintaining its horizontal position.

We group the temperature samples over the 10 profiles into 0.6-m vertical bins. We then use the maximum and minimum samples within each bin as proxies of the mean plume centerline and ambient seawater temperatures at the central level of that bin. The difference between the two is thus an estimate of T_c at that level of the plume. Subsequently, we perform non-linear least-squares fitting of equation (5.13) to T_c estimates applying the Gauss-Newton method and determine H_0 and z_0 as the iterative best-fit parameters. The result is shown in Figures 5.2 and 5.3(a). The resulting heat transport estimate is $H_0 = 26.72$ MW with a 95% confidence interval (CI) of (20.86; 33.05 MW). The acoustic heat transport estimate averaged over 3 days before and after the in-situ estimate is 21.09 MW, which is within the 95% CI of the in-situ estimate.

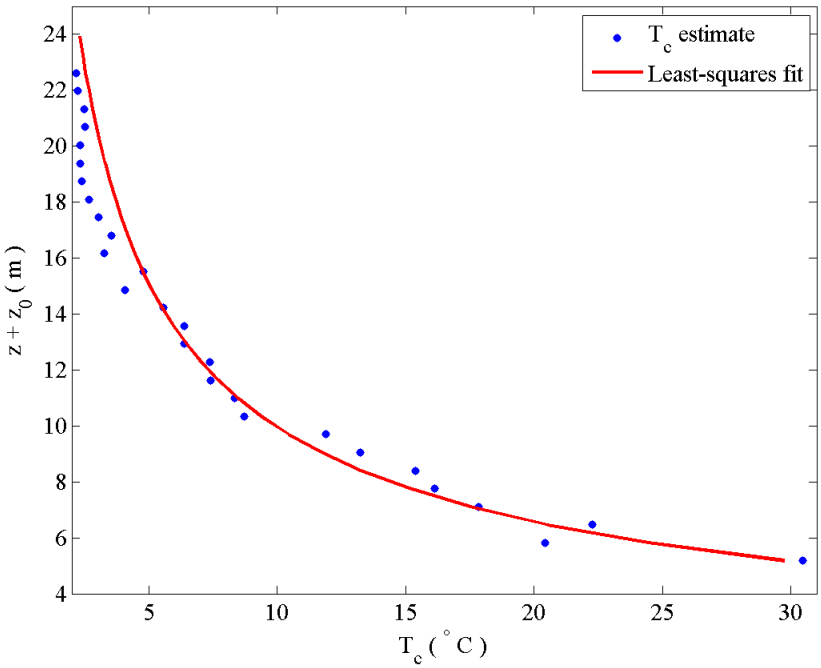

Figure 5.2: Plume centerline temperature anomaly T_c estimated from the in-situ temperature measurements conducted on June 19th, 2012 (blue dots) and the least-squares fit of equation (5.13) calculated using the Gauss-Newton method (red line). The heat transport determined as the best-fit parameter is $H_0 = 26.72$ MW with the 95% confidence interval of (20.86; 33.05 MW). This figure is reproduced from Figure 5 in Xu et al. (2014).

5.2 Results and Discussion

5.2.1 Heat Transport Time Series

Figure 5.3 (a) shows a 41-month (October 2011 to February 2015) time series of the heat transport driving the North Tower Plume obtained using the default values of the constant parameters listed in Table 5.1. The average sampling rate of this time series is 1.22 sample/day. There is considerable variability in the time series with the standard deviation $H_{std} = 6.46$ MW being approximately 37% of the mean $H_m = 17.58$ MW. Note that the estimation error, H_{err}, obtained in Section 3.1.4 is approximately 50% of H_{std}. This suggests half of the temporal variability may be caused by the random error from the first two sources described in Section 3.1.4. Figure 5.3(c) shows the power spectrum of the time series, which has a near-white distribution with no peaks beyond the 5% significance level, which corresponds to a relative magnitude of heat transport oscillation being approximately 6% of H_m. In addition, there is a slightly decreasing trend in the time series corresponding to a linear regression slope of -0.73 MW/year with the 95% confidence interval from -1.06 to -0.37 MW/year. Another interesting feature in the heat transport time series is the two dips in October 2014 and January 2015 (marked by the downward arrows in Figure 5.3(a)). The mean heat transport over those two months is approximately 11 MW, which is 63% of H_m.

In order to reduce the random noise, we smooth the heat transport time series in Figure 5.3(a) using a moving-average filter (Figure 5.3(b)). The period of the averaging window is 30 days, and the window is moved from left to right along the time axis in 1 day increments. The red shade marks the 95% CI of the smoothed time series. Note that the reduced heat transport in October 2014 and January 2015 is more pronounced in the smoothed time series.

5.2.2 Hydrothermal Response to Geological Events: a Case Study at Grotto

Direct links between hydrothermal discharge and geological events such as submarine volcanic eruptions, non-eruptive dike intrusions, and earthquakes of magmatic or tectonic origin have been observed in many cases. Examples of eruptive events include the four

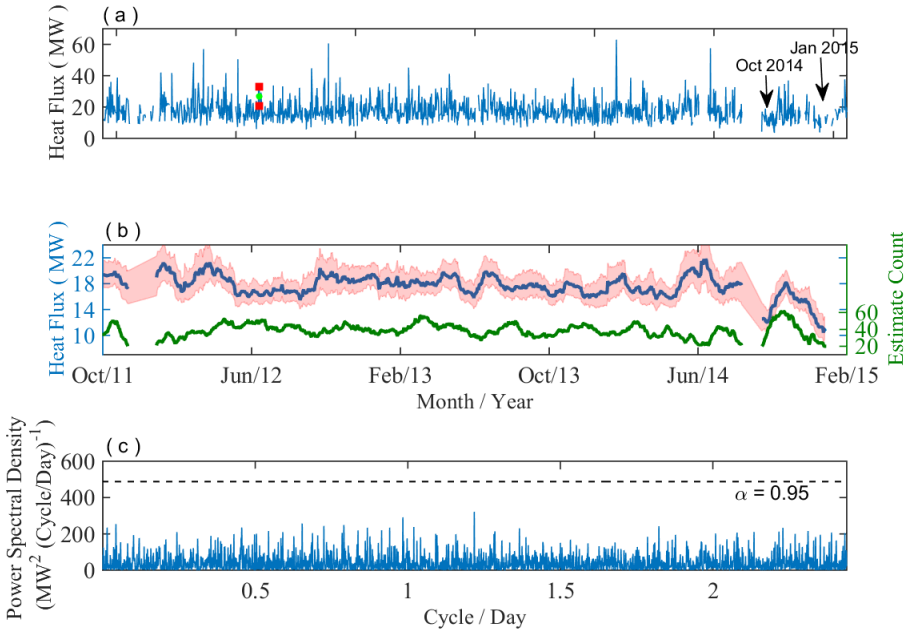

Figure 5.3: (a) 41-month (October 2011 to February 2015) time series of the heat transport driving the North Tower plume obtained using the default values of the constant parameters listed in Table 5.1. The green dot marks the in-situ heat transport estimate described in Section 5.1.5. The red blocks delimit the 95% confidence interval (CI) of the in-situ estimate. (b) The blue line is the 30-day moving average of the time series in (a). The red shade marks the 95% CI of the moving-averaged time series. The green line shows the number of heat transport estimates within the moving window corresponding to each average. An average is replaced with NaN if there are fewer than 20 estimates in the moving window. (c) Power spectral density of the heat transport time series in (a). The dashed line marks the 5% significance level. Note that because the heat transport time series shown in (a) is unevenly spaced, the time series does not have a well-defined Nyquist frequency. According to (Eyer and Bartholdi, 1999), the equivalent Nyquist frequency of an unevenly spaced time series $\geq 1/2\delta t$, where δt is the smallest time interval. For the heat transport time series, $\delta t \sim 1/8$ day and the equivalent Nyquist frequency ≥ 4 cycle/day, which is sufficient for detection of the major semi-diurnal and diurnal tidal oscillations without aliasing effects. This figure is modified from Figure 6 in Xu et al. (2014).

seafloor eruptions detected on the Juan de Fuca Ridge at the Cleft Segment in 1986 (Baker et al., 1987), at the Coaxial Segment in 1993 (Baker et al., 1998), and at Axial Seamount in 1998 and 2011 (Baker et al., 1999; Chadwick et al., 2013) (readers are referred to Baker et al. (2012) for a summary of historical magmatic events). All four events have had profound impacts on local hydrothermal systems in terms of generating transient cataclysmic hydrothermal discharges—event plumes, changing the venting temperature and chemical concentrations of preexisting hydrothermal systems, reactivating extinct hydrothermal structures, and initiating new chronic hydrothermal venting. Examples of non-eruptive events include the earthquake swarms that occurred on the East Pacifict Rise at 9-10 $^{\circ}N$ in 1995 (Sohn et al., 1998) and on the Endeavour Segment in 1999-2000 (Johnson et al., 2000; Lilley et al., 2003; Bohnenstiehl et al., 2004). Both events caused significant changes in temperatures and chemical concentrations of local hydrothermal effluents.

The seismic activity at the Endeavour Segment has been closely monitored since 1991 when the data recorded by the US Navy's Sound Surveillance System (SOSUS) became accessible to civilian research groups. The SOSUS record discontinued in 2008 after several key elements of the system went offline. In addition to the SOSUS system, a local OBS network named Keck was deployed along the central Endeavour Segment from 2003 to 2006 to monitor local microearthquakes with high spatial resolution. By analyzing the local microearthquakes detected by the Keck network, Wilcock et al. (2009) and Kellogg (2011) found a positive spatial correlation between the rate of seismicity beneath the vent fields and their hydrothermal heat transports. In 2010, two short-period OBSs, KEMF and NCHR, were deployed and connected to the NEPTUNE observatory at Endeavour. NCHR was disconnected in July 2012, which left KEMF as the only working seismometer at Endeavour since then. The data recorded by SOSUS and Keck feature continuous seismic activity dominated by 4 large earthquake swarms in June 1999, January 2000, January and February 2005. Weekly et al. (2013) hypothesized that these four earthquake swarms are results of a 6-year non-eruptive event which started with the 1999 swarm and ended with the 2005 swarms. After the 2005 swarms, the rate of seismicity at Endeavour decreased dramatically and the segment has entered a quiescent period. This is demonstrated by the comparison between the daily earthquake-count time series recorded by the Keck network

and OBS KEMF shown in Figure 5.4.

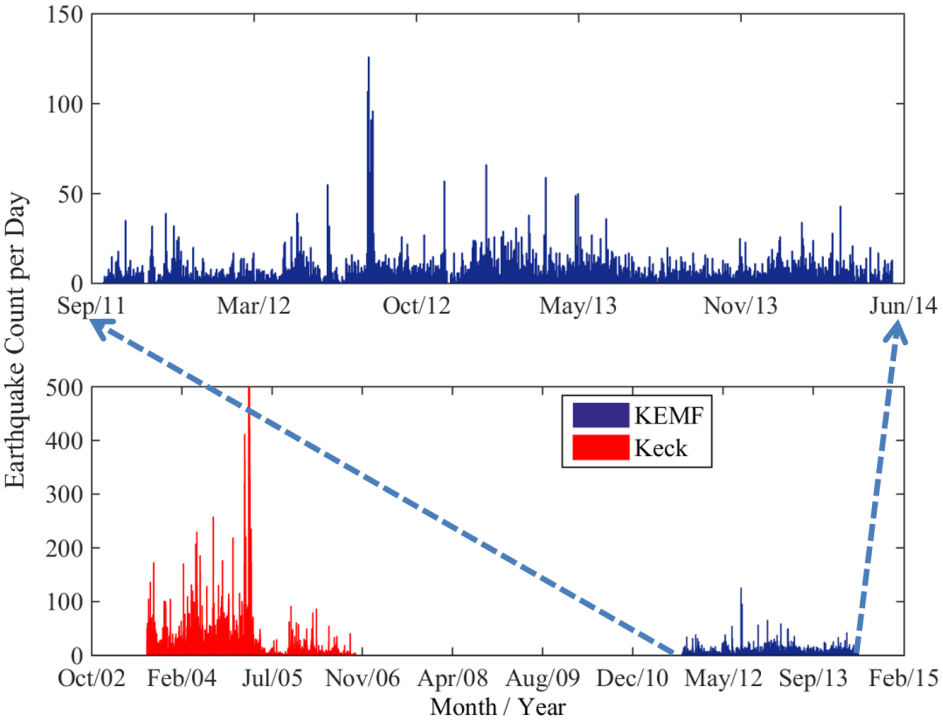

Figure 5.4: (a) Daily event-count time series of the earthquakes detected from the seismic data recorded by OBS KEMF from Sept 2011 to May 2014. The earthquakes were detected using the automatic algorithm described in the supporting documents of (Weekly et al., 2013). (b) Comparison of the daily earthquake-count time series in (a) (blue) with the daily earthquake-count time series recorded by the Keck network from August 2003 to October 2006 (red) (Weekly et al., 2013). This figure is modified from Figure 7 in Xu et al. (2014).

Compared with the almost continuous seismic data at Endeavour over the past two decades, contemporaneous observations of hydrothermal activities are far scarcer. Estimates of heat transport from the Grotto Mound have been reported in several previous studies. Bemis et al. (1993) acquired the first estimate of heat transport from the North Tower at 15.8 MW in 1988, based on temperature and flow rate observations within the plume above the North Tower, and estimated the error range from 4.7 MW to 40.4 MW depending on calculation assumptions. In 2000, observations of effluent temperature and flow rate along with orifice diameter at 5 black smoker vents on the North Tower imply a total heat transport of 56 ± 15 MW, much larger than the 1988 estimate (Rona et al., 2006). In the same year, the hydrographic survey using the AUV ABE (section 1.2.2) measured the

combined heat transport from Grotto and Lobo (a sulfide mound to the north of Grotto) as 101 ± 40 MW. In 2004, a similar hydrographic survey using ABE found the combined heat transport decreased by $> 50\%$ to 45 ± 8 MW (table 2.4 in Kellogg (2011)). More recently during several submersible dives in Aug 2008 and Jul 2010, a total of 6 point measurements of the effluent temperature, flow rate, and vent orifices at black smoker vents on the elliptical edifice of Grotto yielded a mean heat transport estimate ~ 1.6 MW/vent with a standard deviation ~ 1.5 MW/vent (L. Germanovich, personal communication). Using this estimate as a proxy for the average heat transport of the five black smoker vents driving the North Tower plume would give a total heat transport from the focused sources on the North Tower as 8 ± 7.5 MW.

The heat transport time series shown in Figure 5.3(a) suggests the heat source driving the North Tower plume remained relatively steady over the 41-month time period. The mean heat transport estimated from the 26-day dataset collected in October 2010 before the power-off of the NEPTUNE observatory at MEF (not shown in Figure 5.3) (Figure 3.4 in Chapter 3, Xu et al. (2013)) is 19.3 MW with a 95% CI of (17.1; 21.7 MW), which is not significantly different from the mean value, $H_m = 17.6$ MW, of the time series over the 41-month period. This indicates the stability of the heat transport may date back to October 2010. Compared with the previous heat transport measurements at Grotto summarized in the preceding paragraph, with the exception of the 2000 data, the 1988 and 2008-2010 estimates can be taken to imply a heat transport in the vicinity of $10 - 20$ MW, which is consistent with the observed range of COVIS estimates over 2010 to 2015. One plausible hypothesis is that the North Tower of Grotto has remained at a similar level of heat transport since 1988 with the exception of a short period of increased transport after the 1999-2000 earthquake swarms (Kelley et al., 2012; Bohnenstiehl et al., 2004) (Figure 5.5). The remarkably steady heat transport may imply the hydrothermal venting at Grotto is fueled by a steady heat source through a robust pluming system that needs a strong geological event to perturb. Previous studies suggest the venting temperature and salinity at several sulfide structures in the MEF had remained relatively steady before the large perturbation caused by the 1999-2000 earthquake swarms (Singh et al., 2013). In addition, the magnetic field data presented in Tivey and Johnson (2002) suggest the

venting from Grotto and other major sulfide structures in the MEF are fed from pipe-like up-flow zones armored by silica deposition in the uppermost crust. The presence of a silica shell likely strengthens the overall integrity of the up-flow zone below Grotto and make it immune to the small perturbations caused by weak seismic activity. The higher than usual heat transport from the North Tower is consistent with the observations of the significant increases in the temperature and volatile concentrations of hydrothermal effluents triggered by the 1999 earthquake swarm (Johnson et al., 2000; Lilley et al., 2003; Seyfried et al., 2003). The higher heat transport in 2000 is also consistent with the ABE data that suggest both the total heat transport from the MEF and the combined heat transport from Grotto and Lobo decreased by $> 50\%$ between 2000 and 2004. Similar to the 1999 earthquake swarm, the 2005 swarms also triggered transient temperature perturbations at two black smoker vents in the MEF (Hooft et al., 2010). Although a 'Rapid Response' cruise found no significant increase in water column heat content above all Endeavour vent fields 8-11 days following the 2005 swarms (Dziak et al., 1996), it is uncertain if the heat transport from the North Tower also remained unchanged due to the lack of heat transport measurement right after the event. In addition, the steady heat transport from the North Tower measured by COVIS from 2011 to 2014 coincides with the reduced rate of seismicity at Endeavour (Figure 5.4). In general, the evolution of the heat transport from the North Tower since 1988 correlates with the rate of local seismicity with a short episode of increased heat transport following pronounced seismic activities and reduced steady heat transport during time periods of quiescent seismicity. Such temporal correlation combined with the spatial correlation observed by Wilcock et al. (2009) and Kellogg (2011) suggest a close interconnection between hydrothermal and seismic activities at Endeavour.

5.2.3 Short Term Variability of Hydrothermal Activity at Grotto

Despite having no global trend, the heat transport time series shown in Figure 5.3(a) has considerable short term variations. Although the estimation uncertainty could be a significant component in the short-term variability of the heat transport, part of the variability may reflect natural oscillations of the hydrothermal circulation within the Grotto mound. Such natural oscillations lead to the fluctuations in the effluent temperature time series

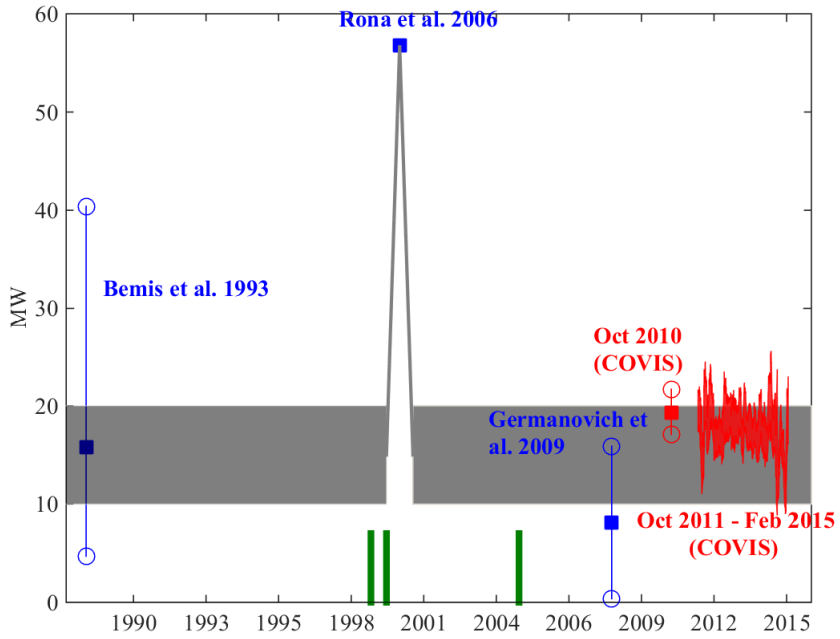

Figure 5.5: heat transport estimates at the North Tower of Grotto and a conceptual model of the long term heat transport variation. The blue squares (from left to right) mark the best estimates of Bemis et al. (1993) and Rona et al. (2006) and the mean values of the estimates of Germanovich et al. (2009) respectively with the corresponding error ranges delimited by the blue circles. The red square marks the mean value of the heat transport estimated by processing the October 2010 COVIS data; the red circles delimit the corresponding 95% confidence intervals (CI). The red shade is the 95% CI of the moving-averaged heat transport time series in Figure 5.3(b). The gray shade and line represent the conceptual model in which the North Tower has remained at a similar level of heat transport ($10 - 20$ MW) since 1988 with the exception of a short period of increased heat transport after the 1999-2000 earthquake swarms. The red bars on the bottom mark the earthquake swarms that happened at Endeavour (from left to right) in Jun 1999, January 2000, and January-February 2005. This figure is modified from Figure 8 in Xu et al. (2014).

recorded by BARS at a vent located on the elliptical edifice of Grotto. Assuming the temperatures of the black smoker vents driving the North Tower plume vary like the vent monitored by BARS, the magnitudes of corresponding plume heat transport variations can be estimated in three different ways discussed below.

First, the effluent temperature, T, measured by BARS inside the orifice of a black smoker vent on the elliptical edifice of Grotto varied from 329.3 °C to 337.4 °C with a mean value of 332.5 °C over a 13 month period from October 2010 to February 2014 (not including two hiatuses: Nov 2010 to Sept 2011 due to the power-off of the NEPTUNE observatory and February 2012 to June 2013 caused by the melting of the BARS cable) (M. Lilley, personal communication, 2014, Ocean Networks Canada Data Archive (2014)). The heat transport of the vent can be expressed as

$$H_0 = \rho C_p Q_0 (T - T_{bot}) \tag{5.14}$$

where $T_{bot} = 2\,^{\circ}\mathrm{C}$ is the temperature of the background bottom seawater. We calculate the temperature-dependent specific heat capacity, $C_p(T)$, and density, $\rho(T)$, of the vent effluent using the empirical equation of state developed by Bischoff and Rosenbauer (1985) based on BARS temperature measurements at a pressure of 220 bars. Assuming the initial volume transport, Q_0, is constant, substituting the varying T measured by BARS into equation (5.14) gives the relative half range of the variations of H_0 as 2.4% of its mean.

Second, the assumption underlying the above calculation that Q_0 remains constant for varying T may not be valid. According to Wilcock (2004), for black smoker vents, an increase in Q_0 may lead to an increase in T due to the reduced conductive cooling during the hydrothermal fluid's rise from the subsurface reaction zone to the seafloor. Based on the same rationale, a decrease in Q_0 can lead to a decrease in T. Assuming the rate of conductive heat loss through the walls bounding the upwelling hydrothermal fluid is constant, the approximate relation between Q_0 and T can be expressed as

$$\frac{Q_0}{Q_{ref}} = \frac{T_b - T_{ref}}{T_b - T} \tag{5.15}$$

where Q_{ref} and T_{ref} are the reference initial volume transport and temperature of vent effluent, T_b is the temperature of the hydrothermal fluid at the subsurface reaction zone.

We take the mean value of BARS temperature measurements as T_{ref}. Assuming T_b = 400 °C (Jupp and Schultz, 2004) and evaluating equation (5.15) at varying T gives the corresponding temperature-dependent initial volume transport $Q_0(T)$. Substituting $Q_0(T)$ along with the corresponding T into equation (5.14) gives the relative half range of variations in H_0 as 8.7% of its mean.

Third, changes in T can not only result from but also lead to changes in Q_0. Assuming the hydrothermal circulation fed to the Grotto mound follows Darcy's law as viscous flows through a porous medium, Q_0 can be expressed as

$$Q_0 = (k/\mu)A_0\frac{\partial P}{\partial z}, \tag{5.16}$$

where k is the crustal permeability, A_0 is the area of vent orifice, μ is the dynamic viscosity of the hydrothermal fluid, and $\partial P/\partial z$ is the vertical pressure gradient driving the circulation. According to Germanovich et al. (2000), μ can be estimated as

$$\mu(T) = \frac{C_1}{T + C_2} \tag{5.17}$$

where $C_1 = 0.032\,\mathrm{Pa}\cdot\mathrm{s}\,^\circ\mathrm{C}$ and $C_2 = 15.4\,^\circ\mathrm{C}$. We assume the pressure gradient is a result of the hydrostatic pressure difference due to the density contrast, $\delta\rho$, between the heated hydrothermal fluid and background bottom seawater, which leads to

$$\frac{\partial P}{\partial z} = \delta\rho g = g\rho_{ref}\alpha_h(T - T_{bot}) \tag{5.18}$$

where α_h is the thermal expansion coefficient of the heated hydrothermal fluid. Substituting equations (5.17) and (5.18) into equation (5.16) gives

$$Q_0 = \frac{k(T + C_2)}{C1}A_0 g\rho_{ref}\alpha_h(T - T_{bot}). \tag{5.19}$$

Since the range of temperature variations observed in BARS temperature record is only 8 °C, we assume $alpha_h$ to be a constant. Additionally, previous studies suggest pronounced geological events can cause significant changes in k (Ramondenc et al., 2008); since the contemporaneous seismic record shown in Figure 5.4 is devoid of large events, we assume k to be a constant. Subsequently, evaluating equation (5.16) at the varying T measured by BARS gives the temperature-dependent $Q_0(T)$. Substituting along with the corresponding

T into equation (5.14) gives the relative half range of the variations in H_0 as 4.9% of its mean.

Significant tidal oscillations in the diurnal ($\sim$ 1 cycle/day) and semi-diurnal ($\sim$ 2 cycle/day) frequency bands are observed in the BARS temperature time series. Their existence can be attributed to the tidal loading effects described in Crone and Wilcock (2005). To investigate the potential influence of the tidal loading effects on plume heat transport, we extract the tidal oscillations from the BARS temperature time series using the harmonic analysis program T-Tide (Pawlowicz et al., 2002). The corresponding magnitudes of the diurnal and semi-diurnal oscillations are 0.04 °C and 0.11 °C respectively. Following the aforementioned calculations in the preceding paragraphs of this section, the maximum magnitude of the resulting tidal oscillations in the plume heat transport is less than 1% of the mean value, which is much less than the relative magnitude of heat transport variations ($\sim$ 6%, Section 5.2.1) corresponding to the 5% significance level in the power spectrum shown in Figure 5.3(c).

The calculations above suggest, if the temperatures of the black smoker vents driving the North Tower Plume vary like the vent sampled by BARS, the corresponding heat transport variations would be up to 8.7% of the mean value, which is less than a quarter of the standard deviation, $H_{std} \sim 37\% H_m$, of the heat transport time series shown in Figure 5.3(a) and less than a half of the estimation error, $H_{err} \sim 18\% H_m$. This suggests the heat transport variations inferred from BARS temperature measurements cannot fully explain the variations observed in Figure 5.3(a) and are likely obscured by the uncertainty in the acoustic heat transport estimates.

During a submersible survey in June 2013, we observed 4 to 5 black smoker vents located within a crown-shaped sulfide structure on the top of the North Tower, while diffuse flow discharge covered almost the entire top surface. According to Bemis and Rona (2006), such a crown-shaped structure can facilitate the entrainment of proximal diffuse flow effluents into the black smoker plumes; therefore, the heat entrained from diffuse sources could be a significant contributor to the heat transport driving the North Tower plume. The entrainment of ambient fluid into a buoyancy-driven plume is a function of the plume's flow rate, entrainment coefficient, and ambient flow field. All of these factors are likely to vary

on time scales of hours or less (Rona et al., 2006; Xu and Di Iorio, 2012). Therefore, the amount of diffuse flow entrained into the North Tower plume is likely to vary on short time scales, causing the total heat transport driving the plume to vary at the same pace. Such variability is likely an important component in the short term variations observed in the heat transport time series shown in Figure 5.3.

5.3 Chapter Summary

Continuous time-series observations are needed for studying the dynamic nature of seafloor hydrothermal systems. The 41-month hydrothermal heat transport time series presented in this paper provides key information on the temporal evolution of the heat source driving the hydrothermal plume at the Grotto mound on the Endeavour Segment of the Juan de Fuca Ridge. We observe considerable short-term variation but no global trend in the heat transport time series, which suggests the hydrothermal heat output from Grotto may have remained remarkably steady over a three year time period marked by reduced rate of local seismicity. Moreover, the comparison of the current heat transport time series with historical measurements extends the period of steady heat transport from Grotto back to 1988 barring a brief period of increased transport in 2000 potentially triggered by the 1999-2000 earthquake swarms. Such long term steadiness of heat transport points to the robustness of heat source and pluming structure underlying Grotto. Although the estimation error could be a significant contributor to the short-term variability of the heat transport estimate, part of the variations may reflect the natural oscillations of the subsurface hydrothermal circulation and more importantly, the variations of the entrainment of diffuse flow into the proximal black smoker plumes. The successful acquisition of the long-term time series of hydrothermal heat transport using COVIS proved the robustness and effectiveness of using moored instruments installed in underwater observatories to monitor hydrothermal activities. In particular, by treating a future seismic event as a natural perturbation experiment, detailed study of COVIS heat transport measurements, especially in conjunction with contemporaneous observations of local seismicity, vent fluid temperature and chemistry, and biological activity before, during, and after the event, can provide valuable insights on the coupling of a hydrothermal system with geological events and local biological community.

Chapter 6

Conclusions

The principal objective of this dissertation is to use the observational data recorded by the Cabled Observatory Vent Imaging Sonar (COVIS) to explore the temporal variability of a seafloor hydrothermal system and its response to oceanic, atmospheric, and geological processes. Since its deployment in 2010, COVIS has recorded a long-term (> 3 years) near-continuous dataset of the acoustic backscatter from the buoyant plumes discharging from the venting sulfide structure Grotto located on the Endeavour Segment of the Juan de Fuca Ridge. Processing this dataset yields long-term time-series measurements of the vertical flow rate, volume transport, expansion rate, and heat transport of the largest plume above Grotto. The acquisition of these time-series measurements using COVIS is a testament to the effectiveness and robustness of employing a moored acoustic imaging sonar installed in an underwater observatory for long-term, time-series observations of a seafloor hydrothermal system. Moreover, further analysis of those time-series measurements, as presented in Chapters 2 to 4, sheds light on the acoustic scattering mechanisms within a hydrothermal plume, the temporal variability of the dynamics of the plume and its response to tidal and atmospheric forcing, and the influences of seismic activity on a seafloor hydrothermal system. The following is a summary of the principal conclusions reached in each chapter.

Chapter 2 presents an investigation of the relative importance of plume particles and temperature fluctuations as the acoustic backscattering mechanisms within the buoyant plumes above Grotto. The result suggests temperature fluctuations are the dominant backscattering mechanism within the initial 10-m rise of the plume. The relative contribution of plume particles to acoustic backscatter increases with height and can possibly be significant at higher levels of the plume. Furthermore, the estimated temperature fluctuations obtained by inverting the observed acoustic backscatter show a reasonable match to

the in-situ measurements, which demonstrates the potential of using acoustic backscatter as a remote-sensing tool to measure the temperature fluctuations within a hydrothermal plume.

Chapter 3 introduces the methodology for processing the acoustic backscatter data to get estimates of multiple physical properties of the largest plume above Grotto. This chapter also presents the 26-day time series of the volume transport, vertical flow rate, and expansion rate of the largest plume above Grotto obtained by processing the acoustic data recorded in October 2010. This time series represents a significant advance in data collection over earlier plume studies due to the ability to track not only the temporal variations of an integrated plume issuing from the multiple vents on a sulfide structure but also the plume's spatial evolution over its initial 10-m rise. The advance also resides in the confidence with which the plume is imaged in three dimensions, which allows the plume to be accurately located. Moreover, analysis of the temporal variations observed in the time-series suggests the rate at which a hydrothermal plume mixes with the ambient seawater increases with the magnitude of ambient ocean currents. Such current-driven entrainment introduces the oscillations in the ambient currents that are driven by tidal and atmospheric forcing into the flow field of the plume, which in turn links the dynamics of a deep-sea hydrothermal plume with oceanic and atmospheric processes.

Chapter 4 presents a 41-month extension to the 26-day time series in Chapter 3 obtained by processing the acoustic data recorded from October 2011 to February 2015. Analysis of the temporal variations observed in the 41-month time series further corroborates the conclusion in Chapter 3 that the current-driven entrainment introduces the oscillations in the ambient currents into the flow field of a deep-sea hydrothermal plume. Furthermore, based on the fact that a hydrothermal plume bends towards the downstream direction of the ambient current, we estimate the direction and relative amplitude of the local bottom currents from the bending angles of the largest plume above Grotto observed in the 3-D acoustic plume images produced by COVIS. Comparing the result with the measurements made by the ADCP at approximately 80 m down south from Grotto reveals significant difference in the mean flows. Such difference points to the complexity of the bottom flow structure within a hydrothermal vent field, which is subject to bottom topography, entrainment flows

driven by local buoyant plumes, and background ocean currents.

Chapter 5 introduces the inverse method developed to estimate the source heat transport driving a hydrothermal plume from its volume transport estimates. The application of this method to the volume transport estimates obtained by processing COVIS data yields a 41-month time series (October 2011 to February 2015) of the source heat transport driving the largest plume above Grotto. This time series is a major advance over earlier heat transport measurements due to its long duration (41-month) and high temporal resolution ($\sim$ 1 sample/day), and is thus an unprecedented tool for studying the temporal variability of the heat source driving a seafloor hydrothermal system over broad time scales (days to years). Inspection of this time series suggests the heat source driving the plume remained relatively steady during the 41-month period. Furthermore, comparing this current time series with historical heat transport measurements suggests the heat source driving the largest plume of Grotto remained at a steady level since 1988 except for a brief period of increased heat transport in 2000. Further comparison between the heat transport measurements and local seismic data reveals that the brief period of increased heat transport in 2000 followed the pronounced seismic events in 1999 and 2000 and the reduced steady heat flux from October 2011 to February 2015 coincided with quiescent seismicity. Such a correlation between hydrothermal heat output and the rate of local seismicity points to the close linkage between a seafloor hydrothermal system with geological processes.

All in all, the findings in this dissertation demonstrate the intimate interconnections of a seafloor hydrothermal system with the processes spanning from the Earth's interior to the sea surface. The results suggest ocean currents enhance the mixing of a buoyant hydrothermal plume with the ambient seawater and introduce the oscillations driven by tidal and atmospheric forcing into the plume's flow field. This finding calls for the necessity of obtaining contemporaneous current measurements in future plume studies. Moreover, this finding suggests ocean currents, in addition to being an important vector for dispersing vent-generated materials (e.g., chemicals, larvae, etc.), have a significant impact on the precipitation of hydrothermal chemicals that happens when the plume fluid mixes with the ambient seawater. This notion argues for the importance of studying the bottom currents near a hydrothermal system to the understanding of its geochemical contribution to the

abyssal ocean. The hydrothermal heat transport time series and historical heat transport measurements presented in this dissertation suggest pronounced geological events can cause large perturbations in the heat output of a hydrothermal system, which on the other hand can remain steady on a decadal scale during quiescent seismicity. This finding points to the necessity of recording contemporaneous seismic data in future vent studies, which is important for interpreting and potentially predicting the temporal variability of hydrothermal heat output. Concisely, the results presented in this dissertation show that a deep-sea hydrothermal system is a focal point of interconnections among geological, oceanic, atmospheric, and hydrothermal processes. Studying these interconnections is key to a better understanding of the role of a seafloor hydrothermal system in the Earth-ocean system, which has been and will continue to be a major goal driving hydrothermal vent research.

Bibliography

Adams, D.K., Jr, D.J.M., Zamudio, L., Thurnherr, A.M., Liang, X., Rouxel, O., German, C.R., Mullineaux, L.S., 2011. Surface-Generated Mesoscale Eddies Transport Deep-Sea Products from Hydrothermal Vents. Science 332, 580–583. doi:10.1126/science.1201066.

Baker, E.T., 2007. Hydrothermal cooling of midocean ridge axes: Do measured and modeled heat fluxes agree? Earth and Planetary Science Letters 263, 140–150. doi:10.1016/j.epsl.2007.09.010.

Baker, E.T., Chadwick, W.W., Cowen, J.P., Dziak, R.P., Rubin, K.H., Fornari, D.J., 2012. Hydrothermal discharge during submarine eruptions: The importance of detection, response, and new technology. Oceanography 25, 128–141.

Baker, E.T., Fox, C.G., Cowen, J.P., 1999. In situ observations of the onset of hydrothermal discharge during the 1998 submarine eruption of Axial Volcano, Juan de Fuca Ridge. Geophysical Research Letters 26, 3445–3448. doi:10.1029/1999gl002331.

Baker, E.T., Massoth, G.J., Feely, R.A., 1987. Cataclysmic hydrothermal venting on the Juan de Fuca Ridge. Nature 329, 149–151.

Baker, E.T., Massoth, G.J., Feely, R.A., Cannon, G.A., Thomson, R.E., 1998. The rise and fall of the CoAxial hydrothermal site, 1993-1996. Journal of Geophysical Research-Solid Earth 103, 9791–9806.

Barreyre, T., Escartín, J., Sohn, R.A., Cannat, M., Ballu, V., Crawford, W.C., 2014. Temporal variability and tidal modulation of hydrothermal exit-fluid temperatures at the lucky strike deep-sea vent field, mid-atlantic ridge. Journal of Geophysical Research 119, 2543–2566. doi:10.1002/2013JB010478.

Bemis, K., Silver, D., Rona, P., Cowen, J., 2006. A particle sedimentation model of buoyant jets: observations of hydrothermal plumes. Cahiers De Biologie Marine 47, 379–384.

Bemis, K.G., Herzen, R.P.V., Mottl, M.J., 1993. Geothermal heat flux from hydrothermal plumes on the Juan de Fuca Ridge. Journal of Geophysical Research 98, 6351–6365.

Bemis, K.G., Lowell, R.P., Farough, A., 2012. Diffuse flow on and around hydrothermal vents at mid-ocean ridges. Oceanography 25, 182–191. doi:10.5670/oceanog.2012.16.

Bemis, K.G., Rona, P.A., 2006. Are hydrothermal plumes lazy?: implications for the entrainment of diffuse flow. EOS, Transactions, American Geophysical Union 87. Fall Meet. Suppl. abstr. B33D-08.

Bemis, K.G., Rona, P.A., Jackson, D., Jones, C., Silver, D., Mitsuzawa, K., 2002. A comparison of black smoker hydrothermal plume behavior at Monolith Vent and at Clam Acres Vent Field: Dependence on source configuration. Marine Geophysical Researches 23, 81–96.

Bemis, K.G., Silver, D., Xu, G., Light, R., Jackson, D., Jones, C., Ozer, S., Liu, L., 2015. The path to COVIS: a review of acoustic imaging of hydrothermal flow regimes. Deep-Sea Research Part II doi:10.1016/j.dsr2.2015.06.002.

Berdeal, I.G., 2006. Hydrography and flow in the axial valley of the Endeavour Segment: implications for larval dispersal. Ph.D. thesis. University of Washington.

Bickle, M., Elderfield, H., 2004. Hydrothermal fluxes in a global context, in: Davis, E., Elderfield, H. (Eds.), Hydrogeology of the Ocean Lithosphere. Cambridge University Press, pp. 677–690.

Bischoff, J.L., Rosenbauer, R.J., 1985. An empirical equation of state for hydrothermal seawater (3.2 percent NaCl). American Journal of Science 285, 735–763.

Bohnenstiehl, D.R., Dziak, R.P., Tolstoy, M., Fox, C.G., Fowler, M., 2004. Temporal and spatial history of the 19992000 Endeavour Segment seismic series, Juan de Fuca Ridge. Geochemistry Geophysics Geosystems 5. doi:10.1029/2004GC000735.

Bonadonna, C., Ernst, G.G.J., Sparks, R.S.J., 1998. Thickness variations and volume estimates of tephra fall deposits: the importance of particle Reynolds number. Journal of Volcanology and Geothermal Research 81, 173–187. doi:10.1016/S0377-0273(98)00007-9.

Bursik, M.I., Sparks, R.S.J., Gilbert, J.S., Carey, S.N., 1992. Sedimentation of Tephra by Volcanic Plumes: I. Theory and Its Comparison with a Study of the Fogo A plinian Deposit, Sao Miguel (Azores). Bulletin of Volcanology 54, 329–344. doi:10.1007/Bf00301486.

Butterfield, D.A., McDuff, R.E., Mottl, M.J., Lilley, M.D., Lupton, J.E., Massoth, G.J., 1994. Gradients in the composition of hydrothermal fluids from the Endeavour segment vent field: Phase separation and brine loss. Journal of Geophysical Research 99, 9561–9583.

Carazzo, G., Kaminski, E., Tait, S., 2006. The route to self-similarity in turbulent jets and plumes. Journal of Fluid Mechanics 547, 137–138. doi:10.1017/S002211200500683X.

Chadwick, W.W., Clague, D.A., Embley, R.W., Perfit, M.R., Butterfield, D.A., Caress, D.W., Paduan, J.B., Martin, J.F., Sasnett, P., Merle, S.G., Bobbitt, A.M., 2013. The 1998 eruption of Axial Seamount: New insights on submarine lava flow emplacement from high-resolution mapping. Geochemistry Geophysics Geosystems 14, 3939–3968.

Chaengbamrung, A., 2005. Turbulent plumes generated by a horizontal area source of buoyancy. Ph.D. thesis. University of Wollongong.

Chu, V.H., 1994. Lagrangian scales of jets and plumes with dominant eddies, in: Davies, P.A., Neves, M.J.V. (Eds.), Recent research advances in the fluid mechanics of turbulent jets and plumes. Kluwer Academic Publishers, Dordrecht, The Netherlands, pp. 45–72. NATO ASI Series E: Applied Sciences, Vol. 255.

Clague, D.A., Caress, D.W., Thomas, H., Thompson, D., Calarco, M., Holden, J., Butterfield, D., 2008. Abundance and distribution of hydrothermal chimneys and mounds on the Endeavour Ridge determined by 1-m resolution AUV multibeam mapping surveys. EOS, Transactions, American Geophysical Union 89. Fall Meet. Suppl. abstr. V41B-2079.

Clague, D.A., Dreyer, B.M., Paduan, J.B., Martin, J.F., Caress, D.W., Gill, J.B., Kelley, D.S., Thomas, H., Portner, R.A., Delaney, J.R., Guilderson, T.P., McGann, M.L., 2014. Eruptive and tectonic history of the Endeavour Segment, Juan de Fuca Ridge, based on AUV mapping data and lava flow ages. Geochemistry Geophysics Geosystems 15, 3364–3391. doi:10.1002/2014GC005415.

Corliss, J.B., Dymond, J., Gordon, L.I., Edmond, J.M., von Herzen, R.P., Ballard, R.D., Green, K., Williams, D., Bainbridge, A., Crane, K., van Andel, T.H., 1979. Submarine Thermal Springs on the Galapagos Rift. Science 203, 1073–1083.

Crone, T.J., Wilcock, W.S.D., 2005. Modeling the effects of tidal loading on mid-ocean ridge hydrothermal systems. Geochemistry Geophysics Geosystems 6. doi:10.1029/2004GC000905.

Crone, T.J., Wilcock, W.S.D., McDuff, R.E., 2010. Flow rate perturbations in a black smoker hydrothermal vent in response to a mid-ocean ridge earthquake swarm. Geochemistry Geophysics Geosystems 11. doi:10.1029/2009GC002926.

Delaney, J.R., Robigou, V., McDuff, R.E., Tivey, M.K., 1992. Geology of a vigorous hydrothermal system on the Endeavour Segment, Juan de Fuca Ridge. Journal of Geophysical Research 97, 19663–19682.

Di Iorio, D., Lavelle, J.W., Rona, P.A., Bemis, K., Xu, G., Germanovich, L.N., Lowell, R.P., Genc, G., 2012. Measurements and models of heat flux and plumes from hydrothermal discharges near the deep seafloor. Oceanography 25, 168–181.

Di Iorio, D., Lemon, D., Chave, R., 2005. A self-contained acoustic scintillation instrument for path-averaged measurements of flow and turbulence with application to hydrothermal vent and bottom boundary layer dynamics. Journal of Atmospheric and Oceanic Technology 22, 1602–1617.

Dziak, R., Cowen, J., Baker, E., Bohnenstiehl, D., Chadwick, B., Resing, J., Embley, R., 1996. Detecting volcanic events in the Northeast Pacific. EOS, Transactions, American Geophysical Union 87(4), 37–42.

Dziak, R., Hammond, S.R., Fox, C.G., 2011. A 20-year hydroacoustic time series of seismic and volcanic events in the Northeast Pacific Ocean. Oceanography 24, 280–293.

Edmond, J.M., Measures, C., McDuff, R.E., Chan, L.H., Collier, R., Grant, B., 1979. Ridge crest hydrothermal activity and the balances of the major and minor elements in the ocean: the Galapagos data. Earth Planetary Science Letters 46, 1–18.

Emery, W.J., Lee, W.G., Magaard, L., 1984. Geographic and seasonal distributions of Brunt-Väisälä frequency and Rossby radii in the North Pacific and North Atlantic. Journal of Physical Oceanography 14, 294–317.

Ernst, G.G.J., Sparks, R.S.J., Carey, S.N., Bursik, M.I., 1996. Sedimentation from turbulent jets and plumes. Journal of Geophysical Research-Solid Earth 101, 5575–5589. doi:10.1029/95jb01900.

Eyer, L., Bartholdi, P., 1999. Variable stars: Which Nyquist frequency? Astronomy and Astrophysics Supplement Series 135, 1–3.

Fan, L.N., 1967. Turbulent buoyant jets into stratified or flowing ambient fluids. Technical Report. California Institute of Technology.

Feely, R., Geiselman, T., Baker, E., Massoth, G., Hammond, S., 1990. Distribution and Composition of Hydrothermal Plume Particles from the ASHES Vent Field at Axial Volcano, Juan de Fuca Ridge. Journal of Geophysical Research 95, 12855–12873.

Feely, R.A., Baker, E.T., Lebon, G.T., Gendron, J.F., Massoth, G.J., Mordy, C.W., 1998. Chemical variations of hydrothermal particles in the 1996 Gorda Ridge Event and chronic plumes. Deep-Sea Research Part II 45, 2637–2664.

Feely, R.A., Lewison, M., Massoth, G.J., Robert-Baldo, G., Lavelle, J.W., Byrne, R.H., Damm, K.L.V., Herbert C.Curl, J., 1987. Composition and Dissolution of Black Smoker Particulates from Active Vents on the Juan de Fuca Ridge. Journal of Geophysical Research 92, 11347–11363. doi:10.1029/JB092iB11p11347.

Feely, R.A., Massoth, G.J., Trefry, J.H., Baker, E.T., Paulson, A.J., Lebon, G.T., 1994.

Composition and sedimentation of hydrothermal plume particles from North Cleft segment, Juan de Fuca Ridge. Journal of Geophysical Research 99, 4985–5006.

Fischer, H.B., LIst, E.J., Koh, R.C., Imberger, J., Brooks, N.H., 1979. Mixing in Inland and Coastal Waters. Academic Press. chapter 9.

Fornari, D., Damm, K.V., Bryce, J., Cowen, J., Ferrini, V., Fundis, A., Lilley, M., Luther, III, G.W., Mullineaux, L., Perfit, M., Meana-Prado, M., Rubin, K., Jr., W.S., Shank, T., Soule, S., Tolstoy, M., White, S., 2012. The East Pacific Rise between 9°N and 10°N: Twenty-five years of integrated, multidisciplinary oceanic spreading center studies. Oceanography 25, 18–43. doi:10.5670/oceanog.2012.02.

Francois, R.E., Garrison, G.R., 1982. Sound adsorption based on ocean measurements: Part I: Pure water and magnesium sulfate contributions. Journal of the Acoustical Society of America 72, 896–907.

Gartman, A., Findlay, A.J., Luther, III, G.W., 2014. Nanoparticulate pyrite and other nanoparticles are a widespread component of hydrothermal vent black smoker emissions. Chemical Geology 366, 32–41. doi:10.1016/j.chemgeo.2013.12.013.

German, C.R., Seyfried, Jr., W.E., 2014. Hydrothermal processes, in: Holland, H., Turekian, K. (Eds.), The Oceans and Marine Geochemistry, Treatise on Geochemistry (Second Edition). Elsevier Science. volume 8, pp. 191–233.

Germanovich, L.N., DiIorio, D., Genc, G., Hurt, R.S., Lowell, R.P., Olson, E.J., 2009. Direct measurements of hydrothermal heat output at Juan de Fuca Ridge. EOS, Transactions, American Geophysical Union 90. Fall Meet. Suppl. abstr. OS13A-1179.

Germanovich, L.N., Lowell, R.P., Astakhov, D.K., 2000. Stress-dependent permeability and the formation of seafloor event plumes. Journal of Geophysical Research-Solid Earth 105, 8341–8354. doi:10.1029/1999jb900431.

Ginster, U., Mottl, M.J., Von Herzen, P., 1994. Heat flux from black smokers on the Endeavour and Cleft segments, Juan de Fuca Ridge. Journal of Geophysical Research 99, 4937–4950.

Glickson, D.A., Kelley, D.S., Delaney, J.R., 2007. Geology and hydrothermal evolution of the Mothra Hydrothermal Field, Endeavour Segment, Juan de Fuca Ridge. Geochemistry Geophysics Geosystems 8. doi:10.1029/2007GC001588.

Goto, S., Kinoshita, M., Schultz, A., Herzen, R.P.V., 2003. Estimate of heat flux and its temporal variation at the TAG hydrothermal mound, Mid-Atlantic Ridge 26 degrees N. Journal of Geophysical Research-Solid Earth 108. doi:10.1029/2001jb000703.

Govenar, B., 2012. Energy Transfer Through Food Webs at Hydrothermal Vents: Linking the Lithosphere to the Biosphere. Oceanography 25, 246–255.

Gregg, M.C., 1987. Diapycnal Mixing in the Thermocline: A Review. Journal of Geophysical Research 92, 5249–5286. doi:10.1029/JC092iC05p05249.

Helfrich, K.R., Speer, K.G., 1995. Oceanic Hydrothermal Circulation: Mesoscale and Basin-Scale Flow, in: Humphris, S.E., Zierenberg, R.A., Mullineaux, L.S., Thomson, R.E. (Eds.), Seafloor Hydrothermal Systems: Physical, Chemical, Biological, and Geological Interactions. American Geophysical Union, pp. 347–356. Geophysical Monograph, vol: 91.

Hocke, K., Kampfer, N., 2009. Gap filling and noise reduction of unevenly sampled data by means of the Lomb-Scargle periodogram. Atmospheric Chemistry and Physics 9, 4197–4206.

Hooft, E.E.E., Patel, H., Wilcock, W., Becker, K., Butterfield, D., Davis, E., Dziak, R., Inderbitzen, K., Lilley, M., McGill, P., Toomey, D., Stakes, D., 2010. A seismic swarm and regional hydrothermal and hydrologic perturbations: The northern Endeavour Segment, February 2005. Geochemistry Geophysics Geosystems 11. doi:10.1029/2010GC003264.

Horn, D.P., Walton, S.M., 2007. Spatial and temporal variations of sediment size on a mixed sand and gravel beach. Sedimentary Geology 202, 509–528.

Ishimaru, A., 1978. Wave Propagation and Scattering in Random Media. Academic Press, Burlington, Massachusetts. volume 2.

Jackson, D.R., Jones, C.D., Rona, P.A., Bemis, K.G., 2003. A Method for Doppler acoustic measurement of black smoker flow fields. Geochemistry Geophysics Geosystems 4, 1095–1107. doi:10.1029/2003GC000509.

Jackson, P.R., Ledwell, J.R., Thurnherr, A.M., 2010. Dispersion of a tracer on the East Pacific Rise (9°N to 10°N), including the influence of hydrothermal plumes. Deep-Sea Research Part I 57, 37–52.

Jamieson, J.W., Hannington, M.D., Clague, D.A., Kelley, D.S., Delaney, J.R., Holden, J.F., Tivey, M.K., Kimpe, L.E., 2013. Sulfide geochronology along the Endeavour Segment of the Juan de Fuca Ridge. Geochemistry Geophysics Geosystems 14, 2084–2099.

Johnson, H.P., Hautala, S.L., Tivey, M.A., Jones, C., Voight, J., Pruis, M., Garcia-Berdeal, I., Gilbert, L., Bjorklund, T., Fredericks, W., Howland, J., the Thermal Grid Scientific Party, 2002. A systematic examination of hydrothermal circulation: Endeavour Segment, Juan de Fuca Ridge. EOS, Transactions, American Geophysical Union 83, 73–78.

Johnson, H.P., Hutnak, M., Dziak, R.P., Fox, C.G., Urcuyo, I., Cowen, J.P., Nabelek, J., 2000. Earthquake-induced changes in a hydrothermal system on the Juan de Fuca mid-ocean ridge. Nature 407, 174–177.

Jonasz, M., 1983. Particle-Size Distributions in the Baltic. Tellus Series B-Chemical and Physical Meteorology 35, 346–358.

Jupp, T.E., Schultz, A., 2004. Physical balances in subseafloor hydrothermal convection cells. Journal of Geophysical Research 109. doi:10.1029/2003JB002697.

Karsten, J.L., Hammond, S.R., Davis, E.E., Currie, R.G., 1986. Detailed geomorphology and neotectonics of the Endeavour Segment, Juan de Fuca Ridge: New results from Seabeam swath mapping. Geological Society of America Bulletin 97, 213–221.

Kelley, D.S., Carbotte, S.M., Caress, D.W., Clague, D.A., Delaney, J.R., Gill, J.B., Hadaway, H., Holden, J.F., Hooft, E.E., Kellogg, J.P., Lilley, M.D., Stoermer, M., Toomey, D., Weekly, R., Wilcock, W.S., 2012. Endeavour Segment of the Juan de

Fuca Ridge: One of the most remarkable places on Earth. Oceanography 25, 44–61. doi:10.5670/oceanog.2012.03.

Kelley, D.S., Delaney, J.R., Kim Juniper, S., 2014. Establishing a newera of submarine volcanic observatories: Cabling Axial Seamount and the Endeavour Segment of the Juan de Fuca Ridge. Marine Geology 352, 426–450.

Kellogg, J.P., 2011. Temporal and spatial variability of hydrothermal fluxes within a mid-ocean ridge segment. Ph.D. thesis. University of Washington.

Kundu, P.K., Thomson, R.E., 1985. Inertial Oscillations due to a Moving Front. Journal of Physical Oceanography 15, 1076–1084.

Larson, B.I., Lilley, M.D., Olson, E.J., 2009. Parameters of subsurface brines and hydrothermal processes 12-15 months after the 1999 magmatic event at the Main Endeavor Field as inferred from in situ time series measurements of chloride and temperature. Journal of Geophysical Research 114. doi:10.1029/2008JB005627.

Larson, B.I., Olson, E.J., Lilley, M.D., 2007. In situ measurement of dissolved chloride in high temperature hydrothermal fluids. Geochimica et Cosmochimica Acta 71, 2510–2523. doi:10.1016/j.gca.2007.02.013.

Lavelle, J., Wetzler, M.A., 1999. Diffuse venting and background contributions to chemical anomalies in a neutrally buoyant ocean hydrothermal plume. Journal of Geophysical Research 104, 3201–3209.

Lavelle, J.W., Di Iorio, D., Rona, P.A., 2013. A turbulent convection model with an observational context for a deep-sea hydrothermal plume in a time-variable cross-flow. Journal of Geophysical Research 118, 1–16. doi:10.1002/2013JC009165.

Lavery, A.C., Geyer, W.R., Scully, M.E., 2013. Broadband acoustic quantification of stratified turbulence. Journal of the Acoustical Society of America 134, 40–54.

Lilley, M.D., Butterfield, D.A., Lupton, J.E., Olson, E.J., 2003. Magmatic events can produce rapid changes in hydrothermal vent chemistry. Nature 422, 878–881.

Luther, III, G.W., Gartman, A., Yucel, M., Madison, A., Moore, T.S., Nees, H.A., Nuzzio, D.B., Sen, A., Lutz, R.A., Shank, T.M., Fisher, C.R., 2012. Chemistry, temperature, and faunal distributions at diffuse-flow hydrothermal vents: Comparison of two geologically distinct ridge systems. Oceanography 25, 234–245. doi:10.5670/oceanog.2012.22.

Medwin, H., Clay, C.S., 1998. Fundamentals of Acoustical Oceanography. Academic Press, San Diego, California. chapter 7.

Mei, W., Pasquero, C., Primeau, F., 2012. The effect of translation speed upon the intensity of tropical cyclones over the tropical ocean. Geophysical Research Letters 39. doi:10.1029/2011GL050765.

Morton, B.R., 1959. Forced Plumes. Journal of Fluid Mechanics 5, 151–163. doi:10.1017/S002211205900012X.

Morton, B.R., Taylor, G., Turner, J., 1956. Turbulent Gravitational Convection from Maintained and Instantaneous Sources. Proceedings of the Royal Society of London 234, 1–23.

Mottl, M.J., 2003. Partitioning of energy and mass fluxes between mid-ocean ridge axes and flanks at high and low temperature, in: Halbach, P.E., Tunnicliffe, V., Hein, J.R. (Eds.), Energy and Mass Transfer in Marine Hydrothermal Systems. Berlin:Dahlem University Press, pp. 271–287.

Mottl, M.J., McConachy, T.F., 1990. Chemical processes in buoyant hydrothermal plumes on the East Pacific Rise near 21°N. Geochimica et Cosmochimica Acta 54, 1911–1927.

Mullineaux, L.S., France, S.C., 1995. Dispersal Mechanisms of Deep-Sea Hydrothermal Vent Fauna. Geophysical Monograph 91, 408–424.

Mullineaux, L.S., Mills, S.W., Sweetman, A.K., Beaudreau, A.H., Metaxas, A., Hunt, H.L., 2005. Vertical, lateral and temporal structure in larval distributions at hydrothermal vents. Marine Ecology Progress Series 293, 1–16.

Nielsen, S.G., Rehkamper, M., Teagle, D.A.H., Butterfield, D.A., Alt, J.C., Halliday, A.N.,

2006. Hydrothermal fluid fluxes calculated from the isotopic mass balance of thallium in the ocean crust. Earth Planetary Science Letters 251, 120–133.

Oakey, N.S., 1982. Determination of the Rate of Dissipation of Turbulent Energy from Simultaneous Temperature and Velocity Shear Microstructure Measurements. Journal of Physical Oceanography 12, 256–271.

Ocean Networks Canada Data Archive, 2011. http://www.oceannetworks.ca, COVIS Doppler data from 30 Sept 2010 to 25 Oct 2010, Oceans Networks Canada, University of Victoria, Canada. Downloaded in Jan 2011 .

Ocean Networks Canada Data Archive, 2014. http://www.oceannetworks.ca, BARS temperature data from 1 Oct 2010 to 10 Feb 2014, Oceans Networks Canada, University of Victoria, Canada. Downloaded on 17 Feb 2014 .

Ocean Networks Canada Data Archive, 2015a. http://www.oceannetworks.ca, ADCP data from Main Endeavour Field from June 2013 to Feb 2015, Oceans Networks Canada, University of Victoria, Canada. Downloaded in Mar 2015 .

Ocean Networks Canada Data Archive, 2015b. http://www.oceannetworks.ca, COVIS Doppler data from 1 Oct 2011 to 27 Feb 2015, Oceans Networks Canada, University of Victoria, Canada. Downloaded between Jan 2011 and Mar 2015 .

Palmer, D., 1996. Rayleigh scattering from nonspherical particles. Journal of the Acoustical Society of America 99, 1901–1912.

Palmer, D.R., Rona, P.A., Mottl, M.J., 1986. The acoustics of "black smoker" hydrothermal plumes. Journal of the Acoustical Society of America 80, 888–898.

Papanicolaou, P.N., List, E., 1988. Investigation of round vertical turbulent buoyant jet. Journal of Fluid Mechanics 195, 341–391. doi:10.1017/S0022112088002447.

Pardo-Iguzquiza, E., Rodriguez-Tovar, F.J., 2012. Spectral and cross-spectral analysis of uneven time series with the smoothed LombScargle periodogram and Monte Carlo evaluation of statistical significance. Computer and Geosciences 49, 207–216. doi:10.1016/j.cageo.2012.06.018.

Pawlowicz, R., Beardsley, B., Lentz, S., 2002. Classical tidal harmonic analysis including error estimates in MATLAB using T-TIDE. Computer and Geosciences 28, 929–937.

Pruis, M.J., 2004. Energy and volume flux into the deep ocean: examining diffuse hydrothermal systems. Ph.D. thesis. University of Washington.

Ramondenc, P., Germanovich, L.N., Damm, K.L.V., Lowell, R.P., 2006. The first measurement of hydrothermal heat output at 9°50′ N, East Pacific Rise. Earth Planetary Science Letters 245, 441–464. doi:10.1016/j.epsl.2006.03.023.

Ramondenc, P., Germanovich, L.N., Lowell, R.P., 2008. Modeling the hydrothermal response to earthquakes with application to the 1995 event at 9° 50' N, East Pacific Rise, in: Lowell, R.P., Seewald, J.S., Metaxas, A., Perfit, M.R. (Eds.), Magma to Microbe: Modeling Hydrothermal Processes at Oceanic Spreading Centers. American Geophysical Union, pp. 97–122. Geophysical Monography, vol : 178.

Richardson, M.D., Williams, K.L., Briggs, K.B., Thorsos, E.I., 2002. Dynamic Measurement of Sediment Grain Compressibility at Atmospheric Pressure: Acoustic Applications. IEEE Journal of Oceanic Engineering 27, 593–601.

Rona, P., Light, R., 2011. Sonar images hydrothermal vents in seafloor observatory. EOS, Transactions, American Geophysical Union 92 (20), 169–170.

Rona, P.A., Bemis, K.G., Jones, C.D., Jackson, D.R., 2006. Entrainment and bending in a major hydrothermal plume, Main Endeavour Field, Juan de Fuca Ridge. Geophysical Research Letters 33. doi:10.1029/2006GL027211.

Rona, P.A., Bemis, K.G., Silver, D., Jones, C.D., 2002. Acoustic imaging visualization, and quantification of buoyant hydrothermal plumes in the Ocean. Marine Geophysical Researches 23, 147–168.

Rona, P.A., Bemis, K.G., Xu, G., Mitsuzawa, K., 2015. Estimations of heat transfer from Grotto's North Tower: A NEPTUNE observatory case study. Deep-Sea Research Part II doi:10.1016/j.dsr2.2015.05.010.

Rona, P.A., Hannington, M.D., Raman, C.V., Thompson, G., Tivey, M.K., Humphris, S.E., Lalou, C., Petersen, S., 1993. Active and Relict Sea-Floor Hydrothermal Mineralization at the Tag Hydrothermal Field, Mid-Atlantic Ridge. Economic Geology and the Bulletin of the Society of Economic Geologists 88, 1989–2017.

Rona, P.A., Jackson, D.R., Wen, T., Jones, C., Mitsuzawa, K., Bemis, K.G., 1997. Acoustic mapping of diffuse flow at a seafloor hydrothermal site: Monolith Vent, Juan de Fuca Ridge. Geophysical Research Letters 24, 2351–2354.

Rona, P.A., Palmer, D.R., Jones, C., Chaves, D.A., Czarnecki, M., Carey, E.W., Guerrero, J.C., 1991. Acoustic imaging of hydrothermal plumes: East pacific rise. $21°N$. $109°W$. Geophysical Research Letters 18, 2233–2236.

Ross, T., 2003. Sound Scattering from Oceanic Turbulence. Ph.D. thesis. University of Victoria.

Ross, T., Lueck, R., 1992. Discrete and diffuse heat transfer at ASHES vent field, Axial Volcano, Juan de Fuca Ridge. Earth Planetary Science Letters 109, 57–71.

Ryan, W.B.F., Carbotte, S.M., Coplan, J.O., O'Hara, S., Melkonian, A., Arko, R., Weissel, R.A., Ferrini, V., Goodwillie, A., Nitsche, F., Bonczkowski, J., Zemsky, R., 2009. Global Multi-Resolution Topography synthesis. Geochemistry Geophysics Geosystems 10. doi:10.1029/2008GC002332.

Scargle, J.D., 1982. Studies in astronomical time series analysis. II. Statistical aspects spectral analysis of unevenly spaced data. The Astrophysical Journal 263, 835–853.

Schultz, A., Delaney, J.R., McDuff, R.E., 1992. On the partitioning of heat flux between diffuse and point source seafloor venting. Journal of Geophysical Research 97, 12299–12314.

Schultz, A., Dickson, P., Elderfield, H., 1996. Temporal variations in diffuse hydrothermal flow at TAG. Geophysical Research Letters 23, 3471–3474. doi:10.1029/96gl02081.

Seyfried, W.E., Seewald, J.S., Berndt, M.E., Ding, K., Foustoukos, D.I., 2003. Chemistry of hydrothermal vent fluids from the Main Endeavour Field, northern Juan de Fuca Ridge:

Geochemical controls in the aftermath of June 1999 seismic events. Journal of Geophysical Research-Solid Earth 108.

Sheng, J., Hay, A.E., 1988. An examination of the spherical scatterer approximation in aqueous suspensions of sand. Journal of the Acoustical Society of America 83, 598–610.

Singh, S., Lowell, R.P., Lewis, K.C., 2013. Numerical modeling of phase separation at Main Endeavour Field, Juan de Fuca Ridge. Geochemistry Geophysics Geosystems 14, 4021–4034. doi:10.1002/ggge.20249.

Sohn, R.A., Fornari, D.J., Damm, K.L.V., Hildebrand, J.A., Webb, S.C., 1998. Seismic and hydrothermal evidence for a cracking event on the East Pacific Rise crest at 9 degrees 50 ' N. Nature 396, 159–161. doi:10.1038/24146.

Stahr, F.R., McDuff, R.E., Yoerger, D.R., Bradley, A.M., Nakamura, K., 2000. Heat flux measurements at the Main Endeavour vent field, Juan de Fuca Ridge. EOS, Transactions, American Geophysical Union 81 (48), Abstract OS521–03.

Stein, C., Stein, S., 1994. Constraints on hydrothermal heat flux through the oceanic lithosphere from global heat flow. Journal of Geophysical Research 99, 3081–3095.

Stein, C.A., Stein, S., 1992. A model for the global variation in oceanic depth and heat flow with lithospheric age. Nature 359, 123–129.

Stommel, H., 1982. Is the South Pacific Helium-3 plume dynamically active? Earth Planetary Science Letters 61, 63–67.

Tao, Y., Rosswog, S., Brug, M., 2013. A simulation modeling approach to hydrothermal plumes and its comparison to analytical model. Ocean Modelling 61, 68–80.

Taylor, J.R., 1982. An Introduction to Error Analysis. University Science Books, Mill Valley, California. chapter 3. The Study of Uncertainties in Physical Measurements.

Thompson, W.J., McDuff, R.E., Stahr, F.R., Yoerger, D.R., Jakuba, M., 2005. Heat Flux From the Endeavour Segment of the Juan de Fuca Ridge. EOS, Transactions, American Geophysical Union 86. Fall Meet. Suppl. abstr. T31A-0489.

Thomson, R.E., Gordon, R.L., Dymond, J., 1989. Acoustic Doppler Current Profiler Observations of a Mid-Ocean Ridge Hydrothermal Plume. Journal of Geophysical Research 94, 4709–4720.

Thomson, R.E., Mihaly, S.F., Rabinovich, A.B., McDuff, R.E., Veirs, S.R., Stahr, F.R., 2003. Constrained circulation at Endeavour ridge facilitates colonization by vent larvae. Nature 424, 545–549. doi:10.1038/nature01824.

Thomson, R.E., Roth, S.E., Dymond, J., 1990. Near-Inertial Motions Over a Mid-Ocean Ridge: Effects of Topography and Hydrothermal Plumes. Journal of Geophysical Research 95, 7261–7278.

Thorne, P.D., Manley, C., Brimelow, J., 1993. Measurements of the form function and total scattering cross section for a suspension of spheres. Journal of the Acoustical Society of America 93, 243–248.

Thorne, P.D., Meral, R., 2008. Formulations for the scattering properties of suspended sandy sediments for use in the application of acoustics to sediment transport processes. Continental Shelf Research 28, 309–317. doi:10.1016/j.csr.2007.08.002.

Tivey, M.A., Johnson, H.P., 2002. Crustal magnetization reveals subsurface structure of Juan de Fuca Ridge hydrothermal vent fields. Geology 30, 979–982.

Tivey, M.K., Bradley, A.M., Joyce, T.M., Kadko, D., 2002. Insights into tide-related variability at seafloor hydrothermal vents from time-series temperature measurements. Earth Planetary Science Letters 202, 693–707.

Tivey, M.K., Delaney, J.R., 1986. Growth of large sulfide structures on the Endeavour Segment of the Juan de Fuca Ridge. Earth Planetary Science Letters 77, 303–317.

Tolstoy, M., Waldhauser, F., Bohnenstiehl, D.R., Weekly, R.T., Kim, W.Y., 2008. Seismic identification of along-axis hydrothermal flow on the East Pacific Rise. Nature 451, 181–184. doi:10.1038/nature06424.

Turner, J., Campbell, I., 1987. Temperature, density and buoyancy fluxes in 'black smoker'

plumes, and the criterion for buoyancy reversal. Earth Planetary Science Letters 86, 85–92.

VanArk, E.M., Detrick, R.S., Canales, J.P., Carbotte, S.M., Harding, A.J., Kent, G.M., Nedimovic, M.R., Wilcock, W.S.D., Diebold, J.B., Babcock, J.M., 2007. Seismic structure of the Endeavour Segment, Juan de Fuca Ridge: Correlations with seismicity and hydrothermal activity. Journal of Geophysical Research 112. doi:10.1029/2005JB004210.

Veirs, S.R., McDuff, R.E., Stahr, F.R., 2006. Magnitude and variance of near-bottom horizontal heat flux at the Main Endeavour hydrothermal vent field. Geochemistry Geophysics Geosystems 7 (2), doi:10.1029/2005GC000952.

Walker, S.L., Baker, E.T., 1988. Particle-size distribution within hydrothermal plumes over the Juan de Fuca Ridge. Marine Geology 78, 217–226.

Wang, H., Law, A.W.K., 2002. Second-oder integral model for a round turbulent buoyant jet. Journal of Fluid Mechanics 459, 397–428. doi:10.1017/S0022112002008157.

Weekly, R.T., Wilcock, W.S.D., Hooft, E.E.E., Toomey, D.R., McGill, P.R., Stakes, D.S., 2013. Termination of a 6 year ridge-spreading event observed using a seafloor seismic network on the Endeavour Segment, Juan de Fuca Ridge. Geochemistry Geophysics Geosystems 14, 1375–1398.

Wilcock, W.S.D., 2004. Physical response of mid-ocean ridge hydrothermal systems to local earthquakes. Geochemistry Geophysics Geosystems 5. doi:10.1029/2004gc000701.

Wilcock, W.S.D., Hooft, E.E.E., Toomey, D.R., McGill, P.R., Barclay, A.H., Stakes, D.S., Ramirez, T.M., 2009. The role of magma injection in localizing black-smoker activity. Nature Geoscience 2. doi:10.1038/NGE0550.

Xu, G., Di Iorio, D., 2011. The relative effects of particles and turbulence on acoustic scattering from deep-sea hydrothermal vent plumes. Journal of the Acoustical Society of America 130, 1856–1867.

Xu, G., Di Iorio, D., 2012. Deep sea hydrothermal plumes and their interaction with oscillatory flows. Geochemistry Geophysics Geosystems 13. doi:10.1029/2012GC004188.

Xu, G., Jackson, D.R., Bemis, K.G., Rona, P.A., 2013. Observations of the volume flux of a seafloor hydrothermal plume using an acoustic imaging sonar. Geochemistry, Geophysics, Geosystems 14, 2369–2382. doi:10.1002/ggge.20177.

Xu, G., Jackson, D.R., Bemis, K.G., Rona, P.A., 2014. Time-series measurement of hydrothermal heat flux at the Grotto mound, Endeavour Segment, Juan de Fuca Ridge. Earth and Planetary Science Letters 404, 220–231. doi:10.1016/j.epsl.2014.07.040.

Yucel, M., Gartman, A., Chan, C.S., Luther, III, G.W., 2011. Hydrothermal vents as a kinetically stable source of iron-sulphide-bearing nanoparticles to the ocean 4, 367–371. doi:10.1038/NGEO1148.

Appendices

Appendix A

Estimation of Particle Size Distribution

In this appendix, we estimate the size distribution of the particle samples taken from the North Tower plume from the microscopic photos of the particle-laden 0.02 μm Anodisc filters taken using a field emission scanning electron microscope (FESEM) as discussed in Section 2.2.2. Figure A.1 is an example of the microscopic photos taken with 500X magnification. To measure the sizes of the particles observed in this photo, we first use the microscopic image processing software ImageJ to draw the outline of each distinguishable particle and measure the area enclosed in the outline (Figure A.1(b)). We then determine the effective radius of each particle as the radius of the circle having an identical area.

In order to better resolve the sizes of small particles, for the sample from the 1st Niskin bottle, we apply the method above to a total of 6 photos of a given view (i.e. the visible area in a 500X photo) taken with 500X, 1000X, 2000X, 4000X, 8000X, and 16000X magnification respectively. The minimal particle radius that can be reliably measured under each magnification is: 3 μm under 500X, 1.5 μm under 1000X, 1 μm under 2000X, 0.5 μm under 4000X, 0.24 μm under 8000X, and 0.12 μm under 16000X. For the sample from the second Niskin bottle, we apply the same method to only three photos of a given view taken with 500X, 1000X, 2000X magnification respectively. The choice of fewer photos per view for the sample from the 2nd bottle is because the lack of distinguishable particles within the 0.12 to 0.5 μm range on the filter.

We then calculate the histogram of particle radius between 0.2 and 20 μm (the largest observed particle radius) in 0.1 μm intervals. Subsequently, we calculate the weighted average of the histograms obtained from the 6 photos of the same view. The weight applied to each photo is the ratio of the visible area in that photo to the visible area in a 500X photo (e.g., the weight applied to a 500X photo is 1 and the weight applied to a 1000X photo

is 4). The result is a discrete size distribution showing the number of particles per view within each 0.1 μm radius bin between 0.2 and 18 μm. Lastly, we repeat the aforementioned procedures on 25 views of the particle sample from the first Niskin bottle and 30 views of the sample from the second bottle and average the results to obtain the final discrete particle size distribution shown in Figure A.2.

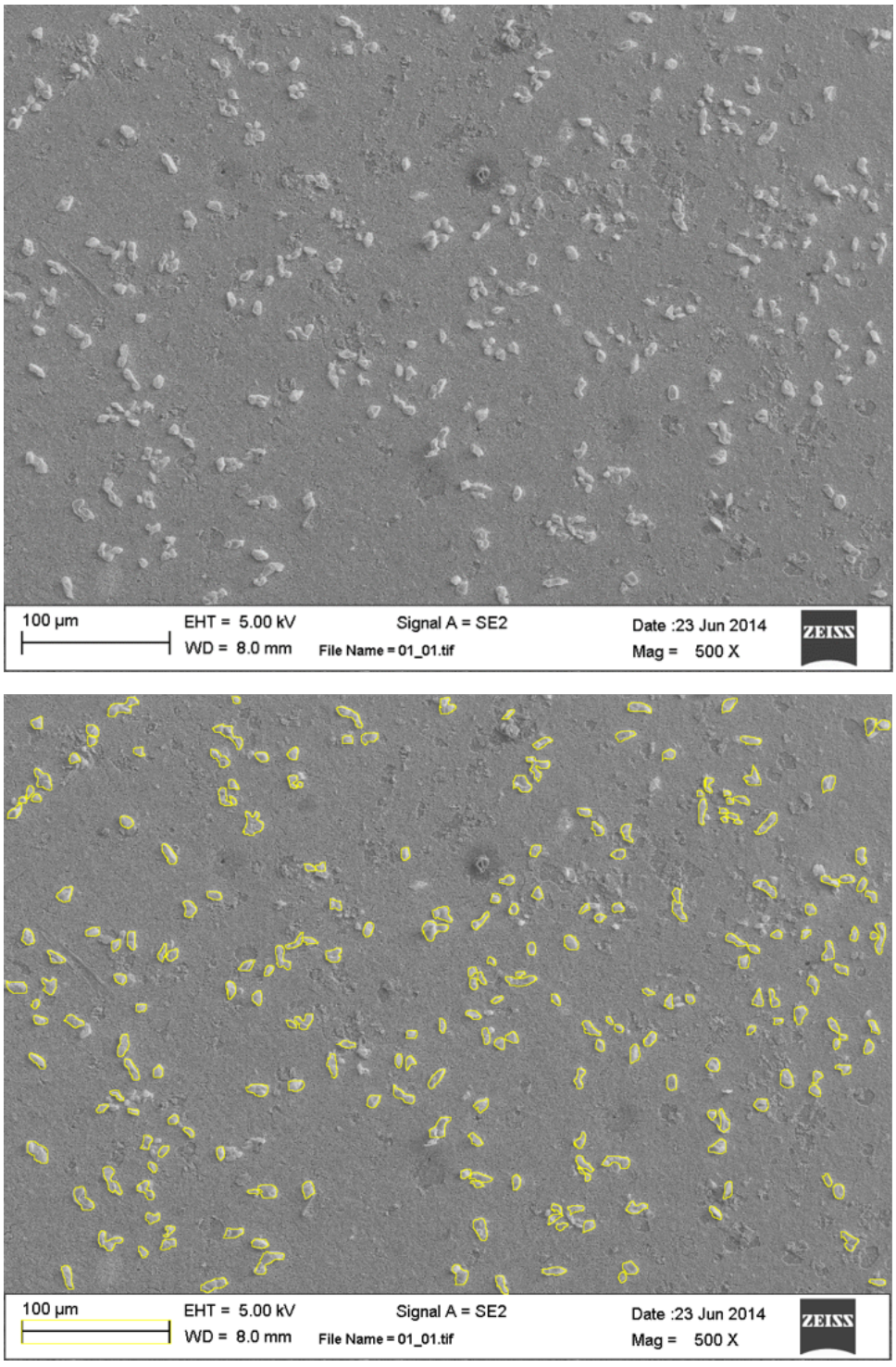

Figure A.1: (a) A 500X FESEM microscopic photo of the particle sample taken from the North Tower plume. (b) Same as (a) with the outlines of the distinguishable particles drawn using the microscopic image processing software ImageJ.

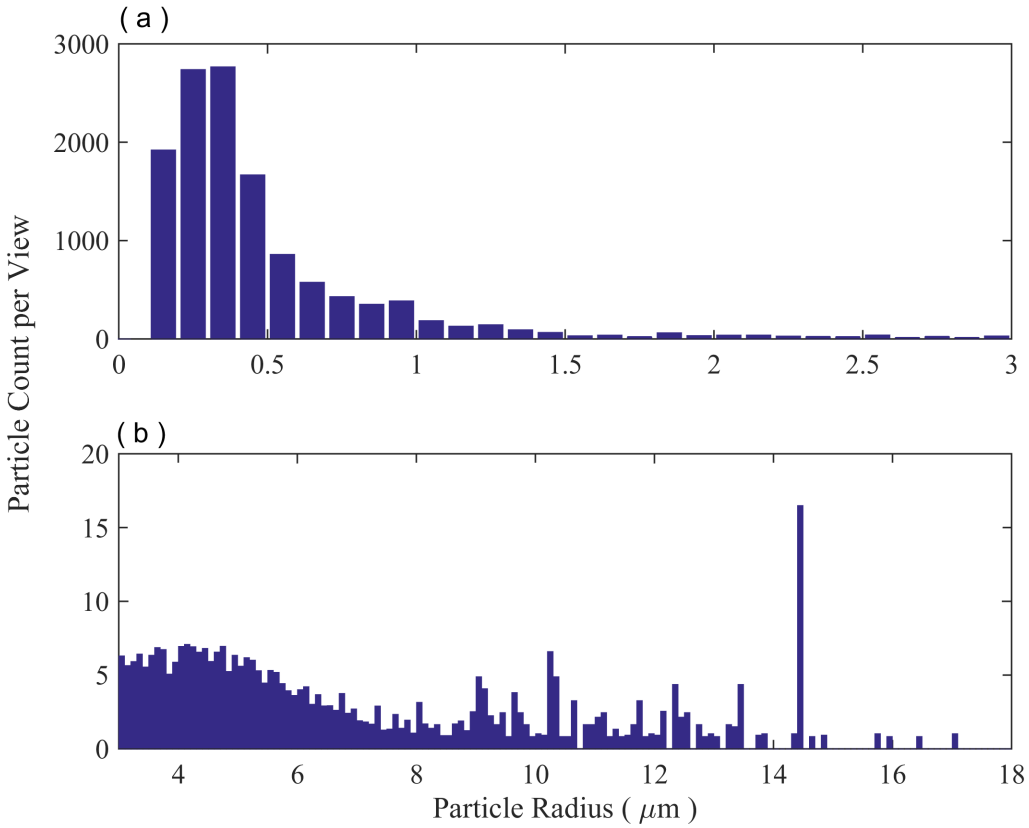

Figure A.2: Discrete size distribution of particles having radii (a) from 0.01 to 3 μm and (b) from 3 to 18 μm.

Appendix B

Backscatter from Individual Particles

This appendix gives the derivation of equation (2.5) in Section 2.3.1. The acoustic backscatter from a particulate suspension can be estimated as the sum of intensities of backscatter from individual particles if multiple scattering is neglected—the single scattering approximation. This approximation is valid under the condition (Ishimaru, 1978)

$$s_{vt}\Delta r \ll 1 \tag{B.1}$$

where s_{vt} is the total volume scattering coefficient of the particulate suspension and Δr is the distance traveled by the sound signal through the suspension. Assuming the sound scattering from the suspension is isotropic, it follows that

$$s_{vt} = 4\pi s_v \tag{B.2}$$

where s_v is the volume backscattering coefficient (i.e., backscattering cross-section per unit solid angle per unit volume). According to Figure 2.7, COVIS measurements suggest $s_v \sim 10^{-5}\,\mathrm{m}^{-1}$ at the center of the North Tower plume at 1 m above the source vents. Substituting this value into equations (B.2) and (B.1) and taking $\Delta r = 4$ m (the mean diameter of the plume within its initial 10-m rise (Xu et al., 2013)) gives $s_{vt}\Delta r \approx 5 \times 10^{-4}$. Therefore, the condition for neglecting multiple scattering is well satisfied.

Applying the single scattering approximation, the volume backscattering coefficient of the particulate suspension is defined as (Medwin and Clay, 1998)

$$s_{vp} = N < |A_s(a)|^2 > . \tag{B.3}$$

Within equation (B.3), N is the number of particles per unit volume of the suspension; $|A_s(a)|^2$ is the squared single-particle backscattering amplitude, which is a function of particle radius (a); $< >$ is the average over the particle size distribution as defined in equation (2.6).

The Rayleigh scattering theory applies for particles whose grain sizes are sufficiently small such that $k_0 a \ll 1$, where $k_0 = 2\pi f_0/c$, f_0 and c are the central frequency of the sonar and sound speed respectively. For COVIS $f_0 = 396$ kHz, and taking $c = 1500$ m/s gives $k_0 = 1.66 \times 10^3$ rad/s. Therefore, the Rayleigh scattering theory is applicable for $a \ll 1/k_0 = 603\,\mu$m, which is well satisfied given the size distribution estimated from the particle samples taken from the North Tower plume (Figure A.2). According to Palmer (1996), the squared backward scattering amplitude averaged over particle shape and orientation within the Rayleigh scattering regime is

$$|A_s(a)|^2 = \frac{k_0^3 a^6}{9}\left\{\left(\frac{e-1}{e} + \frac{h^2-1}{2h}\right)^2 + \frac{1}{20}\frac{(h-1)^4}{h^2}\right\}. \tag{B.4}$$

Within equation (B.4), $e = K_s/K_w$ is the ratio of particle bulk modulus (K_s) to seawater bulk modulus (K_w); $h = \rho_s/\rho_w$ is the ratio of particle density (ρ_s) to seawater density (ρ_w). The particle mass concentration (in units kg/m^3) can be expressed as

$$M = \frac{4\pi\rho_s}{3} N < a^3 > \tag{B.5}$$

where $< a^3 >$ is defined in equation (2.7). Substituting equation (B.5) in equation (B.3) to eliminate N gives

$$s_{vp} =< |A_s(a)|^2 > \left(\frac{3M}{4\pi\rho_s < a^3 >}\right)$$

which is equation (2.5) in Section 2.3.

Appendix C

Backscatter from Turbulence

This appendix gives the derivation of the formulas used to estimate the acoustic backscatter from the turbulence-induced microstructure in the spatial distribution of plume particles and temperature fluctuations as discussed in Sections 2.3.2 and 2.3.3. The aforementioned two mechanisms lead to fluctuations of the acoustic impedance, which in turn scatters sound waves. The relevant volume backscattering coefficient (s_v) can be expressed in terms of the 3-D spatial spectrum of the fluctuations of acoustic impedance as

$$s_v = 2\pi k_0^4 \Phi_\xi(K)|_{\kappa=2k_0}. \tag{C.1}$$

Within equation (C.1), $\Phi_\xi(K)$ is the 3-D spatial spectrum of the normalized acoustic impedance fluctuations ξ (i.e. fluctuations of acoustic impedance divided by its mean) evaluated at the Bragg wavenumber $K = 2k_0$ assuming ξ is homogeneous and isotropic; $k_0 = 2\pi f_0/c$ where f_0 and c are the central frequency of the sonar and sound speed respectively. According to Ross (2003), the 3-D spatial spectrum of fully-developed, homogeneous, isotropic turbulence has the form

$$\Phi_\xi(K) = \frac{C}{2\pi\epsilon^{1/3}} \frac{\chi_\xi}{2} K^{-11/3} \tag{C.2}$$

in the inertial-convective subrange ($\kappa_L \leq K \leq (\frac{5}{12})^{3/2}\kappa_v$, where κ_L is the wavenumber corresponding to the outer scale of the inertial-convective subrange and κ_v is the Kolmogorov wavenumber). In the viscous-convective subrange ($\kappa_{B\xi} > K > (\frac{5}{12})^{3/2}\kappa_v$), the 3-D spatial spectrum has the form

$$\Phi_\xi(K) = \frac{q\nu^{1/2}}{2\pi\epsilon^{1/2}} \frac{\chi_\xi}{2} K^{-3} \exp(-qK^2/\kappa_{B\xi}^2). \tag{C.3}$$

Within equations (C.2) and (C.3), C is a fundamental constant whose value is determined by (Ross, 2003) to be 1.542, $q = 3.7$ is the straining constant, ϵ is the turbulent kinetic energy

dissipation rate, χ_ξ is the acoustic impedance variance dissipation rate, $\kappa_v = (\epsilon/\nu^3)^{1/4}$ is the Kolmogorov wavenumber and ν is the kinematic viscosity of plume fluid, $\kappa_{B\xi} = (\epsilon/(\nu k_\xi^2))^{1/4}$ is the Batchelor wavenumber associated with the acoustic impedance whose molecular diffusivity is k_ξ. Assuming the molecular diffusion of acoustic impedance is dominated by thermal diffusion gives $k_\xi \approx k_T$ where $k_T = 1.5 \times 10^{-7}\,\mathrm{m}^2/\mathrm{s}$ is the molecular thermal diffusivity.

Selecting the right form of $\Phi_\xi(K)$ (either equation C.2 or C.3) requires knowledge of κ_v, which further requires knowing ϵ. Since there is no direct measurement of the turbulence within the North Tower plume, we estimate ϵ from the turbulent kinetic energy budget (modified from the original equations in Gregg (1987))

$$- < w'w' > \frac{dW}{dz} =< \rho'w' > \frac{g}{\rho_0} + \epsilon \tag{C.4}$$

where w' and W are the turbulent and mean plume vertical flow rate, ρ' and ρ_0 are the density fluctuations and reference density of the plume, g is the gravitational acceleration, and $<>$ denotes ensemble average. The laboratory results reported in Wang and Law (2002) suggest the ratios of turbulent to mean transport are constant at the centerline of a buoyancy-driven plume:

$$\frac{\sqrt{< w'w' >}}{W} = 6.83\%, \tag{C.5}$$

$$\frac{< w'\rho' >}{W\Delta\rho} = 5.09\%, \tag{C.6}$$

where $\Delta\rho$ is the mean density difference between the plume and the ambient seawater. In practice, we estimate W along the centerline of the North Tower plume from the Doppler-mode data recorded by COVIS following the procedures described in Section 3.1 (Figure C.1a). We estimate $\Delta\rho$ along the centerline of the North Tower plume from the conductivity-temperature-depth (CTD) measurements conducted within the North Tower plume during the same ROV dive on which the plume particles samples were collected (see Section 2.4.2 for the details of the CTD data collection and processing) (Figure C.1b). We smooth the estimates of W and $\Delta\rho$ using a LOESS filter (red curves in Figure C.1a,b) before substituting them into equations C.5 and C.6 to calculate the turbulent transport terms: $< w'w' >$ and $< w'\rho' >$, which are further substituted into equation C.4 to estimate ϵ (Figure C.1c).

Figure C.2 shows the Kolmogorov wavenumber calculated from the estimated ϵ shown in Figure C.1(c) and $\nu = 1.3 \times 10^{-6}\,\mathrm{m}^2/\mathrm{s}$. Also shown in the figure is the Bragg wavenumber corresponding to the acoustic signals used in the Imaging and Doppler modes of COVIS: $K = 2k_0 = 4\pi f_0/c = 3.33 \times 10^3$ rad/s with $f_0 = 396000$ Hz and $c = 1500$ m/s. The result suggests $K > \kappa_v$ for $z \geq 1$ m, and thus the turbulence that is responsible for generating the backscatter is in the viscous-convective subrange.

By definition, the variance of the normalized acoustic impedance fluctuations (σ_ξ^2) is

$$\sigma_\xi^2 = 4\pi \int_{\kappa_L}^{\infty} K^2 \Phi_\xi(K) dK, \tag{C.7}$$

where $\kappa_L = 2\pi/L$ is the wavenumber corresponding to the outer scale (L) of the inertial-convective subrange. In practice, we determine L as $2b_e$ where b_e is the plume's e-folding radius obtained by processing the Doppler-mode data recorded by COVIS following the procedures described in Section 3.1 (Figure C.1d).

To simplify the integration, we set the upper limit of the integral to $(5/12)^{3/2}\kappa_v$. This approximation is reasonable since the relative contribution from the eddies in the range $\kappa > (5/12)^{3/2}\kappa_v$ is expected to be small. Substituting equation (C.2) into equation (C.7) then gives

$$\begin{aligned} \sigma_\xi^2 &= \frac{3C}{\epsilon^{1/3}} \frac{\chi_\xi}{2} \left(\kappa_L^{-2/3} - \frac{12}{5} \kappa_v^{-2/3} \right) \\ &\approx \frac{3C}{\epsilon^{1/3}} \frac{\chi_\xi}{2} \kappa_L^{-2/3} \quad \text{for } \kappa_L \ll \kappa_v, \end{aligned} \tag{C.8}$$

and thus

$$\chi_\xi = \frac{2\epsilon^{1/3} \sigma_\xi^2 \kappa_L^{2/3}}{3C}. \tag{C.9}$$

Recall that the result shown in Figure C.2 suggests the turbulence responsible for generating the backscatter is in the viscous-convective subrange, substituting equations (C.9) into (C.3) gives

$$\Phi_\xi(K) = \frac{q\nu^{1/2}}{2\pi\epsilon^{1/6}} \frac{\sigma_\xi^2 \kappa_L^{2/3}}{3C} K^{-3} \exp(-qK^2/\kappa_{B\xi}^2). \tag{C.10}$$

Substituting the above equation into equation (C.1) gives the volume backscattering coefficient (s_v) of the turbulence-induced acoustic impedance fluctuations

$$s_v = \frac{q\nu^{1/2} \sigma_\xi^2 \kappa_L^{2/3} k_0}{24\epsilon^{1/6} C} \exp(-qK^2/\kappa_{B\xi}^2). \tag{C.11}$$

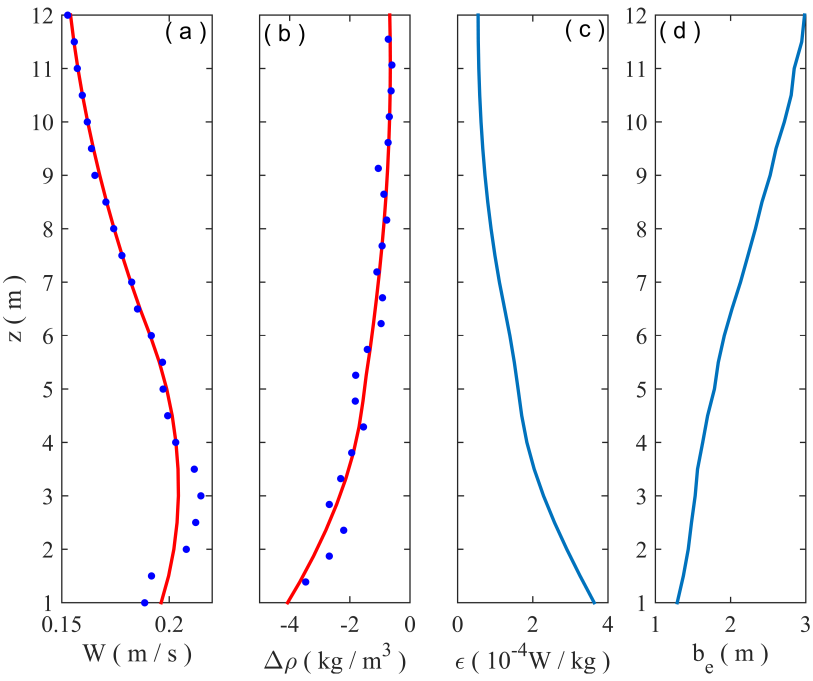

Figure C.1: (a) Mean vertical flow rate (W) along the centerline of the North Tower plume as a function of the height above the source vents (z) (blue dots). The estimates of W are obtained by processing the Doppler-mode data recorded by COVIS in May 2014 following the procedures described in Section 3.1 and taking the monthly average. The red curve denotes the smoothed estimates obtained using a LOESS filter. (b) Mean centerline density difference between the plume and the ambient seawater ($\Delta\rho$) estimated from the CTD data recorded during the same ROV dive on which the plume particle samples were collected (blue dots). The red curve denotes the smoothed estimates obtained using a LOESS filter. (c) Turbulent kinetic energy dissipation rate (ϵ) calculated from the estimates of W and $\Delta\rho$ using equations (C.4) to (C.6). (d) plume e-folding radius obtained by processing the Doppler-mode data recorded by COVIS in May 2014 following the procedures described in Section 3.1 and taking the monthly average.

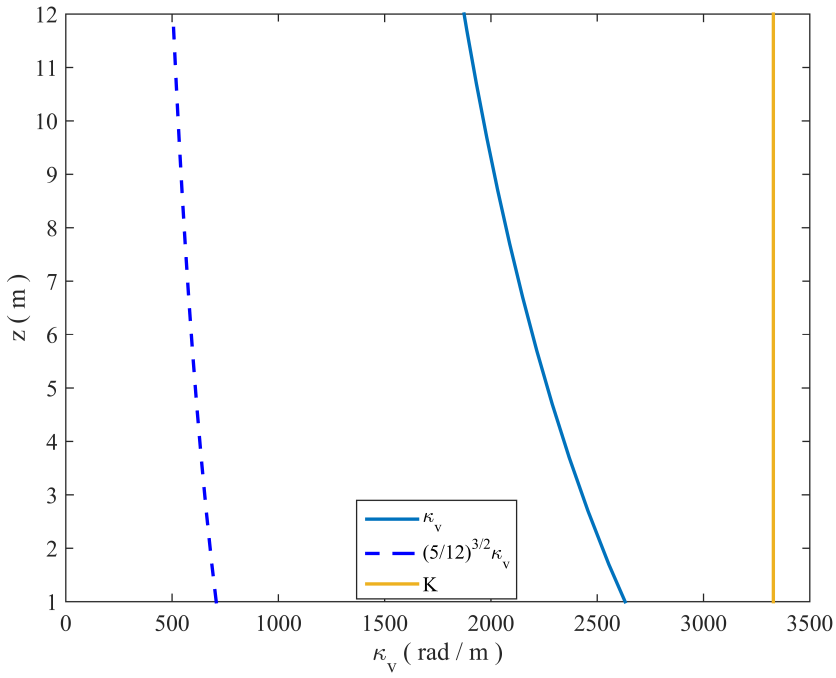

Figure C.2: The Kolmogorov wavenumber (κ_v) along the centerline of the North Tower plume as a function of the height above the source vents (z) (blue), and the Bragg wavenumber corresponding to the acoustic signals used in the Imaging and Doppler modes of COVIS (yellow).

C.1 Backscatter from Microstructure in Spatial Distribution of Particles

The acoustic impedance of particle-loaded seawater is

$$Z = \sqrt{K_e/\rho_e} \tag{C.12}$$

where K_e and ρ_e are the effective bulk modulus and density of the particle-loaded seawater. According to Richardson et al. (2002),

$$1/K_e = (1-\beta)/K_w + \beta/K_s, \tag{C.13}$$

$$\rho_e = \rho_w \frac{1-\beta+(2+\beta)h}{1+2\beta+2(1-\beta)h}, \tag{C.14}$$

where K_w is seawater bulk modulus, K_s is particle bulk modulus, $\beta = M/\rho_s$ is the fractional volume of the suspension occupied by the particles, and $h = \rho_s/\rho_w$ is the ratio of particle density (ρ_s) to seawater density (ρ_w). Since $\beta \ll 1$, substituting equations (C.13) and (C.14) into equation (C.12) and expanding the resulting expression to the first order of β gives

$$Z = Z_w \left\{ 1 + \frac{\beta}{2} \left[\frac{3(1-h)}{1+2h} - \frac{1}{e} + 1 \right] \right\}, \tag{C.15}$$

where $Z_w = \sqrt{K_w/\rho_w}$ is the acoustic impedance of seawater, $e = K_s/K_w$ is the ratio of particle bulk modulus (K_s) to seawater bulk modulus (K_w). Similarly, the variance of the normalized acoustic impedance fluctuations (σ_ξ^2) approximated to the first order of β is

$$\sigma_\xi^2 = \overline{\beta'^2} \frac{1}{4} \left[\frac{3(1-h)}{1+2h} - \frac{1}{e} + 1 \right]^2, \tag{C.16}$$

where $\overline{\beta'^2}$ is the variance of β, which increases with increasing magnitude of particle concentration fluctuations. Substituting σ_ξ^2 into equation (C.11) gives the volume backscattering coefficient of the microstructure in spatial distribution of particles

$$s_{vm} = \frac{q\nu^{1/2}\overline{\beta'^2} H \kappa_L^{2/3} k_0}{24\epsilon^{1/6} C} \exp(-qK^2/\kappa_{Bm}^2) \tag{C.17}$$

with

$$H = \frac{1}{4} \left[\frac{3(1-h)}{1+2h} - \frac{1}{e} + 1 \right]^2,$$

which is equation (2.9) in Section 2.3.2.

C.2 Backscatter from Temperature Fluctuations

As discussed in Appendix C.1, the volume backscattering coefficient (s_v) is related to the normalized acoustic impedance fluctuations (ξ) as (equation (C.11))

$$s_v = \frac{q\nu^{1/2}\sigma_\xi^2\kappa_L^{2/3}k_0}{24\epsilon^{1/6}C}\exp(-qK^2/\kappa_{B\xi}^2). \tag{C.18}$$

The contribution of temperature fluctuations to σ_ξ^2 can be approximated to the first order as

$$\sigma_\xi^2 = \frac{1}{4}\overline{T'^2}(a_T - \alpha_T)^2. \tag{C.19}$$

Within equation (C.19), $\overline{T'^2}$ is the variance of temperature fluctuations, a_T is the fractional change in sound speed due to temperature change, and α_T is the thermal expansion coefficient. Substituting equation (C.19) into equation (C.11) gives the volume backscattering coefficient of the microstructure in temperature field

$$s_{vT} = \frac{q\nu^{1/2}\overline{T'^2}(a_T - \alpha_T)^2\kappa_L^{2/3}k_0}{96\epsilon^{1/6}C}\exp(-qK^2/\kappa_{B\xi}^2) \tag{C.20}$$

which is equation (2.10) in Section 2.3.3.

Appendix D

Particle Sedimentation Formulation

This appendix gives the derivation of the formula used to estimate the variation of particle mass concentration (M) with height as discussed in Section2.4.1 for particles having a given radius based on the classic particle sedimentation theory described in Bursik et al. (1992); Ernst et al. (1996); Bemis et al. (2006). Figure D.1 shows a conceptual diagram of a vertical segment of a hydrothermal plume of thickness dz. The plume is assumed to be axisymmetric. Particles are lost from the segment through its lateral sloping margins and bottom boundary. Additionally, particle fallout from higher levels enters the segment through its top and lateral boundaries. The latter is a result of the re-entrainment caused by the turbulent eddies that sweep ambient seawater into the plume through its lateral boundaries. In general, fallout occurs when the particles' terminal settling velocity (v_t) is equivalent to or greater than the plume's vertical flow rate (W). According to Papanicolaou and List (1988), we can assume W to be Gaussian distributed over a given horizontal cross-section of the plume

$$W(r,z) = W_0(z)\exp\left(-\frac{r^2}{b_w^2}\right) \tag{D.1}$$

where r is the radial distance from the plume centerline, $W_0(z)$ is the centerline vertical flow rate at a given height z, and b_w is the e-folding radius of the Gaussian profile (i.e. the distance from the plume centerline to where w decrease to $1/e$ of W_0). According to Bonadonna et al. (1998), the expressions of v_t for different particle Reynolds number (R_p) are

$$v_t = \left[\frac{3.1g(\rho_s-\rho)2a}{\rho}\right]^{1/2}, \quad \text{for } R_p > 500 \tag{D.2}$$

$$v_t = 2a\left[\frac{4(\rho_s-\rho)^2 g^2}{225\mu\rho}\right], \quad \text{for } 0.4 < R_p < 500 \tag{D.3}$$

$$v_t = \frac{g(\rho_s-\rho)4R^2}{18\mu}, \quad \text{for } R_p < 0.4 \tag{D.4}$$

where R_p is defined as

$$R_p = 2W_0 a\rho/\mu. \tag{D.5}$$

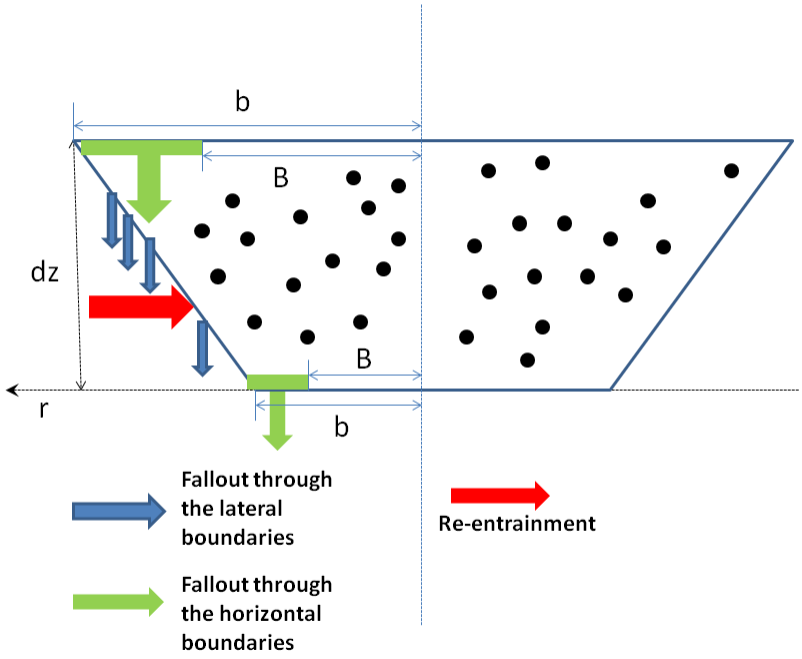

Figure D.1: Conceptual diagram of the particle fallout from and re-entrainment into a vertical segment of an axisymmetric plume of thickness dz. Within the figure, b is the radial distance from the centerline of the plume to its lateral sloping margins; B is the radial distance at which the plume's vertical flow rate equals the particles' terminal settling velocity. The areas from which the particles are lost from the plume segment are the lateral margins (blue arrows) and the circular region between B and b on the bottom (green arrows). Additionally, particles enter the segment through its lateral margins as a result of the re-entrainment effects (red arrows) and through the circular region between B and b on the top boundary (green arrows). This diagram summarizes the concepts of plume particle sedimentation theories described in Bursik et al. (1992); Ernst et al. (1996); Bemis et al. (2006).

Within Figure D.1, b is the distance from the centerline of the plume to its lateral boundaries, which is defined as $b = \sqrt{2}b_w$; B is the distance from the centerline to where W equals v_t, which is the radial distance at and beyond which the particle fallout occur. In the conceptual model depicted in Figure D.1, which follows the plume particle sedimentation theories described in Bursik et al. (1992); Ernst et al. (1996); Bemis et al. (2006), the loss of particles from a plume segment is restricted to being through the lateral boundaries and the

annulus within $B < r < b$ on the bottom. The conservation of the total mass of particles within the segment can be written as

$$\frac{d}{dz}Q = \frac{d}{dz}q - L + R \tag{D.6}$$

where Q is the mass transport of particles across the horizontal boundaries of the segment; q is the mass transport of particles through the annulus within $B < r < b$; Ldz is the mass transport of particles lost through the lateral boundaries; Rdz is the mass transport of the particles re-entrained into the segment. Assuming the particle mass concentration (M) has the same Gaussian cross-sectional distribution as W gives

$$M(r,z) = M_0(z)\exp\left(-\frac{r^2}{\lambda^2 b_w^2}\right) \tag{D.7}$$

where $M_0(z)$ is the particle mass concentration at the centerline of the plume at a given height, and λ is the ratio between the e-folding radii of the profiles of M and W. Subsequently, the expressions of Q and q are

$$Q = 2\pi \int_0^b WMrdr, \tag{D.8}$$

$$q = 2\pi v_t \int_B^b Mrdr. \tag{D.9}$$

According to Bursik et al. (1992),

$$Ldz = \eta v_t H \tag{D.10}$$

where

$$H = 2\pi \int_0^b Mrdr \tag{D.11}$$

is the total mass of the particles per unit thickness of the segment; the coefficient η arises from the geometry of the sloping margins of the segment and has the expression

$$\eta = \frac{2(A_t - A_b)}{(A_t + A_b)}. \tag{D.12}$$

Within equation (D.12), A_t and A_b are the areas of the top and bottom boundaries of the segment respectively, which can be written as

$$A_t = \pi(b + \tan\phi dz)^2,$$

$$A_b = \pi b^2,$$

where $\tan\phi = db/dz$ is the slope of lateral boundaries. Substituting these expressions into equation (D.12) and neglecting the second order terms of dz gives

$$\eta \approx 2\tan\phi dz/b. \tag{D.13}$$

Substituting equations (D.11) and (D.12) into equation (D.10) gives

$$L = \frac{4\pi\tan\phi}{b} v_t \int_0^b Mrdr \tag{D.14}$$

Adapted from the formula given in Ernst et al. (1996), the mass transport of the particles re-entrained into the segment is

$$Rdz = \frac{2\Psi dz H U_e}{b} \tag{D.15}$$

where Ψ is the re-entrainment coefficient defined in Ernst et al. (1996) with an empirically determined value of 0.4 for a buoyant plume; U_e is the flow rate at which the ambient seawater is entrained into the plume. According to Morton et al. (1956),

$$U_e = \alpha W_0 \tag{D.16}$$

where α is the entrainment coefficient and is related to the slope of lateral boundaries as $\alpha = 5\tan\phi/6$. Substituting equation (D.11) into equation (D.15) gives

$$R = \frac{4\pi\Psi U_e}{b} \int_0^b Mrdr. \tag{D.17}$$

Substituting equations (D.8), (D.9), (D.14), and (D.17) into equation (D.6) and eliminating the factor 2π gives

$$\frac{d}{dz}\int_0^b WMrdr = \frac{d}{dz} v_t \int_B^b Mrdr - \frac{2\tan\phi}{b} v_t \int_0^b Mrdr + \frac{2\Psi U_e}{b}\int_0^b Mrdr, \tag{D.18}$$

where W, M, v_t have the expressions given in equation (D.1), (D.7), and (D.4).

As described in Xu et al. (2013), we obtain time-series measurements of the centerline vertical flow rate (W_0) and e-folding radius (b_w) of the plume by processing the COVIS Doppler-mode data. In practice, we substitute W_0 and b_w averaged over a two year time series (January 2012 - December 2013) into equations (D.1) and (D.16) to calculate W and U_e. We then choose a given particle size and calculate the corresponding v_t using equation (D.4). Finally, we substitute W, U_e, and v_t into and integrate equation (D.18) from $z = 1$

m to a given height to obtain the centerline mass concentration (M_0) of particles having the chosen grain size at that height. The initial value used in the integration is a given value of M_0 at $z = 1$ m.

Appendix E

Backscatter Signal Calibration

The amplitude of the backscatter signal is calibrated to volume backscattering coefficient s_v in units m^{-1}, as discussed in Section 1.4, using the following sonar equation:

$$S_v = 20\log_{10}(|data_{in}|) - SL - D - G + TL - 20\log_{10}(RS) - 10\log_{10}(dV). \tag{E.1}$$

Within the equation, $S_v = 10\log_{10} s_v$ is the volume scattering strength, which is 10 times the logarithm of s_v; $|data_{in}|$ is the envelope of the raw back-scattered signals; SL is the source level of the transmitter; D is the directivity of the transmitter; G is the combined gain at both the transmitter and receiver ends; TL is the transmission loss caused by the absorption of sound by seawater and spherical expansion; RS is the receiver sensitivity, which is used to convert the units of the raw signal ($data_{in}$) from machine units to μPa; and dV is the volume element insonified by sound waves. Among those parameters mentioned above, SL and RS are measured through laboratory experiments; $TL = 40\log_{10} r + 2\alpha_w r$, where r is the distance of a given point in the plume from the sonar and $\alpha_w = 34.6\,\mathrm{dB/km}$ is the absorption coefficient calculated using the Francois-Garrison model (Francois and Garrison, 1982) with constant parameters: frequency = 396000 Hz, depth=2500 m, salinity=35 psu, temperature=2°C, and pH=7.

Appendix F

Doppler Velocity Measurement

As mentioned in Section 3.1.1, we measure the component V_r (in the direction of the acoustic line-of-sight) of plume velocity from the Doppler frequency shift f_D (Hz) of acoustic backscatter using the covariance method described in Jackson et al. (2003). The following equation gives the relation between V_r and f_D,

$$V_r = \frac{cf_D}{2f_c} \tag{F.1}$$

$$f_D = \frac{1}{2\pi\Delta t} ANGLE \left[\sum_{n=1}^{N_p} \int_{t=0}^{T_w} E(t)E^(*)(t+\Delta t)dt' \right] \tag{F.2}$$

In equation (F.1), c is the sound speed and $f_c = 396kHz$ is the sonar operation frequency in the Doppler mode. In equation (F.2), the operator $ANGLE[\ ]$ calculates the phase angle in radians of a complex number. $E(t)$ is a demodulated complex signal corresponding to a given azimuthal beam and a given ping, whose amplitude and phase reflect the amplitude of the acoustic backscatter and its phase shift relative to the transmitted pulses. The integral in equation (F.2) estimates the autocorrelation function of $E(t)$ at the time lag Δt. Note that a rectangular window with length $T_w = 1$ ms is used to truncate the received signal. A summation over $N_P = 40$ pings at each elevation angle reduces the uncertainty in the measurement caused by turbulence and background noise. In addition, the standard deviation V_{std} of V_r is calculated over the 40 pings, which is used as a measure of the statistical uncertainty in the Doppler measurements (Jackson et al., 2003).

Appendix G

Entrainment Coefficient Calculation

As cited in Section 3.2, Tao et al. (2013) estimate the entrainment coefficient (α) of hydrothermal plumes rising in stably stratified static environments using numerical simulations. Their estimates are reported to be consistent with experimentally determined values but somehow not explicitly given in their paper. We herein recalculate the entrainment coefficient using the simulation results and method presented in Tao et al. (2013).

According to Morton et al. 1956, the maximum rising height of a buoyant plume can be calculated as

$$Z_m = C_e \left(\frac{B_0}{N^3} \right)^{1/4} \tag{G.1}$$

where B_0 ($\mathrm{m^4 s^{-3}}$) is the initial buoyancy transport of the plume and N (1/s) is the buoyancy frequency, and

$$C_e = 1.148 \alpha^{-1/2} \tag{G.2}$$

is a universal constant. By performing linear regression on the simulation results of Z_m with different combinations of B_0 and N, Tao et al. (2013) obtain $C_e = 4.05$. Substituting into equation G.2 gives $\alpha = 0.083$.

Appendix H

Spectrum Calculation

This appendix introduces the method used to obtain the power spectrum of the plume centerline vertical flow rate shown in Figure 3.6(b). The time series samples of vertical volume transport, centerline vertical flow rate, and expansion rate are not evenly spaced. The sampling is semi-regular with the sampling interval oscillating around 3 hours with small amplitude. In addition, the time series has gaps concentrating mostly in the sector before October 9th (see Figure 3.4(a), (b) in the main text). As result, a modified periodogram (Lomb-Scargle periodogram, Scargle 1982) is used for spectral analysis of the time series. The Lomb-Scargle periodogram has the following mathematical form

$$P_X(w) = \frac{1}{2}\left\{ \frac{\left[\sum_j^M X_j \cos w(t_j - \tau)\right]^2}{\sum_j^N \cos^2 w(t_j - \tau)} + \frac{\left[\sum_j^N X_j \sin w(t_j - \tau)\right]^2}{\sum_j^N \sin^2 w(t_j - \tau)} \right\} \tag{H.1}$$

where τ is defined by

$$\tan(2w\tau) = \left(\sum_j^N \sin 2wt_j\right) / \left(\sum_j^N \cos 2wt_j\right). \tag{H.2}$$

Within the above equation, $w = 2\pi f$ and f is the frequency of interest; X is the time series data; N is the number of samples within the time series. The results shown in Figure 3.6 of the main text are normalized to the variance of the time series ($P_X(w)/\sigma_X^2$) and are thus dimensionless.

The Lomb-Scargle periodogram has well defined statistics for unevenly spaced samples. Assuming X_j are independent samples of normally distributed noise, the significance level of a spectral peak $Z = 2P_X(w)/\sigma_X^2$ (the chance of observing a spectral peak greater than Z) is (Scargle, 1982)

$$Q_Z = 1 - \left(\int_0^Z \chi_k^2(Z)dZ\right)^N, \quad k = 2, \tag{H.3}$$

where χ_k^2 is the probability density function of the chi-square distribution with k degrees of freedom. In order to smooth the spectrum, periodograms calculated at different levels along the plume axis (S = 5 to 15 m at 0.5-m intervals) are averaged to give the result shown in Figure 3.6. Since a total of 21 periodogram are used for averaging, assuming the noise at different levels is independent, the significance level of the smooth spectrum becomes

$$Q_Z = 1 - \left(\int_0^{MZ} X_k^2(Z) dZ \right)^N, \quad k = 2M,\ M = 21. \tag{H.4}$$

The dashed horizontal line in Figure 3.6 denotes the value of Z with the significance level of 0.05 (5%).

Appendix I

Quantifying the Tidal Loading Effects

This appendix quantifies the potential contribution of the tidal loading effects to the temporal variations in the plume centerline vertical flow rate (W_c) time series shown in Figure 3.4(b) in Section 3.3.2. According to Morton et al. (1956), the centerline vertical flow rate of a buoyant plume injecting into a uniform, static background fluid from a point source ($B_0 \neq 0$, $M_0 = 0$, $Q_0 = 0$, where $M_0 = \frac{1}{2}b^2W_0^2$, and $Q_0 = b^2W_0$ are the initial momentum and volume transports) can be calculated as

$$W_c = q\left(\frac{B_0}{z}\right)^{1/3}, \tag{I.1}$$

$$B_0 = \frac{\lambda^2}{1+\lambda^2}b^2W_0 g\alpha_t\Delta T. \tag{I.2}$$

Within the equations, B_0 ($\mathrm{m}^4/\mathrm{s}^3$) is the the initial specific buoyancy transport of the plume; z is the height above the source; q is an empirically determined constant, which is assumed ~ 1; b, W_0, and ΔT are the orifice radius, initial vertical flow rate and temperature anomaly of the plume; α_t is the thermal expansion coefficient; $\lambda = 1.2$ is the empirically determined ratio between the e-folding radii of the cross-sectional distributions of temperature and vertical flow rate; $g = 9.8\,\mathrm{m/s}^2$ is the gravitational acceleration.

A plume from a finite source ($B_0 \neq 0$, $M_0 \neq 0$, $Q_0 \neq 0$) is asymptotically identical to the plume from a point source (B_0, 0, 0) at vertical distance Z_0 below the vent orifice. Therefore we rewrite equation (I.1) as

$$W_c = \left(\frac{B_0}{z+Z_0}\right)^{1/3} \tag{I.3}$$

before applying it to the the hydrothermal plume observed in this study. Using the formulations developed by Morton (1959) with minor modification, Z_0 is calculated as

$$\frac{Z_0}{\eta} = 3.253 - 3.126|\gamma|^{3/2} \int_{-1}^{1/|\gamma|} (t^5 + 1)^{-1/2} t^3 dt, \tag{I.4}$$

$$\eta = 2^{-3/4} \alpha^{-1/2} (1 + \lambda^2)^{-1/2} |V_0|^{3/2} |B_0|^{-1/2}, \tag{I.5}$$

$$\gamma^5 = 1 - \Gamma, \tag{I.6}$$

$$\Gamma = 2^{9/2} 5 \alpha^{-1} (1 + \lambda^2) B_0 V_0^{-5} Q_0^2 \tag{I.7}$$

where $\alpha = 0.08$ is the entrainment coefficient, and $V_0 = M_0^{1/2}$. Substituting the parameters listed below into equations (I.2) to (I.4) gives $Z_0 = 3.6$ m and the mean values of W_c at 5, 10, and 15 m above the orifice. Note that the parameters are chosen to match those measured at Grotto. Increasing W_0 and ΔT by 40% and 6%, which are the observed variations of venting flow rate and temperature reported in Crone et al. (2010) and Larson et al. (2007) respectively (see Section 3.3.2 of the main text), and substituting into equations (I.2) to (I.4) along with the other parameters listed below gives the perturbed values of W_c at each height. Table I.1 summarizes the results. The ratios of deviations to means are also given in Table 3.1 in the main text.

$$z = 5,\ 10,\ \text{and}\ 15\,\text{m}; \tag{I.8}$$

$$\alpha = 0.08 \tag{I.9}$$

$$\lambda = 1.2 \tag{I.10}$$

$$\Delta T = 350\,^{\circ}\text{C}; \tag{I.11}$$

$$W_0 = 0.3\,\text{m/s}; \tag{I.12}$$

$$b = 0.1\,\text{m} \tag{I.13}$$

$$\alpha_t = 10^{-4} (^{\circ}C)^{-1} \tag{I.14}$$

Table I.1: Tidal Loading Effects on W_c

z (m)	Mean (m/s)	Perturbed (m/s)	Deviation/Mean
5	0.0414	0.0462	11.6%
10	0.0355	0.0399	12.5%
15	0.0320	0.0361	12.9%

Appendix J

Isolation of the Inertial Oscillation

As discussed in Section 3.3.3, we isolate the inertial oscillation from the mean plume centerline vertical velocity component $< W_c >$ by fitting the following sinusoidal function to the time series of $< W_c >$,

$$W_{ci} = C + A\cos(2\pi f_c t) + B\sin(2\pi f_c t) \tag{J.1}$$

where $C = \frac{1}{\tau}\int_t^{t+T} < W_c(t) > dt$ is the mean value of the time series, $f_c = 1.5$ cycle/day is the inertial peak in the spectrum (Figure 3.6 in the main text), A and B are optimal coefficients corresponding to the minimum of the mean squared fitting error

$$R = \frac{1}{\tau}\int_t^{t+T} (W_c(t) - W_{ci}(t))^2 dt. \tag{J.2}$$

The amplitude of the inertial oscillation is

$$Amp = \sqrt{A^2 + B^2} \tag{J.3}$$

and the phase is

$$Pha = arctan\left(\frac{B}{A}\right). \tag{J.4}$$

A moving window of length $T = 4$ days is used to segment the time series to yield the variation of the inertial oscillation amplitude as a function of time shown in Figure 3.9 in Section 3.3.3.

Note that we use the least-square-fit method describe above instead of the common band-pass filters (Thomson et al., 1990) to extract the inertial oscillations because the $< W_c >$ time series is unevenly sampled and has gaps. The least-square-fit method is immediately applicable to unevenly sampled time series; whereas one has to interpolate the $< W_c >$ time series onto an evenly spaced time axis before band-pass filtering, and the interpolation process will introduce bias into the result.

Appendix K

Simple Plume Model Formulation

This appendix gives the derivation of equation (K.9) in Section 5.1.1 by solving the conservation equations described in Morton et al. (1956). For an axisymmetric buoyancy-driven plume, its specific buoyancy transport ($B0$) is

$$B0 = \int_0^\infty 2\pi W(r,z) g(\rho_w - \rho(r,z))/\rho_{ref} r dr \tag{K.1}$$

where z is the height above the plume source, r is the radial distance from the plume's centerline, W is the plume's vertical flow rate, ρ_w is the seawater density, ρ is the plume density, and ρ_{ref} is the reference density. Assuming W and B have Gaussian cross-sectional profiles yields

$$W(r,z) = W_c(z) \exp(-r^2/b_e(z)^2), \tag{K.2}$$

$$g(\rho_w - \rho(r,z))/\rho_{ref} = g(\rho_w - \rho_c(z))/\rho_{ref} \exp\left(-r^2/\lambda^2 b_e(z)^2\right), \tag{K.3}$$

where W_c and ρ_c are the plume centerline vertical flow rate and density, b_e is the plume e-folding radius, and λ is the plume concentration-to-velocity ratio. Substituting equations (K.2) and (K.3) into (K.1) gives

$$B0 = \frac{\pi g \lambda^2 (\rho_w - \rho_c(z)) W_c(z) b_e(z)^2}{\rho_{ref}(1+\lambda^2)}. \tag{K.4}$$

The conservation equations governing the behavior of a buoyant plume with Gaussian

velocity and buoyancy profiles in an homogeneous, calm (i.e. zero ambient current) environment are (Morton et al., 1956)

$$\begin{aligned}
\frac{d}{dz}(\pi b_e^2 W_c) &= 2\pi\alpha b_e W_c \quad \text{Volume} \\
\frac{d}{dz}\left(\frac{1}{2}\pi b_e^2 W_c^2\right) &= \int_0^\infty 2\pi g \frac{\rho_w - \rho}{\rho_{ref}} r dr \\
&= \pi\lambda^2 b_e^2 g \frac{\rho_w - \rho_c}{\rho_{ref}} \\
&= \frac{(1+\lambda^2)B0}{W_c} \quad \text{Momentum} \\
\frac{d}{dz}B0 &= 0 \quad \text{Buoyancy}
\end{aligned} \tag{K.5}$$

Solving the equation group (K.5) analytically gives

$$b_e = \frac{6}{5}\alpha z, \tag{K.6}$$

$$B0 = \frac{24\pi\alpha^2 W_c(z)^3 z}{25(1+\lambda^2)}. \tag{K.7}$$

Since the volume transport of the plume is

$$Q(z) = \int_0^\infty 2\pi W(r,z) r dr = \pi b_e(z)^2 W_c(z), \tag{K.8}$$

substituting with equation (K.6) into equation (K.7) to eliminate W_c and b_e gives

$$Q(z) = \left(\frac{3\pi^2(1+\lambda^2)}{2(5/(6\alpha))^4}\right)^{1/3} B_0^{1/3} z^{5/3}, \tag{K.9}$$

which is equation (K.9) in section 5.1.1.

Appendix L

Monte Carlo Simulation

We establish a Monte-Carlo simulation to quantify the uncertainty in the heat transport estimate originating from the first two error sources mentioned in Section 3.1.4. First of all, we calculate the ideal volume transport (Q) and e-folding radius (b_e) over a vertical range $10 \leq z_i \leq 22$ m with a source heat transport $H_0 = 18$ MW by substituting H_0 and z_i into equations (D.8) and (5.3). The two error sources are introduced into the simulation by adding random Gaussian errors to the ideal Q and b_e profiles and the default values of entrainment coefficient (α) and concentration-to-noise ratio (λ). The errors in Q and b_e are 4% of their ideal values as are shown in Figure 5.1, while the errors in α and λ are 20% and 13% of their default values respectively. We then estimate H_0 following the procedures described in Section 5.1.1 using the perturbed profiles and constant parameters. This simulation is repeated $10,000$ times. Figure L.1 shows the histogram of the simulated H_0 estimates, which has a mean value ~ 17.95 MW with a standard deviation ~ 2.91 MW. We use the standard deviation as the proxy for the combined uncertainty stemming from the two error sources.

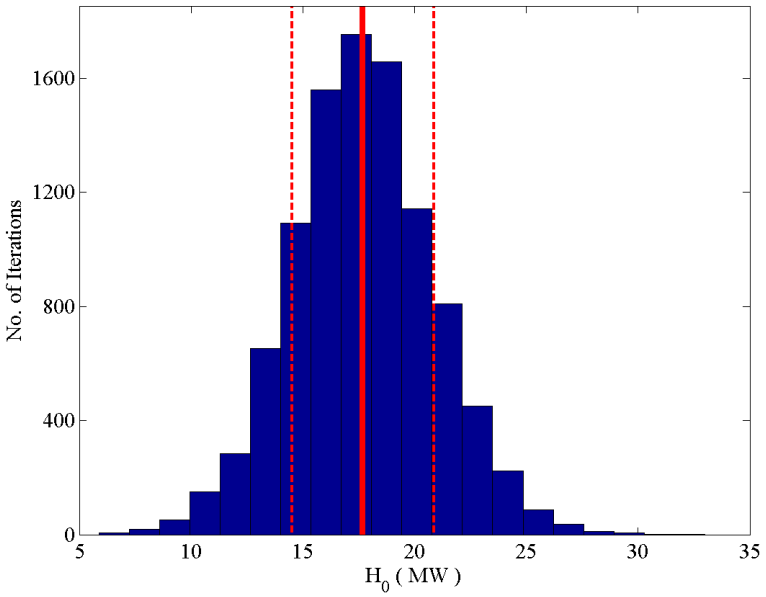

Figure L.1: Histogram of the simulated heat transport (H_0) estimates. The solid red line marks the mean value (17.69 MW) and the dashed red lines delimit one standard deviation (3.18 MW) away from the mean value.